Doppler Shift Estimation of MIMO-OFDM Systems Based on Auto-correlation Function of Channel Estimate

Qin Zhu

A Thesis

in

The Department

of

Electrical and Computer Engineering

Presented in Partial Fulfilment of the Requirements

for the Degree of Master of Applied Science at

Concordia University

Montréal, Québec, Canada

Your file Votre référence
ISBN: 978-0-494-63074-7
Our file Notre référence
ISBN: 978-0-494-63074-7

ABSTRACT

Doppler Shift Estimation of MIMO-OFDM Systems Based on Auto-correlation Function of Channel Estimate

Qin Zhu

Multiple-input multiple-output (MIMO) and orthogonal frequency division multiplexing (OFDM) techniques have been considered as a strong candidate for the next-generation wireless communication systems, due to their well-known advantages in high data-rate wireless transmission as well as high frequency spectrum efficiency. In the mean time, channel state information (CSI) is required for precise detection and recovery of signals. Therefore, channel estimation plays a significant role in MIMO-OFDM systems. On the other hand, due to the high mobility of wireless terminals, Doppler shift (DS) can be one of the major side-effects of utilizing MIMO-OFDM techniques, which may lead to severe performance loss. Many schemes on DS estimation have been developed for broadband single-input single-output (SISO) systems. A commonly used method is to exploit the auto-correlation property of the channel impulse response (CIR) estimated by well-developed channel estimation approaches, which not only has high accuracy but also moderate computational complexity. Hence, we first investigate an efficient channel estimation method in this thesis. We will then focus on Jakes' model based DS estimation schemes, and further extend to independently identically distributed (i.i.d.) MIMO-OFDM fading channels with both Rayleigh and Rician distributions.

In the first part of the thesis, a training-sequence (TS) based least square (LS) channel estimation scheme is presented for MIMO-OFDM systems along with plenty of computer

simulations and corresponding analyses. Experimental study shows that the CIR estimates obtained by the LS method are reliable under moderate channel conditions, and can efficiently be utilized for DS estimation.

The second part of the thesis first studies the auto-correlation function (ACF) based DS estimation schemes for SISO-OFDM systems in Rayleigh fading channels, and then extends it to Rician fading channels by developing a new approach along with the analysis of its accuracy and complexity. Thereafter, we apply those approaches to MIMO-OFDM systems and present a few enhanced methods by using non-linear interpolation under certain circumstances. Detailed computer simulations and comparisons are performed, confirming that the proposed ACF based schemes give satisfactory estimation performance over i.i.d. Rayleigh or Rician fading channels with various channel conditions.

ACKNOWLEDGMENTS

First and foremost, I would like to express my sincere gratitude and appreciation to my supervisor, Dr. Weiping Zhu, for his guidance throughout this research. He has given me excellent guidance to choose this research topic. It is an honor to work under his supervision.

I would also like to thank my friends, especially Dr. Feng Wan for his help in resolving some technical difficulties and thesis writing. I have gained a great deal of knowledge from his direction.

My deepest appreciation goes to my parents for their selfless love and support throughout my life.

Contents

List of Figures ix

List of Abbreviations xii

List of Symbols xv

1 Introduction 1

1.1 Background 1

1.2 OFDM and MIMO Technologies 3

1.2.1 Orthogonal Frequency Division Multiplexing 3

1.2.2 Multiple Input Multiple Output Technology 4

1.2.3 Combination of MIMO and OFDM Techniques 5

1.3 Motivation and Objectives of the Research 7

1.4 Organization of the Thesis 8

1.5 Contributions 9

2 Fundamentals of MIMO-OFDM Systems 11

2.1 Basic Concepts of Wireless Channels 12

2.1.1 Types of Multi-path Fading Channels 12
2.1.2 Fading Channel Model 15
2.1.3 Doppler Effect and Auto-correlation of CIR 19
2.2 OFDM Systems 22
2.2.1 Transceiver 23
2.2.2 OFDM Symbol Design 23
2.3 MIMO-OFDM Systems 27
2.3.1 MIMO Channel Model 27
2.3.2 MIMO-OFDM System Model 28
2.3.3 MIMO-OFDM Signal Model 30
2.3.4 Recovery of MIMO-OFDM Signals 32
2.4 Conclusion 33

3 Training based LS Channel Estimation for MIMO-OFDM Systems 34

3.1 LS Channel Estimation Using TSs 34
3.2 Optimal Pilot Design over Multiple OFDM Symbols 39
3.3 LS Channel Estimation Performance of MIMO-OFDM Systems 40
3.3.1 Experiment 1: Effect of Antenna Configurations 41
3.3.2 Experiment 2: Effect of Guard Interval 42
3.3.3 Experiment 3: Effect of Optimal Pilots 44
3.3.4 Experiment 4: Effect of Maximum DS 45
3.3.5 Experiment 5: Estimation of Rician Channels 47
3.4 Conclusion 49

4 ACF based DS Estimation for MIMO-OFDM Systems **50**

4.1 ACF based DS Estimation for SISO Systems 51

4.1.1 Auto-correlation Feature of Rayleigh Fading Channels 51

4.1.2 DS Estimation Employing Zero-crossing Point of ACF 52

4.1.3 DS Estimation Employing ACF Curve 54

4.1.4 DS Estimation for Rician Fading Channels 61

4.2 ACF Based DS Estimation for i.i.d. MIMO-OFDM Systems 65

4.2.1 Rayleigh Fading Channels 65

4.2.2 Rician Fading Channels 69

4.3 Accuracy Analysis of Proposed Algorithms with Possible Practical Solutions 69

4.3.1 Zero-crossing Scheme 70

4.3.2 ACF Curve Schemes 71

4.3.3 Half-period Scheme for LOS DS 75

4.4 Simulation Results 78

4.4.1 Rayleigh Fading Channels 78

4.4.2 Rician Fading Channels 87

4.5 Conclusions 93

5 Conclusions and Future Work **95**

5.1 Summary 95

5.2 Future Research 97

Bibliography **99**

List of Figures

2.1 Multi-path fading 12

2.2 Relationship of fading and symbol duration 14

2.3 Relationship of fading and symbol bandwidth 15

2.4 The NLOS and LOS paths 17

2.5 The pdf of Rayleigh and Rician distributions when $\sigma = 1$. 18

2.6 Doppler effect 19

2.7 Jakes Doppler spectrum, $f_d = 100$ Hz 20

2.8 ACF of CIR of Rayleigh and Rician channels 22

2.9 The transmitter model of OFDM systems 23

2.10 The receiver model of OFDM systems 24

2.11 Orthogonal subcarriers in the frequency and time domain 25

2.12 MIMO channel with N_t transmit antennas and N_r receive antennas 27

2.13 MIMO-OFDM transmitter 29

2.14 MIMO-OFDM receiver 29

3.1 MIMO-OFDM transmitter with optimal pilots 35

3.2 MIMO-OFDM receiver with TSLS channel estimator and DS estimator . . 36

3.3 Flowchart for LS algorithm at the receiver 38
3.4 Training over a single OFDM symbol 40
3.5 MSE versus SNR with different antenna configurations 42
3.6 MSE versus SNR with different guard lengths 43
3.7 MSE versus SNR with different number of optimal pilots 44
3.8 MSE versus SNR with different DSs, $T = 1\ \mu s$ 46
3.9 MSE versus SNR with different DSs, $T = 0.1\ \mu s$ 46
3.10 MSE versus SNR in Rician fading channels, $\theta_0 = 90°$ 48
3.11 MSE versus SNR in Rician fading channels, $\theta_0 = 0$ 48
3.12 Rician fading 49

4.1 Zeroth-order Bessel function of the first kind 52
4.2 Linear interpolation of ACF curve for estimating the first zero-crossing point 53
4.3 Flowchart of zero-crossing algorithm 55
4.4 Flowchart of polynomial curve fitting algorithm 58
4.5 Flowchart of look-up table scheme 59
4.6 Normalized ACF when $\theta_0 = 90°$ 62
4.7 Normalized ACF curve of Rician fading channel 63
4.8 Flowchart of LOS DS estimator 64
4.9 Averaged ACF of all links versus the ACF of single link, SNR = 0 dB . . . 68
4.10 Linear interpolation and non-linear interpolation 71
4.11 Choosing partial ACF curve 72
4.12 Slope of Bessel function $J_0(x)$ 73

4.13 A typical binary search tree 74

4.14 ACF when $f_{d,LOS}$ is small 75

4.15 Cosine-like ACF curve and interpolation 76

4.16 Valley and peak points on the ACF curve 77

4.17 NMSE of $\hat{f}_d$ versus SNR for different receive antenna configurations 79

4.18 NMSE of $\hat{f}_d$ versus SNR with regard to guard interval 80

4.19 NMSE of $\hat{f}_d$ versus SNR with different number of pilots 81

4.20 Comparison between systems with different sample rates of 1 μs and 0.5 μs 82

4.21 Comparison of two estimators with different number of CIR estimates . . . 84

4.22 Comparison of two estimators for different DSs with a spline interpolation enhanced method at 20 dB 85

4.23 Comparison of two estimators at different SNRs 86

4.24 NMSE of $\hat{f}_{d,LOS}$ versus SNR 88

4.25 NMSE of $\hat{f}_{d,LOS}$ versus number of channel estimates 89

4.26 Effect of K-factor 90

4.27 Effect of AOA 91

4.28 NMSE of $f_{d,LOS}$ versus f_d with and without spline interpolation 93

List of Abbreviations

4G	Fourth Generation
ACF	Auto-Correlation Function
AOA	Angle Of Arrival
AWGN	Additive White Gaussian Noise
B3G	Beyond 3rd Generation
BST	Binary Search Tree
CIR	Channel Impulse Response
CP	Cyclic Prefix
CSI	Channel State Information
DAC	Digital to Analog Converter
DFT	Discrete Fourier Transform
DS	Doppler Shift
FFT	Fast Fourier Transform
FIR	Finite Impulse Response
GI	Guard Interval
ICI	Inter Carrier Interference

IFFT	Inverse FFT
i.i.d.	Independently Identically Distributed
ISI	Inter Symbol Interference
LCR	Level Crossing Rate
LOS	Line Of Sight
LS	Least Square
LTI	Linear Time Invariant
LTV	Linear Time Variant
MAP	Maximum A Posterior
MIMO	Multiple-Input Multiple-Output
ML	Maximum Likelihood
MMSE	Minimum Mean Squared Error
MSE	Mean Squared Error
NLOS	Non Line Of Sight
OFDM	Orthogonal Frequency Division Multiplexing
PAPR	Peak to Average Power Ratio
pdf	Probability Density Function
PSK	Phase Shift Keying
QAM	Quadrature Amplitude Modulation
QoS	Quality of Service
QPSK	Quadrature Phase Shift Keying
ROM	Read Only Memory

SISO	Single-Input Single-Output
SNR	Signal to Noise Ratio
TS	Training Sequence
TSLS	Training-Sequence based Least Square
VBLAST	Vertical Bell Laboratories Layered Space-Time
ZF	Zero-Forcing

List of Symbols

c	Speed of light
E_b	Power of transmitted signals
$\mathbf{F}$	Unitary DFT matrix
f_d	Maximum Doppler shift
$f_{d,LOS}$	Direct path Doppler shift
g	g consecutive OFDM symbols with inserted training pilots
$\mathbf{H}_l$	Channel matrix of the lth tap
$h_l^{n_r,n_t}(m)$	Complex CIR between the n_tth transmit antenna to the n_rth receive antenna of the lth tap during the mth symbol
$\mathbf{I}$	Identity matrix
$I_0(\cdot)$	Zeroth-order modified Bessel function
$J_0(\cdot)$	Zeroth-order Bessel function of the first kind
K	K-factor or Rice factor
k_0	First zero-crossing point
k_e	Effective valley point
k_v	First vally point

L	Channel length
L_g	Guard length
N	Number of sub-carriers
N_p	Number of pilots within one OFDM symbol
N_r	Number of receiver antennas
N_t	Number of transmit antennas
$R_{xx}(\tau)$	Auto-correlation function of x with lag τ
T_s	Symbol duration
T	Sample duration
v	Relative motion speed
$\hat{x}$	Estimated value of x
$\delta(\cdot)$	Dirac delta function
$\delta_{i,j}$	Kronecker delta function
$\Im$	Imaginary component
$\Re$	Real component
σ_n^2	Power of noise
σ_h^2	Power of CIR
θ_0	AOA of the direct path (LOS)
$(\cdot)^*$	Complex conjugation
$a \mod b$	Modulo
$\mathrm{E}\{\cdot\}$	Expectation
$*$	Linear convolution

$\otimes$	Circular convolution
$\|\|\mathbf{X}\|\|_F$	Frobenius norm of $\mathbf{X}$
$\mathbf{X}^T$	Transpose of $\mathbf{X}$
$\mathbf{X}^H$	Hermitian or complex conjugate transpose of $\mathbf{X}$
$\mathbf{X}^\dagger$	Moore-Penrose pseudo-inverse of $\mathbf{X}$
$\mathrm{diag}(\mathbf{x})$	Diagonal matrix with its main diagonal elementsdenoted by $\mathbf{x}$
$\mathrm{vec}(\mathbf{X})$	A stacking of the columns of matrix $\mathbf{X}$ into a vector

Chapter 1

Introduction

1.1 Background

With the increasingly growing demand for mobile communications and Internet and multimedia services, the frequency bandwidth becomes a bottleneck in the next generation wireless communications. This problem is difficult to solve without significantly increasing the wireless channel bandwidth. On the other hand, the transmission performance in wireless mobile environments is another main issue in the next generation communications. Due to the shadowing effect of multi-path fading channel and the high mobility of wireless terminals, the performance of communication system might be severely degraded.

Many approaches have been proposed to solve the bandwidth and reliability problems, and most well known schemes are multiple-input multiple-output (MIMO) systems and orthogonal frequency-division multiplexing (OFDM) systems, which are also considered as strong candidates for the next generation wireless communication network, or the 4th generation network.

The 4th generation (4G), or beyond 3G (B3G), describes the next level of evolution in wireless communications. A 4G system will offer a complete replacement for existing communication networks and is expected to provide a comprehensive and secure IP based solution, varieties of multimedia services will be provided at higher data rates on an "Anytime, Anywhere" basis. The following objectives of the next generation wireless communication standard have been defined by the 4G working group [1][2]:

- A spectrally efficient system to be designed.
- High network capacity which means more simultaneous users per cell.
- A nominal data rate of 100 Mbps while the client physically moves at high speeds relative to the base station, and 1 Gbps while client and base station are in relatively fixed positions as defined by the ITU-R.
- A data rate of at least 100 Mbps between any two points.
- Smooth hand-off across heterogeneous networks.
- Seamless connectivity and global roaming across multiple networks.
- High quality of service (QoS) for next generation multimedia support.
- Interoperability with existing wireless standards.
- An all IP, packet switched network.

1.2 OFDM and MIMO Technologies

1.2.1 Orthogonal Frequency Division Multiplexing

OFDM, a multi-carrier modulation method, has already been developed as a popular scheme for wide-band communications. The principle of OFDM is to split a high-rate data stream into a number of orthogonal parallel streams at lower rates, which are transmitted simultaneously over a number of sub-carriers. Since the symbol duration increases for the lower rate parallel sub-carriers, the relative dispersion in time caused by multi-path delay is largely decreased. A guard interval (GI) is inserted in each OFDM symbol, during which, the OFDM symbol is cyclically extended, such that inter symbol interference (ISI) can be eliminated. As a result, each sub-channel can be considered as flat fading. Furthermore, the sub-carrier frequencies are chosen so that they are orthogonal to each other, which eliminates the inter carrier interference (ICI) as well as increases spectral efficiency without requiring extra bandwidth.

Although OFDM technique simplifies the complexity of communication systems, orthogonality does introduce a severe frequency-sensitive problem. Typically, frequency offsets are caused by the mismatching between the transmitter and receiver oscillators, or by Doppler shift (DS) due to relative movement. This thesis focuses on the DS issue.

The primary advantages of OFDM systems over other modulation schemes are listed as follows:

- Resistance to frequency-selective fading, since each sub-channel is almost flat fading.
- Simple equalization, due to the flat fading feature of the sub-channels.

- Robustness against ISI by the insertion of appropriate GI in each OFDM symbol.
- High spectral efficiency by overlapping the orthogonal sub-carriers.
- Easy implementation using FFT chips at both the transmitter and the receiver.

OFDM also has some disadvantages, such as:

- Sensitivity to DS and frequency synchronization error, which creates ICI.
- High peak-to-average-power ratio (PAPR), which reduces efficiency of the RF power amplifier.

1.2.2 Multiple Input Multiple Output Technology

Essentially, OFDM is a single-input and single-output (SISO) technique. Although it introduces orthogonality and GI to improve communication performance, the low data rate limits its applications in the modern wireless communications. Therefore, multiple-input and multiple-output, or MIMO, which uses the multiple antennas at both the transmitter and receiver, gets in our sight.

MIMO technology makes use of the effect of multi-path fading or spatial diversity, as well as efficient coding algorithms, such as the most well known space-time coding [3], to increase the data rate and capacity of the system without sacrificing bandwidth and transmit power. It also has been chosen as one of the major techniques in the IEEE 802.16e and IEEE 802.11n standards.

A list of several advantages of MIMO system are shown below:

- It provides higher data rates, which will be suitable for current and future usage such as Internet surfing, voice conference, data sharing, etc.
- It reduces the effects of interference and as a result lower transmission power and longer battery lifetime.
- Adjustable power and phase of each transmit antenna in terms of water-filling criteria to further improve QoS.
- Secured transmission due to multiple transmit and receive antennas.
- Various coding systems can be utilized to alleviate the performance loss due to multi-path fading.
- Well combined with OFDM modulation for simple receiver design.

1.2.3 Combination of MIMO and OFDM Techniques

The combination of OFDM and MIMO technologies not only solves the frequency-selective fading problem, but also increases channel capacity greatly, which is the most attractive feature. In the mean time, the increase of total transmission power or bandwidth is entirely not required as compared with its single antenna counterpart. And the channel capacity has been proved to grow linearly with the number of antennas when perfect knowledge of the wireless channel status is available at the receiver. However, the channel status information (CSI) is never known a prior. Therefore, channel estimation is in great need to play a significant role in MIMO-OFDM systems.

MIMO-OFDM Channel Estimation

To make full use of the spectral efficiency, blind channel estimation methods have been developed. Using second order cycle-stationary statistics or correlative coding or other properties, channel matrix can be estimated just from transmitted data [4]. Despite their advantages such as a gain in capacity, most of blind techniques are not very robust and only allow estimating channel under a number of ambiguities. Furthermore, some methods may have poor convergence and some channels are not identifiable [5].

Traditionally, to learn the channel, some known training signals are required to be sent during some portion of the transmission interval. The training-sequence (TS) based schemes can be divided into training phase and data transmission phase. In the training phase, with the knowledge of the training signal at the transmitter and the received version of the training signal at the receiver, we can estimate the channel matrix using some TS based channel estimation algorithms, such as least square (LS), maximum likelihood (ML), maximum a posterior (MAP) and minimum mean squared error (MMSE) [6] algorithms. Thus the estimated channel matrix is used in the subsequent data transmission phase to enhance the reception performance.

Hence in this thesis, we will restrict our attention to TS based channel estimation.

DS Estimation for MIMO-OFDM Systems

As stated before, the OFDM system is frequency-sensitive due to various factors, such as DS resulting from relative motions. Therefore, it is necessary to estimate DS so as to compensate for the introduced ICI in fast-fading MIMO channels. The DS information is also

required for the estimation of vehicle speed, and can be utilized to improve performance and reduce complexity in adaptive receivers. Many DS estimation methods have been proposed, which can be categorized into several groups, such as the one based on the level crossing rate (LCR) [7], the one based on the auto-correlation [8][9][10][11] and the one based on the ML algorithm [12]. The LCR based methods are not suitable for wide-band communications, since the DS is much smaller than the signal spectrum. While the methods based on auto-correlation can be used for both the narrow-band and wide-band signals, where an accurate calculation of the inverse of Bessel function is required, which may lead to a moderate to a high computational complexity. The ML based methods in general provide high accuracy and also incur a high computational complexity. Taking all these estimation approaches into consideration, we will focus on auto-correlation based schemes in this thesis.

1.3 Motivation and Objectives of the Research

In the preceding sections, the new trends of wireless communications are reviewed. It is shown that the combination of MIMO and OFDM techniques with channel estimation offers promising performance for the forth coming 4G network. However, the corresponding DS or even velocity estimation techniques are necessary. This thesis is concerned with DS estimation using estimates of channel impulse responses (CIRs) for MIMO-OFDM systems.

The first objective of the thesis is to obtain reliable channel estimates from the time-domain MIMO-OFDM channel estimation using optimal TSs in conjunction with the LS algorithm. The second objective is to develop several DS estimation approaches for MIMO-

OFDM systems by exploiting CIR estimates, which are formerly used in SISO-OFDM systems. The performance of the estimation algorithms will be investigated by considering different system parameters and channel conditions. In addition, the proposed algorithms will be compared with each other in terms of performance and computational complexity.

1.4 Organization of the Thesis

This thesis is organized as follows:

Chapter 1: The proceeding chapter provides an overview on the background of next generation wireless communications with MIMO, OFDM and related channel estimation and DS estimation techniques.

Chapter 2: Fundamentals of MIMO-OFDM systems are reviewed, including the basic concepts of wireless channels, the cause of DS and corresponding correlation features, OFDM symbol design and MIMO-OFDM system model.

Chapter 3: The TS based MIMO-OFDM channel estimation that uses LS algorithm is introduced. First, the mean squared error (MSE) of channel estimates is derived, and then optimal pilot sequences are deduced with respect to the MSE, followed by performance studies of the whole system.

Chapter 4: Three auto-correlation function (ACF) based DS estimation algorithms are proposed for i.i.d. MIMO-OFDM systems under Rayleigh channels, by employing channel estimates obtained in Chapter 3. The first method utilizes the first zero-crossing point of ACF, while the other two utilize a partial ACF curve and calculates the maximum DS by polynomial curve fitting or looking up a table of Bessel function. Then the underlying sys-

tem is extended for Rician fading channels, and an estimator which utilizes the periodicity of ACF curve is proposed for the DS of the direct path. The performance of the proposed methods is then evaluated through computer simulations with necessary comparisons.

Chapter 5: This final chapter concludes the whole research and points out some possible directions for future work.

1.5 Contributions

The most significant contributions of this research are summarized as follows:

1. A TS based LS (TSLS) channel estimation approach for MIMO-OFDM systems is studied with plenty of simulation work. Simulations show that such channel estimation scheme is rather reliable and efficient for further DS estimations.

2. Four DS estimation algorithms using the ACF of channel estimates are proposed for uncorrelated MIMO-OFDM systems under both Rayleigh and Rician fading channels. The proposed estimators are analyzed with the enhanced non-linear interpolation schemes being proposed, followed by performance simulations. The estimators are summarized as follows:

    - **Zero-crossing scheme:** It utilizes the first zero-crossing point on the ACF curve, which is estimated by linear interpolation. Simulations show that it is almost noise-insensitive and thus is well suited for general use. Spline interpolation can improve the estimation performance to some extent.

    - **Partial-curve scheme:** It utilizes the properly chosen region of ACF curve for

accuracy improvement, and is implemented by following methods:

- **Polynomial curve fitting:** It uses a 6th-order polynomial to fit the Bessel function with certain progressive deviation. Then the positive and real root of this polynomial is used to calculate the maximum DS. As a higher-order polynomial is required, higher computational complexity is expected.
- **Look-up table:** Instead of calculating the inverse of Bessel function by evaluating the root of high-order polynomial, it searches a pre-stored table of values of Bessel function with controllable precision, which reduces computational time considerably. Computer simulations indicate that this scheme is better than the zero-crossing scheme under moderate channel conditions. Spline interpolation is implemented to compensate for systems with an extremely large DS, which may make it undetectable.

• **Half-period scheme:** Unlike the other three estimators, this scheme is only applicable to direct path DS in Rician fading channels. It utilizes the periodicity of the ACF curve, and makes use of the effective first valley point for DS computation. Simulations show that it is suitable for Rician fading channels with any K-factor and channel conditions. Spline interpolation is a compensation for channels with large DSs.

Chapter 2

Fundamentals of MIMO-OFDM Systems

We have undertaken an overview of the upcoming wireless communication systems in Chapter 1, which provides us with a bright insight into the combination of MIMO and OFDM techniques. In this chapter, we will briefly review the fundamentals of related technologies, including the model of wireless channels, symbol design for OFDM systems, and the concept of DS as well as auto-correlation property of fading channels. Then, we will discuss about the channel and signal models of MIMO-OFDM systems, which will be utilized in the following chapters to develop channel and Doppler frequency shift estimation techniques.

2.1 Basic Concepts of Wireless Channels

2.1.1 Types of Multi-path Fading Channels

In wireless communications, multi-path fading is a common propagation phenomenon, which can be caused by reflection from scatterers such as mountains and buildings. The signals coming from different paths result in multiple delayed versions at the receiver.

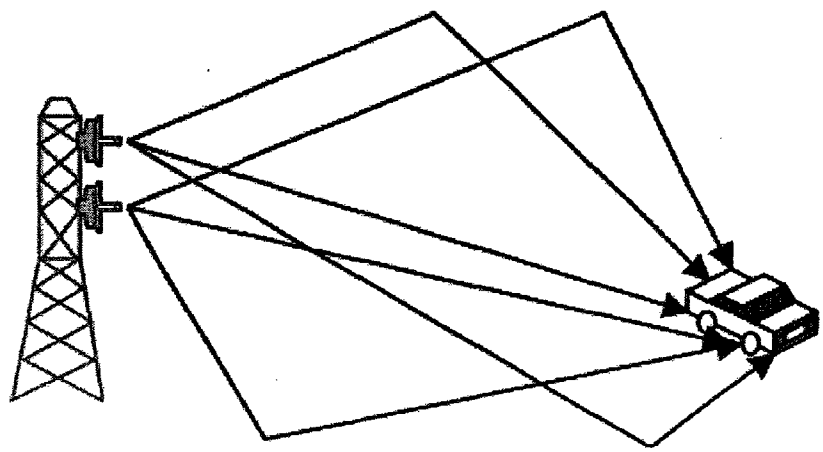

Figure 2.1: Multi-path fading

Fig. 2.1 is a typical example of multi-path propagation between a base-station and a moving vehicle. As can be seen from the figure, the fading process consists of line-of-sight (LOS) and non-line-of-sight (NLOS) fadings, in which LOS fading has a distribution of Rician and NLOS, however, is Rayleigh distributed. In addition, Doppler frequency shift can be incurred by the relative motion between the transmitter and the receiver.

Fading channels can be classified into several groups in terms of fading features.

Slow and Fast Fading Channels

Wireless fading channel is normally modeled as a linear time-variant (LTV) system. The speed of varying with regard to time refers to how fast the magnitude and phase of signals are changing in propagation, which is measured by the coherence time of the channel denoted by $(\Delta t)_c$ and the delay requirement that usually chooses the symbol duration T_s. When $(\Delta t)_c \gg T_s$, the amplitude and phase change caused by the channel can be considered constant over a certain time period, the channel is relative slowly fading compared with signals, which is so called *slow fading*. On the contrary, *fast fading* occurs when the coherence time of the channel is relatively smaller or comparable to that of the symbol duration.

Moreover, the coherence time has been proved to be inverse proportional to the Doppler spread denoted by B_d, i.e.

$$(\Delta t)_c \approx \frac{1}{B_d} \tag{2.1}$$

Hence, the fading speed of channels can be also measured by the Doppler spread. Larger Doppler spread can result in faster fading than that of a smaller one.

Flat and Frequency-selective Fading Channels

Similarly, coherence bandwidth, or $(\Delta f)_c$ is to measure the fading in terms of frequency. In the coherence bandwidth, all frequency components of the signal experience coherent interference. If the coherence bandwidth is smaller than that of the transmit signals, i.e. $(\Delta f)_c < B_s$, the channel is known as *frequency-selective*, as those signals whose frequency components exceed the coherence bandwidth experience uncorrelated fading. And severe

ISI can be introduced at the receiver. On the other hand, the channel is non-selective, or *flat*, when $(\Delta f)_c \gg B_s$, all frequency components of the signal experience the same magnitude of fading.

Besides, we have a useful relation between the coherence bandwidth and the multi-path delay spread:

$$(\Delta f)_c \approx \frac{1}{T_m} \tag{2.2}$$

which indicates that the fading channel can be also measured by the delay spread. With $T_s = 1/B_s$ as well as (2.2), we can derive that, the channel is frequency-selective when $T_m \ll T_s$, and on the contrary, $T_m > T_s$ implies flat fading.

Fig. 2.2 and 2.3 summarize the relation between channel parameters and various fading types.

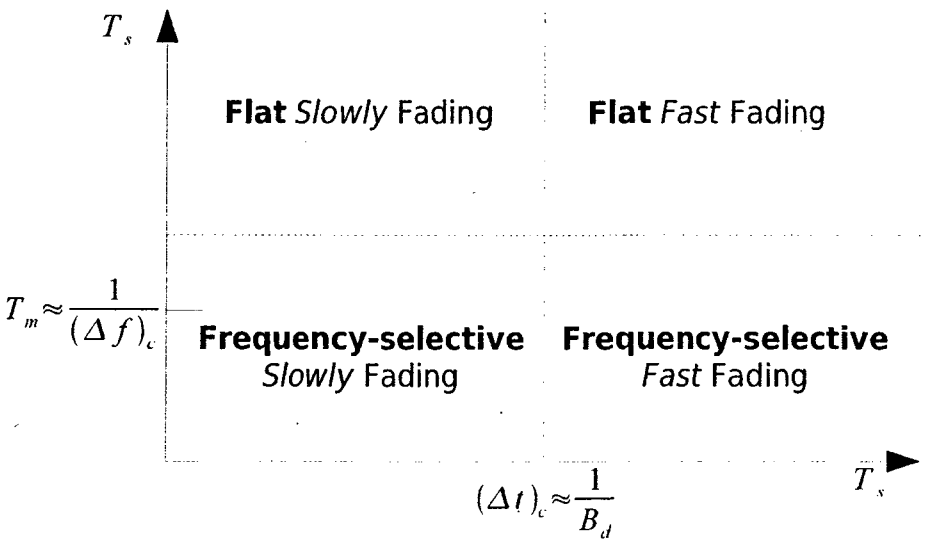

Figure 2.2: Relationship of fading and symbol duration

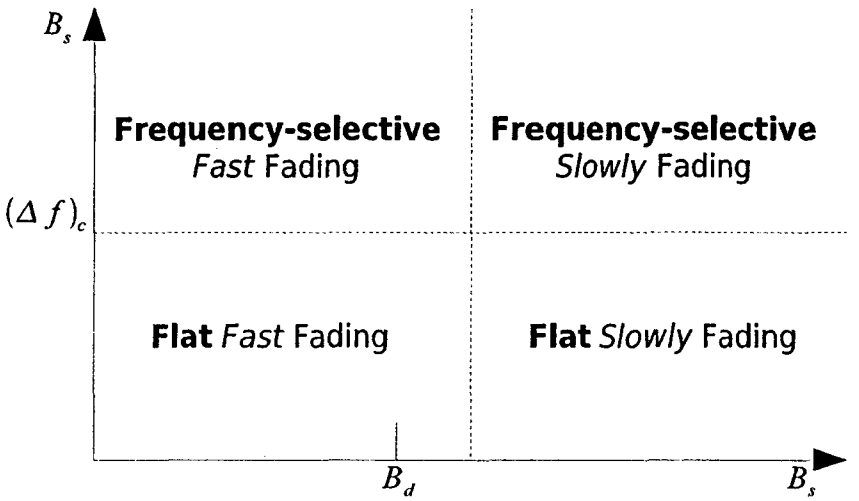

Figure 2.3: Relationship of fading and symbol bandwidth

2.1.2 Fading Channel Model

Fading channel can be considered as a equivalent base-band LTV model. Hence, the CIR at time t can be expressed by [13]

$$h(\tau, t) = \sum_i a_i(t)\delta(\tau - \tau_i(t)) \tag{2.3}$$

where $a_i(t)$ and $\tau_i(t)$ is the complex attenuation and propagation delay at time t of the ith delay path, respectively; and a Dirac function δ is defined by

$$\delta(t) = \begin{cases} 0, & t \neq 0 \\ \infty, & t = 0 \end{cases} \tag{2.4}$$

and

$$\int_{-\infty}^{\infty} \delta(t) = 1 \tag{2.5}$$

Thus, the corresponding output of the channel can be described as

$$\begin{aligned} y(t) &= h(\tau, t) * x(t) \\ &= \int_{-\infty}^{\infty} h(\tau, t) x(t-\tau) d\tau \\ &= \sum_i a_i(t) x(t - \tau_i(t)) \end{aligned} \tag{2.6}$$

where $*$ denotes convolution operation.

For digital implementation, we normally use a discrete time base-band model, the multi-path fading channel is modeled as a linear finite impulse response (FIR) filter. Then, the propagation of such model can be expressed by

$$y_n = \sum_l h_{l,n} x_{n-l} \tag{2.7}$$

where $h_{l,n}$ is denoted as the lth channel tap at time n. Especially, if the path gain a_i and the path delays are time-invariant during a certain time slot, for example, one symbol period, the lth tap can then be simplified to:

$$h_l = \sum_i a_i \operatorname{sinc}(l - \frac{\tau_i}{T}) \tag{2.8}$$

where T is the input sample period to the channel.

Moreover, the CIR $h(t)$ is a composition of multiple scatters and an LOS component (see Fig. 2.4). We use the following model for the multi-path CIR described in the base-band [7]:

$$h(t) = \underbrace{\frac{1}{\sqrt{K+1}} \sum_{i=1}^{I} \alpha_i(t) e^{j[2\pi f_d \cos(\theta_i)t + \phi_i]}}_{Z_1(t)} + \underbrace{\sqrt{\frac{K}{K+1}} e^{j[2\pi f_d \cos(\theta_0)t + \phi_0]}}_{Z_2(t)} \tag{2.9}$$

where the K-factor $K = \mathrm{E}\{|Z_2(t)|^2\}/\,\mathrm{E}\{|Z_1(t)|^2\}$ is defined as the ratio of the power of the LOS component to the NLOS component. α_i denotes normalized amplitudes, satisfying $\sum_{i=1}^{I} \alpha_i^2 = 1$. f_d is the maximum DS, θ_i denotes the angle of arrival (AOA), which is independently and identically distributed (i.i.d.). ϕ_i are independently identically and uniformly distributed phases on $(-\pi, \pi]$. θ_0 and ϕ_0 are the AOA and the initial phase of the LOS component, respectively.

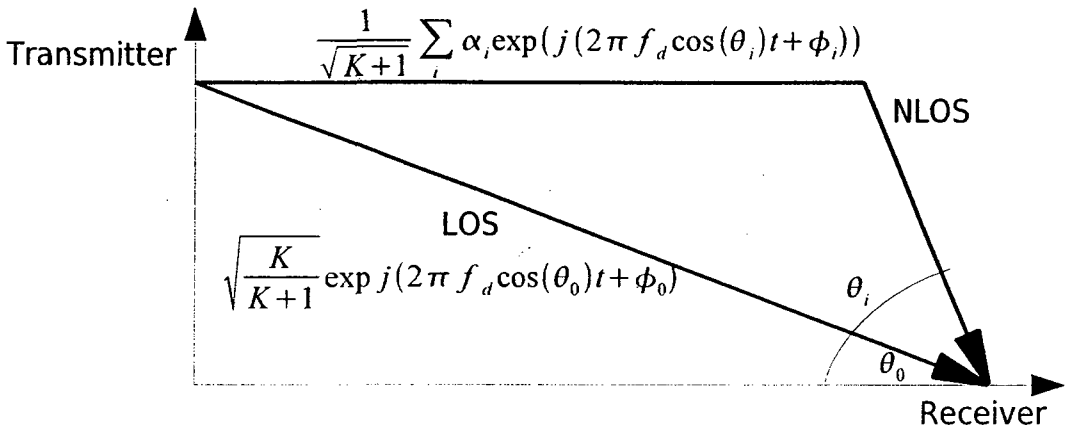

Figure 2.4: The NLOS and LOS paths

Aside from the form expressed in Eq. (2.9), the CIR can be statistically described as

$$h(t) = \sum_{i=1}^{I} \alpha_i(t) e^{-j\psi_i(t)} + \alpha_0(t) e^{-j\psi_0(t)} = \left[h_1(t) + jh_2(t)\right] + \Gamma(t) \tag{2.10}$$

in which

$$\begin{cases} \psi_i = 2\pi f_d \cos\theta_i + \phi_i \\ h_1(t) = \sum_{i=1}^{I} \alpha_i(t) \cos\psi_i(t) \\ h_2(t) = \sum_{i=1}^{I} \alpha_i(t) \sin\psi_i(t) \\ \Gamma(t) = \alpha_0(t) e^{-j\psi_0(t)} \end{cases} \tag{2.11}$$

where $\alpha_0(t)e^{-j\psi_0(t)}$ represents the LOS component, along with $h_1(t) + jh_2(t)$ denoting the

NLOS components. According to the central limit theorem, when I is large, the NLOS component $h_1(t) + jh_2(t)$ tends to be a complex Gaussian random variable, in which $h_1(t)$ and $h_2(t)$ are both Gaussian random variables subjecting to $\mathcal{N}(0, \sigma^2)$. And in turn, $|h(t)|$, the amplitude of a nonzero-mean complex Gaussian process, is Rician distributed. Its probability density function (pdf) is expressed as [14]:

$$f(x) = \underbrace{\frac{x}{\sigma^2}\exp\left(-\frac{x^2}{2\sigma^2}\right)}_{\text{Rayleigh}} \cdot \underbrace{\exp\left(-\frac{\alpha_0^2}{2\sigma^2}\right) \cdot I_0\left(\frac{\alpha_0 x}{\sigma^2}\right)}_{\text{Modifier}}$$

$$= \frac{x}{\sigma^2}\exp\left(-\frac{x^2+\alpha_0^2}{2\sigma^2}\right) I_0\left(\frac{\alpha_0 x}{\sigma^2}\right),\ x \geq 0 \tag{2.12}$$

where α_0^2 denotes the power of the LOS component, $2\sigma^2$ is the total power of all other NLOS scatters, or in another word, $K = \frac{\alpha_0^2}{2\sigma^2}$; and I_0 is the zeroth-order modified Bessel function of the first kind. While in the absence of a LOS component, i.e. $K = 0$, $|h(t)|$ subjects to a Rayleigh distribution with a pdf of

$$f(x) = \frac{x}{\sigma^2}\exp\left(-\frac{x^2}{2\sigma^2}\right) \tag{2.13}$$

The pdf of Rayleigh and Rician distributions are shown in Fig. 2.5.

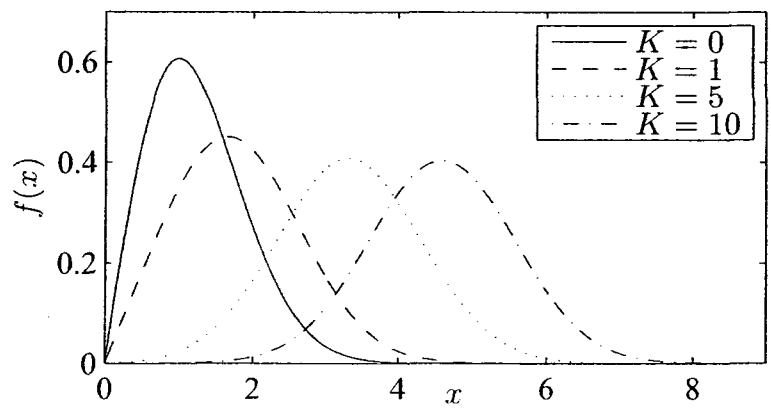

Figure 2.5: The pdf of Rayleigh and Rician distributions when $\sigma = 1$.

2.1.3 Doppler Effect and Auto-correlation of CIR

Concept on DS

As stated before, wireless fading channels are LTV due to relative motion between mobile stations and base-stations, which can introduce frequency offset, or normally DS. DS may lead to severe performance loss especially when frequency-sensitive schemes are employed, such as OFDM.

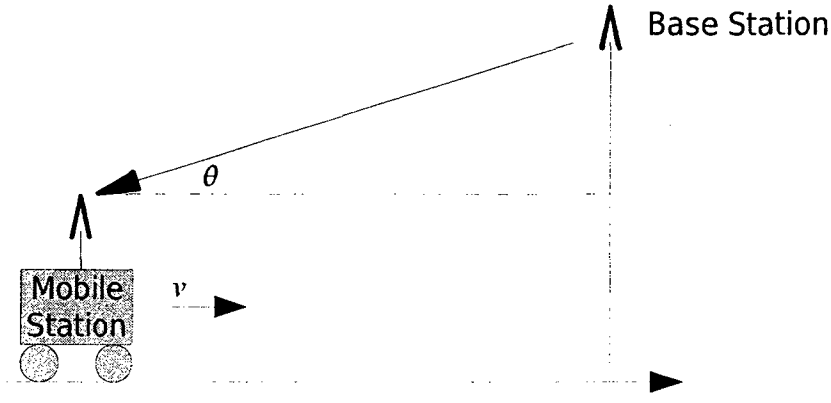

Figure 2.6: Doppler effect

Fig. 2.6 shows a mobile station moving towards a base station with a speed of v. The AOA of the wave relative to the motion direction is denoted by θ. Thus, the received frequency of the mobile station can be expressed by $f_0 + f$, in which f is the DS and can be given by

$$f = \frac{v}{c} f_0 \cos\theta \tag{2.14}$$

where c is the the speed of light, and f_0 is the original frequency of signals. The maximum DS is achieved when $\theta = 0$, i.e.

$$f_d = \frac{v}{c} f_0 \tag{2.15}$$

In addition, if the following conditions [15] are satisfied, the well-known Jakes Doppler power spectrum will have a normalized form (see Fig. 2.7):

$$S(f) = \frac{1}{\pi f_d \sqrt{1 - (\frac{f}{f_d})^2}}, \ |f| \leq f_d \tag{2.16}$$

- The radio waves are horizontally propagated.
- The AOA θ_i of the radio waves are uniformly distributed over $[-\pi, \pi]$ at the receiver.
- The receive antenna has a circular-symmetrical pattern.

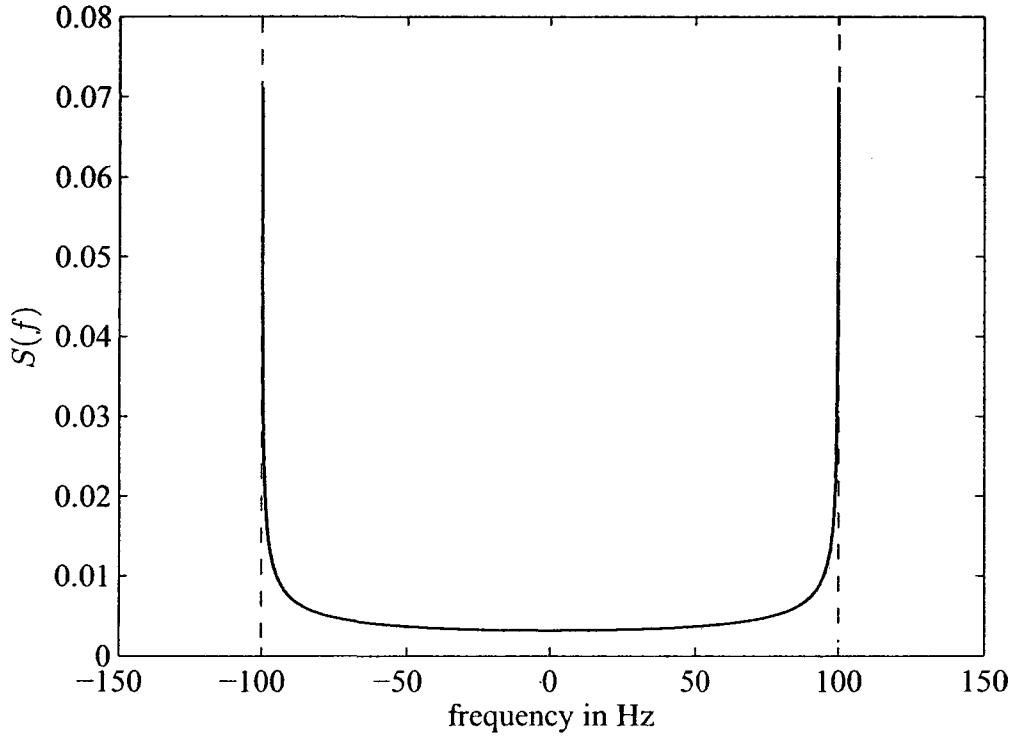

Figure 2.7: Jakes Doppler spectrum, $f_d = 100$ Hz

Moreover, if there exists an LOS component, i.e. Rician fading channel, a modified Doppler power spectrum is given by

$$S(f) + K\delta(f - f_{d,LOS}) \tag{2.17}$$

where $f_{d,LOS} = f_d \cos\theta_0$ denotes the DS of the direct path, and $\delta(\cdot)$ is a Kronecker Dirac function satisfying

$$\delta(x) = \begin{cases} 1, & x = 0 \\ 0, & x \neq 0 \end{cases} \tag{2.18}$$

ACF of CIR

The ACF of CIR $h(t)$ (2.9) can be simply calculated by [7]

$$\begin{aligned} R_{hh}(\tau) &= \mathrm{E}\left\{h(t)h^*(t+\tau)\right\} \\ &= \frac{1}{K+1}\int_{-\pi}^{\pi} p(\theta)e^{-j2\pi f_d \cos(\theta)\tau}d\theta + \frac{K}{K+1}e^{-j2\pi f_d \cos(\theta_0)\tau} \end{aligned}$$

where $p(\theta)$ is the pdf of the AOA θ_i. According to the Jakes' model [16], if θ_i is uniformly distributed on $[-\pi, \pi]$ and also $K = 0$, i.e. Rayleigh fading, then we obtain

$$R_{hh}(\tau) = J_0(2\pi f_d \tau) \tag{2.19}$$

where $J_0(\cdot)$ represents the zeroth-order Bessel function of the first kind. Therefore, the ACF of a Rician distributed CIR can be expressed by

$$R_{hh}(\tau) = \frac{1}{K+1}J_0(2\pi f_d \tau) + \frac{K}{K+1}e^{-j2\pi f_d \cos(\theta_0)\tau} \tag{2.20}$$

Note that the CIR can be also modeled in a complex form of $h(t) = \Re(t) + j\Im(t)$, with $\Re(t)$ and $\Im(t)$ denoting the real and imaginary component of $h(t)$, respectively. As a result, the ACF (see Fig. 2.8) of the real component can be expressed as [11]

$$\begin{aligned} R_{\Re\Re}(\tau) &= \mathrm{E}\left\{\Re(t)\Re(t+\tau)\right\} \\ &= \frac{1}{K+1}J_0(2\pi f_d \tau) + \frac{K}{K+1}\cos(2\pi f_d \cos(\theta_0)\tau) \end{aligned} \tag{2.21}$$

And in the special case of a Rayleigh fading channel, $\Re$ and $\Im$ are both i.i.d. Gaussian random variables. Therefore, their ACFs can be simply obtained by

$$R_{\Re\Re}(\tau) = R_{\Im\Im}(\tau) = J_0(2\pi f_d \tau) \tag{2.22}$$

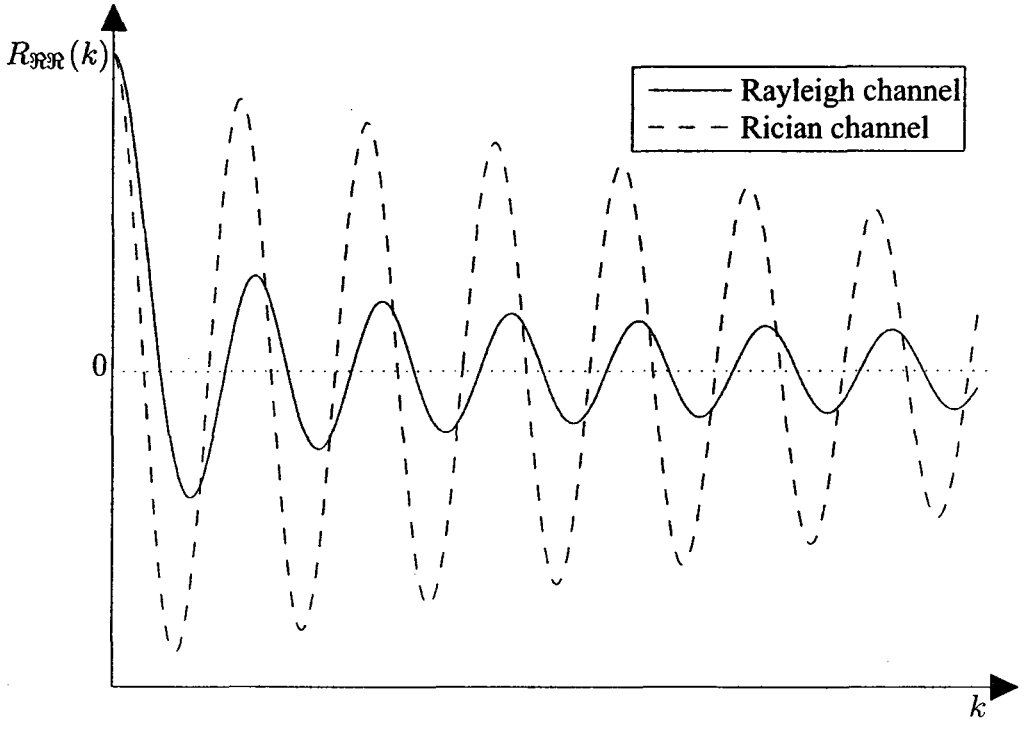

Figure 2.8: ACF of CIR of Rayleigh and Rician channels

2.2 OFDM Systems

OFDM was designed to increase the robustness against frequency-selective fading and multi-path delay, it also increases the frequency spectral efficiency for modern wireless communication systems. In this section, we will take a brief review of the principle of this multi-carrier scheme.

2.2.1 Transceiver

A transmitter diagram of OFDM systems is illustrated in Fig. 2.9. Data stream is demultiplexed into N parallel sub-carriers and then mapped commonly using quadrature amplitude modulation (QAM) or phase-shift keying (PSK). An IFFT is performed thereafter, generating an OFDM symbol in the time domain, which are then appended by a copy of its tail of length L_g. By using digital-to-analogue converters (DACs), the digital signals are converted to the analogue domain. Finally, the analogue signals are modulated at the carrier frequency f_c and transmitted trough the antenna.

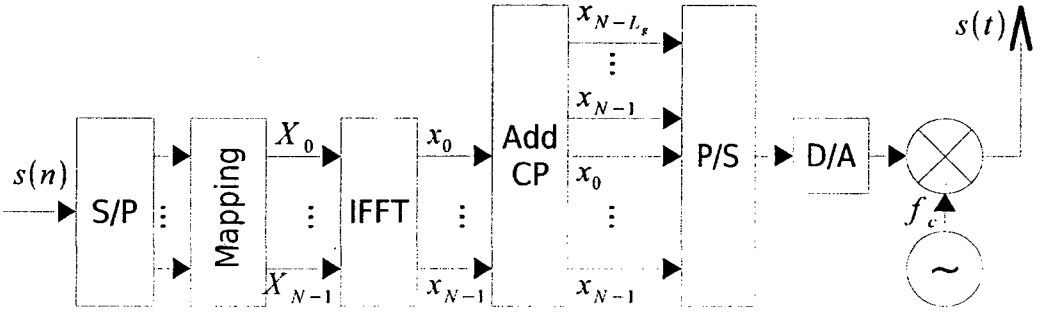

Figure 2.9: The transmitter model of OFDM systems

As shown in Fig. 2.10, the signals that arrive at the receive antenna are demodulated and converted back to the discrete domain. Cyclic prefixes (CP) are then removed, followed by FFT processing resulting in N parallel streams in the frequency domain, which are further detected by a symbol detector. Estimated signals are finally formed into a serial stream.

2.2.2 OFDM Symbol Design

Now we consider a data sequence

$$\mathbf{X} = [X_0, \ldots . X_{N-1}]^T \tag{2.23}$$

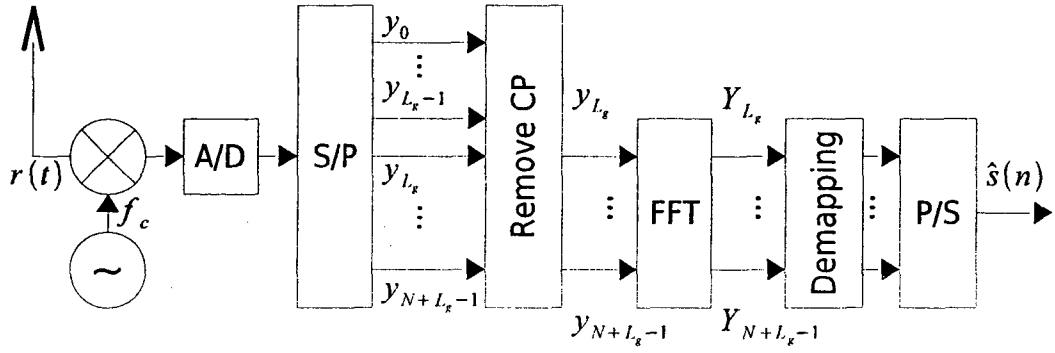

Figure 2.10: The receiver model of OFDM systems

Assume the signals are sampled at $\frac{1}{T}$, thus the entire OFDM symbol duration is NT. After IFFT or OFDM modulation, we obtain the base-band signals in the time domain:

$$x_n = \frac{1}{\sqrt{N}} \sum_{k=0}^{N-1} X_k e^{j2\pi \frac{k}{N} n} \tag{2.24}$$

$$= \frac{1}{\sqrt{N}} \sum_{k=0}^{N-1} X_k e^{j2\pi f_k nT}, \; n \in \{0, \ldots, N-1\} \tag{2.25}$$

where $f_k = \frac{k}{NT}$ is the frequency of the kth sub-carrier. Moreover, the low-pass equivalent OFDM signal can be expressed as

$$s(t) = \frac{1}{\sqrt{N}} \sum_{k=0}^{N-1} X_k e^{j2\pi f_k t}, \; 0 \leq t < NT \tag{2.26}$$

Orthogonality of OFDM Signals

In OFDM systems, the sub-carrier frequencies are chosen such that the sub-carriers are orthogonal to each other as shown in Fig. 2.11, each tone represents a sub-carrier, and the ICI is eliminated by overlapping these sinc shaped frequency spectra. The orthogonality requires that each sub-carrier has exactly an integer number of cycles in the FFT interval, and the number of cycles between adjacent sub-carriers differs by exactly one [17]. This

property can be expressed as

$$\int_0^{NT} \left(e^{j2\pi \frac{k_1}{NT} t}\right)\left(e^{j2\pi \frac{k_2}{NT} t}\right)^* dt = \int_0^{NT} e^{j2\pi \frac{(k_1-k_2)}{NT} t} dt = \delta_{k_1,k_2}$$

where $(\cdot)^*$ denotes the complex conjugate operator, and δ is the Kronecker delta function defined as

$$\delta_{k_1,k_2} = \begin{cases} 1, & k_1 = k_2 \\ 0, & k_1 \neq k_2 \end{cases} \tag{2.27}$$

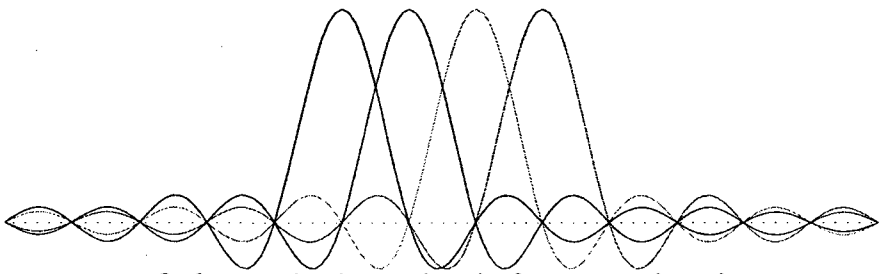

Orthogonal sub−carriers in frequency domain

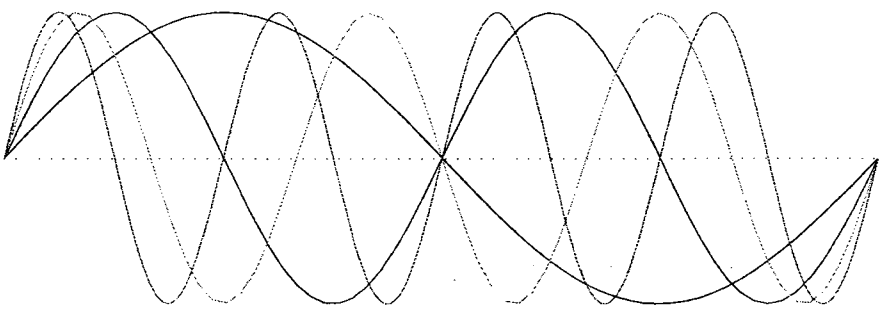

Subcarriers within one OFDM symbol

Figure 2.11: Orthogonal subcarriers in the frequency and time domain

By overlapping, high spectral efficiency is possible. However, accurate frequency synchronization between the receiver and the transmitter are required. Orthogonality will be destroyed for a small frequency deviation, which causes ICI. Frequency offsets are typi-

cally caused by mismatched transmitter and receiver oscillators, or by DS due to relative movement. Moreover, Doppler effect worsens as motion speed increases. Hence, DS information is required for accurate signal recovery.

Cyclic Prefix

A CP of length L_g, which is a cyclic extension of the OFDM symbol, is inserted before transmission in order to avoid ISI in multi-path fading channels. It also reduces the sensitivity to time synchronization problems. From Fig. 2.9, we can see that the OFDM symbol after CP prefixing can be defined by

$$\bar{\mathbf{x}} = [x_{N-L_g}, \ldots, x_{N-1}, x_0, \ldots, x_{N-1}]^T \tag{2.28}$$

As discussed before, for the linear time invariant (LTI) system, discrete-time base-band model is expressed as

$$y_n = \sum_{l=0}^{L-1} h_l x_{n-l} \tag{2.29}$$

Assuming $L_g = L$ and taking (2.28) into consideration, then (2.29) can be rewritten as

$$y_n = \sum_{l=0}^{L-1} h_l x_{[(n-L-l) \mod N]} \tag{2.30}$$

We can rewrite (2.30) as

$$y_n = h_n \otimes x_n \tag{2.31}$$

with $\otimes$ denoting the cyclic convolution. By taking the DFT of both sides of (2.31), we thus obtain

$$\mathrm{DFT}(y_n) = \mathrm{DFT}(h_n \otimes x_n) = \mathrm{DFT}(h_n) \cdot \mathrm{DFT}(x_n)$$

Or

$$Y_k = H_k X_k, \; k \in \{0, \ldots, N-1\} \tag{2.32}$$

where

$$H_k = \sum_{l=0}^{L-1} h_l e^{-j2\pi \frac{l}{N} k} \tag{2.33}$$

Therefore, a multi-path channel is converted into N parallel sub-channels in the frequency domain, which can also simplify the receiver.

2.3 MIMO-OFDM Systems

2.3.1 MIMO Channel Model

MIMO-OFDM scheme is designed for broadband wireless communications. Since the signal bandwidth is always larger than the coherence bandwidth, the channel can be viewed as frequency-selective.

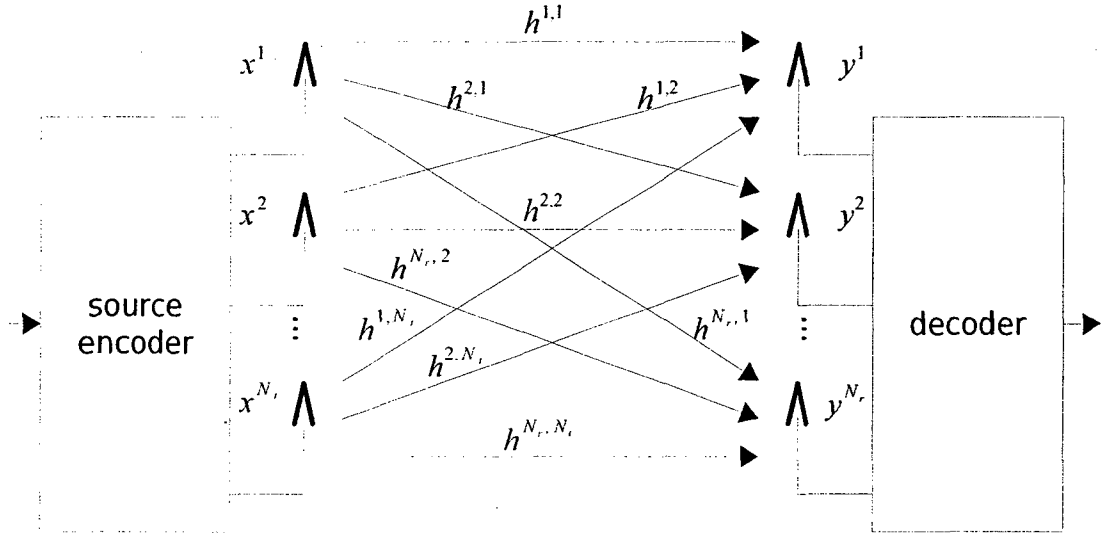

Figure 2.12: MIMO channel with N_t transmit antennas and N_r receive antennas

Fig. 2.12 shows a typical block diagram of a MIMO system. The received signal vectors

can be simply represented by

$$\mathbf{y} = \mathbf{H}\mathbf{x} + \mathbf{v} \tag{2.34}$$

where $\mathbf{y}$ and $\mathbf{x}$ are the received and the transmitted signal vectors, respectively; $\mathbf{H}$ denotes the $N_r \times N_t$ channel matrix of the MIMO system, with $\mathbf{v}$ representing the noise vector at the receiver. We assume that the noise in this thesis is always an additive white Gaussian noise (AWGN). Each link between a pair of transmit and receive antennas can be regarded as an L-tap FIR filter. Moreover, the channel can usually be assumed constant over the transmission of one OFDM symbol, though it may vary for different symbols, which is also known as the quasi-static model. Hence, we define a channel matrix for the lth tap as:

$$\mathbf{H}_l(m) = \begin{bmatrix} h_l^{1,1}(m) & h_l^{1,2}(m) & \dots & h_l^{1,N_t}(m) \\ h_l^{2,1}(m) & h_l^{2,2}(m) & \dots & h_l^{2,N_t}(m) \\ \vdots & \vdots & \ddots & \vdots \\ h_l^{N_r,1}(m) & h_l^{N_r,2}(m) & \dots & h_l^{N_r,N_t}(m) \end{bmatrix}_{N_r \times N_t} \tag{2.35}$$

where $h_l^{n_r n_t}(m)$ stands for the CIR between the n_rth receive antenna and the n_tth transmit antenna of the lth tap during the mth OFDM symbol.

2.3.2 MIMO-OFDM System Model

Fig. 2.13 shows a block diagram of a simple MIMO-OFDM transmitter, which consists of N_t independent links. For the mth OFDM symbol, we define

$$\mathbf{X}^{n_t}(m) = \left[X_1^{n_t}(m), \dots, X_N^{n_t}(m)\right]^T \tag{2.36}$$

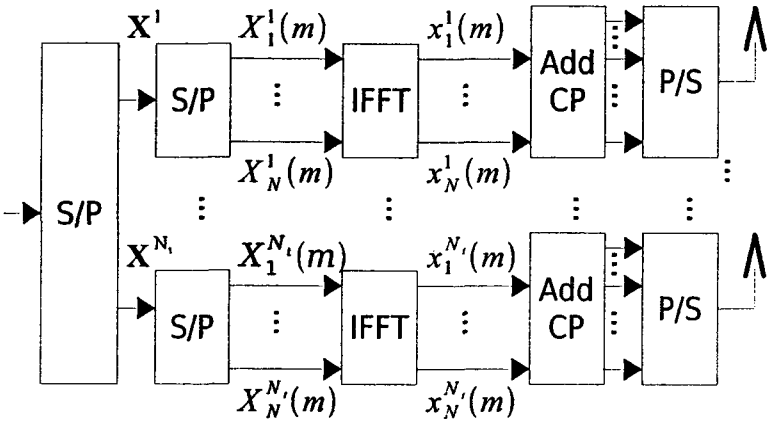

Figure 2.13: MIMO-OFDM transmitter

as the input frequency-domain signals for the IFFT unit, where K denotes the number of sub-carriers. Similarly, the output signals of the IFFT processor can be defined as

$$\mathbf{x}^{n_t}(m) = \left[x_1^{n_t}(m), \ldots, x_N^{n_t}(m)\right]^T \tag{2.37}$$

which is normally called time-domain signals. After adding a CP, the signals are transmitted from the n_tth antenna.

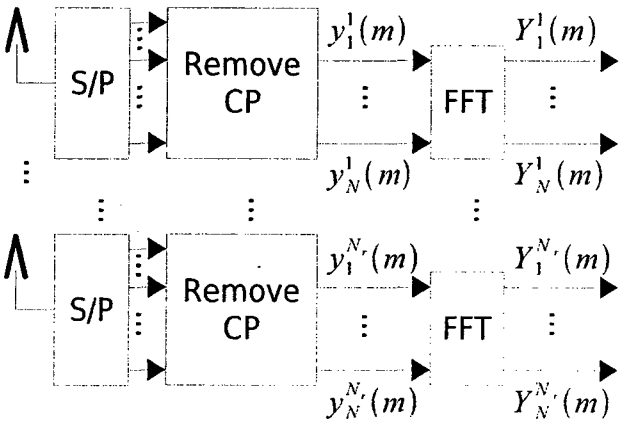

Figure 2.14: MIMO-OFDM receiver

Fig. 2.14 shows a diagram of a simple MIMO-OFDM receiver, which consists of N_r receive antennas. For the n_rth link, samples of the received signals corresponding to the

CPs are removed first. Then, the received time-domain signals can be expressed as

$$\mathbf{y}^{n_r}(m) = \left[y_1^{n_r}(m), \ldots, y_N^{n_r}(m)\right]^T \tag{2.38}$$

After FFT processing, we finally obtain the received signals in the frequency domain:

$$\mathbf{Y}^{n_r}(m) = \left[Y_1^{n_r}(m), \ldots, Y_N^{n_r}(m)\right]^T \tag{2.39}$$

With the received signals, the MIMO channel can be estimated via various schemes. The information data can then be recovered by the MIMO-OFDM decoder based on the estimated channel matrix.

2.3.3 MIMO-OFDM Signal Model

First, we take a look at the signal model in the time domain. Assuming that the channel is constant during one OFDM symbol, and the CP is perfectly set to be no less than the channel length. For the mth OFDM symbol, the signal model for the frequency-selective fading channel can be expressed as

$$y_n^{n_r}(m) = \sum_{n_t=1}^{N_t} h_n^{n_r,n_t}(m) * x_n^{n_t}(m) + v_n^{n_r}(m) \tag{2.40}$$

$$= \sum_{n_t=1}^{N_t} \sum_{l=0}^{L-1} h_l^{n_r,n_t}(m) x_{n-l}^{n_t}(m) + v_n^{n_r}(m) \tag{2.41}$$

where n denotes the discrete time index, and $v_n^{n_r}(m)$ is the spatial-temporally uncorrelated noise with zero mean and variance of σ_v^2. We can also rewrite (2.40) in a common matrix form as

$$\mathbf{y}_n(m) = \sum_{l=0}^{L-1} \mathbf{H}_l(m)\mathbf{x}_{n-l}(m) + \mathbf{v}_n(m) \tag{2.42}$$

where

$$\mathbf{x}_n(m) = \left[x_n^1(m), \ldots, x_n^{N_t}(m)\right]^T \tag{2.43}$$

$$\mathbf{y}_n(m) = \left[y_n^1(m), \ldots, y_n^{N_r}(m)\right]^T \tag{2.44}$$

$$\mathbf{v}_n(m) = \left[v_n^1(m), \ldots, v_n^{N_r}(m)\right]^T, \ \mathrm{E}\left\{\mathbf{v}_i(m)\mathbf{v}_j^H(m)\right\} = \sigma_v^2 \delta_{i,j}\mathbf{I} \tag{2.45}$$

where $(\cdot)^H$ denotes Hermitian or conjugate transpose, $\mathbf{I}$ is an identity matrix.

Now we derive the signal model in the frequency domain. After the CP is removed, the received signal at the n_rth receive antenna, which is defined in (2.38), can be rewritten as [18]

$$\mathbf{y}^{n_r}(m) = \sum_{n_t=1}^{N_t} \mathbf{H}_{cir}^{n_r,n_t}\mathbf{F}^H\mathbf{X}^{n_t}(m) + \mathbf{v}^{n_r}(m) \tag{2.46}$$

where $\mathbf{H}_{cir}^{n_r,n_t}$ is an $N \times N$ circulant matrix with the first column given by $\left[(\mathbf{h}^{n_r,n_t}(m))^T, \mathbf{0}_{1\times(N-L)}\right]^T$, with $\mathbf{h}^{n_r,n_t}(m) = \left[h_0^{n_r,n_t}(m), \ldots, h_{L-1}^{n_r,n_t}(m)\right]^T$; $\mathbf{v}^{n_r}(m) = \left[v_1^{n_r}(m), \ldots, v_N^{n_r}(m)\right]^T$ is the spatial-temporally uncorrelated noise vector, and $\mathbf{F}$ is the $N \times N$ unitary DFT matrix, where the entries are defined as

$$F_N^{kn} = e^{-j2\pi\frac{nk}{N}} \tag{2.47}$$

By using the eigendecomposition [13], $\mathbf{H}_{cir}^{n_r,n_t}(m)$ can be further expressed as:

$$\mathbf{H}_{cir}^{n_r,n_t}(m) = \mathbf{F}^H \operatorname{diag}\left\{\sqrt{N}\mathbf{F}\left[(\mathbf{h}^{n_r,n_t}(m))^T, \mathbf{0}_{1\times(N-L)}\right]^T\right\}\mathbf{F} \tag{2.48}$$

After taking the DFT of both sides of (2.46), we can obtain the signal model in the frequency domain as

$$\mathbf{Y}^{n_r}(m) = \sum_{n_t=1}^{N_t} \operatorname{diag}\left\{\sqrt{N}\mathbf{F}\cdot\left[(\mathbf{h}^{n_r,n_t}(m))^T, \mathbf{0}_{1\times(N-L)}\right]^T\right\}\mathbf{X}^{n_t}(m) + \mathbf{V}^{n_r}(m) \tag{2.49}$$

where $\mathbf{V}^{n_r}(m) = \mathbf{F}\mathbf{v}^{n_r}(m)$.

2.3.4 Recovery of MIMO-OFDM Signals

Since the MIMO-OFDM system can be divided into independent flat-fading MIMO sub-systems for different sub-carriers, the algorithm for flat-fading MIMO channel receiver can be used for each MIMO sub-system. Based on the estimated channel matrix, the optimum detection algorithm is ML algorithm, which chooses

$$\hat{\mathbf{x}} = \arg\left\{ \min_{\mathbf{x}\in\{\mathbf{x}_1,\ldots,\mathbf{x}_{C^{N_t}}\}} ||\mathbf{y} - \mathbf{H}\mathbf{x}||^2 \right\}$$

where C represents the constellation size. Since this algorithm needs a lot of searching, it is one of the most complex detection methods.

Zero-forcing (ZF) algorithm is the simplest one. The information data are detected by using pseudo-inverse of the channel as [19]

$$\hat{\mathbf{x}} = \mathbf{H}^{\dagger}\mathbf{y} = (\mathbf{H}^H\mathbf{H})^{-1}\mathbf{H}^H\mathbf{y}$$

where $(\cdot)^{\dagger}$ represents matrix pseudo inverse.

And MMSE algorithm is another linear detection algorithm, which has an intermediate computational complexity [6]

$$\hat{\mathbf{x}} = \mathbf{H}^{\dagger}\mathbf{y} = \left(\frac{1}{\mathrm{SNR}}\mathbf{I}_{N_r} + \mathbf{H}^H\mathbf{H}\right)^{-1}\mathbf{H}^H\mathbf{y}$$

From these methods, we can conclude that the CSI is needed for signal recovery, and therefore a channel estimation has to be done a prior.

2.4 Conclusion

In this chapter, we started with a brief description of general wireless fading channels as well as the corresponding properties of each fading model. We have then discussed the ACF of Rayleigh and Rician fading channels and stated the possibility of using the ACF for DS estimation. The OFDM symbol transmission principle was then discussed along with CP and ISI elimination. The combination of MIMO and OFDM techniques, i.e., MIMO-OFDM systems, including channel and signal models and MIMO-OFDM transceivers were also reviewed.

Chapter 3

Training based LS Channel Estimation for MIMO-OFDM Systems

In this chapter, we investigate a TSLS channel estimation algorithm [20] for MIMO-OFDM systems. We start with an analysis of LS channel estimation in the time domain. The MSE of channel estimates is then used for the derivation of optimal pilots. Simulations are performed to show the reliability and efficiency of the channel estimation approach.

3.1 LS Channel Estimation Using TSs

In this section, we introduce a TSLS channel estimation in the time domain. Optimal pilots at specific sub-carriers are employed for the estimation of the time-domain channel $\mathbf{H}_l$, $(l = 0, 1, \ldots, L-1)$. With a few or even a single OFDM symbol, accurate channel estimates can be obtained.

Fig. 3.1 shows a block diagram of a simplified transmitter of a MIMO-OFDM system

with an architecture of VBLAST [13]. The data stream is firstly encoded and mapped by a QPSK modulator, and then divided into N_t sub-carriers followed by optimal pilots insertion before IFFT processing or OFDM modulation. The modulated streams are padded by CP of length L_g in each link before transmission. Normally, the length of CP is assumed to be no less than the maximum path delay L of all channels for the robustness against the ISI.

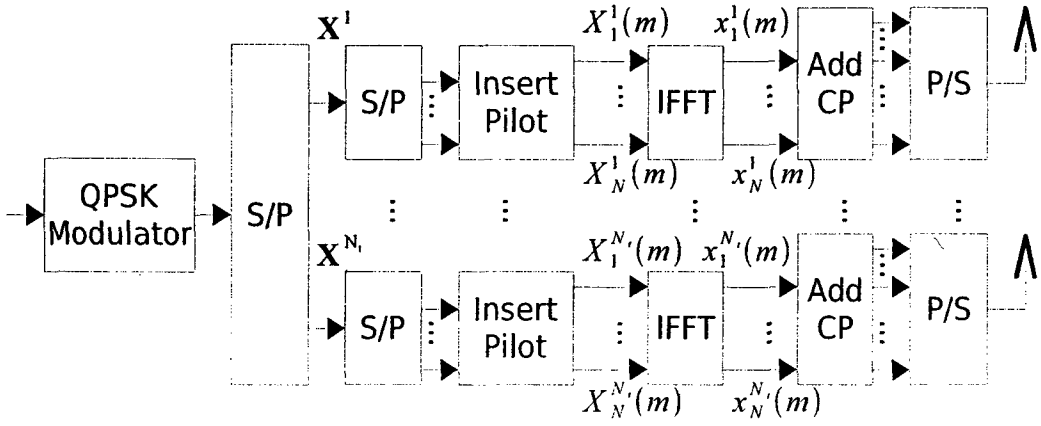

Figure 3.1: MIMO-OFDM transmitter with optimal pilots

Fig. 3.2 is a diagram of a MIMO-OFDM receiver with N_r receive antennas. The received signals, in which CPs have been removed, pass through FFT processing or OFDM demodulation module. Then training pilots are extracted in conjunction with known transmitted TSs for the LS channel estimation. Finally, the channel estimates are further utilized for DS estimation, which will be discussed in Chapter 4.

Here, we assume that the pilots are inserted at N_p out of N sub-carriers of each OFDM symbol that carries the pilot signals. The transmitted pilot vectors of the mth OFDM symbol at each antenna can be written as

$$\mathbf{X}_p^{n_t}(m) = \left[X_{p,1}^{n_t}(m), \ldots, X_{p,N_p}^{n_t}(m)\right]^T \tag{3.1}$$

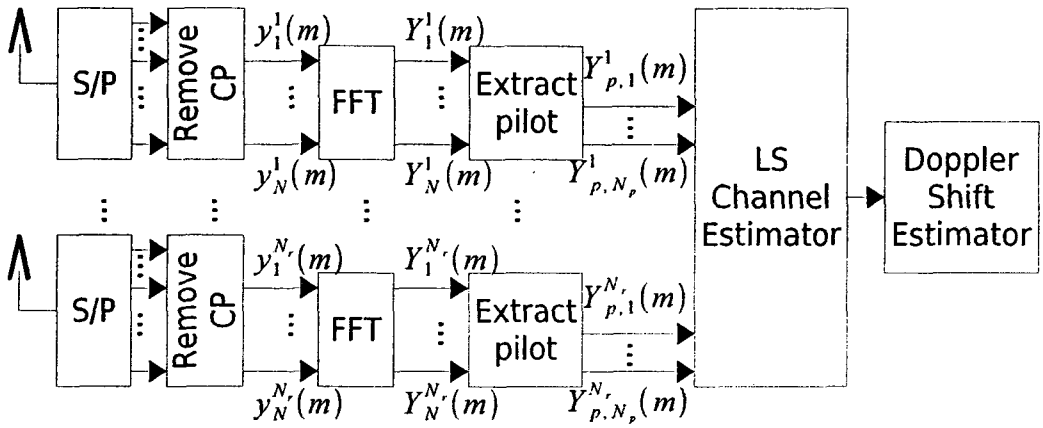

Figure 3.2: MIMO-OFDM receiver with TSLS channel estimator and DS estimator

Similarly, the received pilot vectors in the corresponding pilot sub-carriers are given by

$$\mathbf{Y}_p^{n_r}(m) = \left[Y_{p,1}^{n_r}(m), \ldots, Y_{p,N_p}^{n_r}(m)\right]^T \tag{3.2}$$

We define a matrix $\mathbf{F}_p(m)$ of size $N_p \times L$, which is $\sqrt{N}$ times the first L columns and the N_p rows corresponding to the pilot sub-carriers of a $N \times N$ unitary DFT matrix $\mathbf{F}$ for the mth OFDM symbol, Eq. (2.49) can now be rewritten for the pilot sub-carriers as

$$\mathbf{Y}_p^{n_r}(m) = \sum_{n_t=1}^{N_t} \mathbf{X}_{p,diag}^{n_t}(m)\mathbf{F}_p(m)\mathbf{h}^{n_r,n_t}(m) + \mathbf{V}_p^{n_r}(m) \tag{3.3}$$

where $\mathbf{X}_{p,diag}^{n_t}(m) = \text{diag}\left(\mathbf{X}_p^{n_t}(m)\right)$, and $\mathbf{V}_p^{n_r}(m)$ is the noise vector corresponding to the pilot sub-carriers.

Assume that the pilots are transmitted over g consecutive OFDM symbols, $m \in \{0, \ldots, g-1\}$. Thus, the total number of pilots is $g \times N_p$. Also in the LS algorithm, it is assumed that the channel remains unchanged during these g consecutive OFDM symbols. Therefore, the index m for $\mathbf{h}^{n_r,n_t}(m)$ can be omitted. The model of (3.3) can be then rewritten as

$$\mathbf{Y}_p^{n_r} = \mathbf{A}\mathbf{h}^{n_r} + \mathbf{V}_p^{n_r} \tag{3.4}$$

where

$$\mathbf{Y}_p^{n_r} = \left[(\mathbf{Y}_p^{n_r}(0))^T, \ldots, (\mathbf{Y}_p^{n_r}(g-1))^T\right]^T$$

$$\mathbf{V}_p^{n_r} = \left[\mathbf{V}_p^{n_r}(0), \ldots, \mathbf{V}_p^{n_r}(g-1)\right]^T$$

$$\mathbf{h}^{n_r} = \left[(\mathbf{h}^{n_r,1})^T, \ldots, (\mathbf{h}^{n_r,N_t})^T\right]^T$$

$$\mathbf{A} = \begin{bmatrix} \mathbf{X}_{p,diag}^1(0)\mathbf{F}_p(0) & \cdots & \mathbf{X}_{p,diag}^{N_t}(0)\mathbf{F}_p(0) \\ \vdots & \ddots & \vdots \\ \mathbf{X}_{p,diag}^1(g-1)\mathbf{F}_p(g-1) & \cdots & \mathbf{X}_{p,diag}^{N_t}(g-1)\mathbf{F}_p(g-1) \end{bmatrix}_{gN_p \times LN_t}$$

From (3.4), we can verify that if $\mathbf{A}$ has a full column rank of LN_t, which is equivalent to $gN_p \geq LN_t$, the channel for the n_rth antenna can be estimated via the LS approach, yielding a channel estimate

$$\hat{\mathbf{h}}^{n_r} = \mathbf{A}^\dagger \mathbf{Y}_p^{n_r} = \mathbf{h}^{n_r} + \mathbf{A}^\dagger \mathbf{V}_p^{n_r} \tag{3.5}$$

Furthermore, if taking all receive antennas into consideration, we can derive from (3.4) that,

$$\mathbf{Y}_p = \mathbf{A}\mathbf{H} + \mathbf{V}_p \tag{3.6}$$

where matrices $\mathbf{Y}_p = \left[\mathbf{Y}_p^1, \ldots, \mathbf{Y}_p^{N_r}\right]$, $\mathbf{H} = \left[\mathbf{h}^1, \ldots, \mathbf{h}^{N_r}\right]$ and $\mathbf{V}_p = \left[\mathbf{V}_p^1, \ldots, \mathbf{V}_p^{N_r}\right]$. Thus the estimated channel matrix of size $LN_t \times N_r$ can be obtained by

$$\hat{\mathbf{H}} = \mathbf{A}^\dagger \mathbf{Y}_p = \mathbf{H} + \mathbf{A}^\dagger \mathbf{V}_p \tag{3.7}$$

Fig. 3.3 presents a flowchart at the receiver of the TSLS channel estimation scheme.

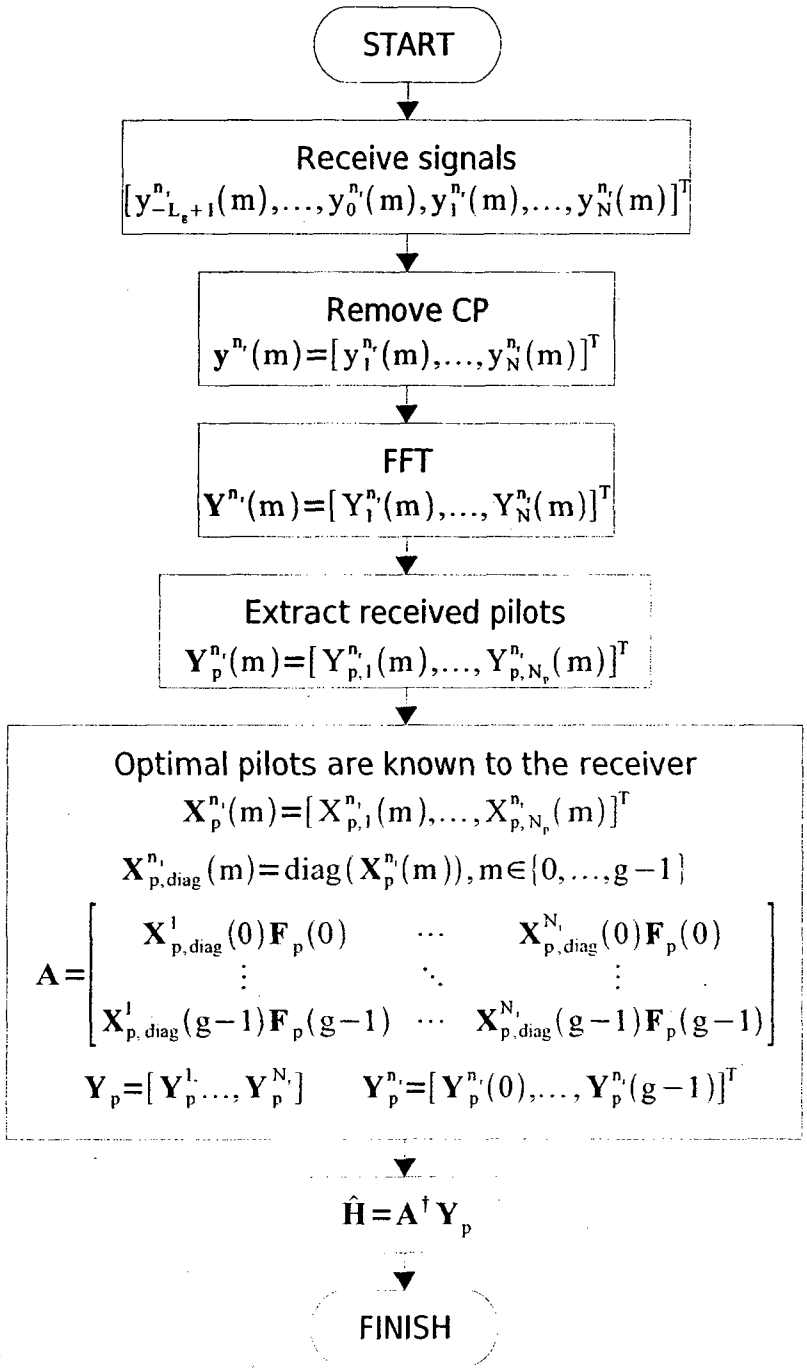

Figure 3.3: Flowchart for LS algorithm at the receiver

3.2 Optimal Pilot Design over Multiple OFDM Symbols

Assume that the transmitting power of training signals is constrained as $||\mathbf{A}||_F^2 = E$, where E is a constant. Then we can find the optimal signals minimizing the channel MSE based on this constraint, which becomes:

$$\min_{\mathbf{A}} J_{LS} = \min_{\mathbf{A}} \mathrm{E}\left\{||\mathbf{H} - \hat{\mathbf{H}}_{LS}||_F^2\right\}, \text{ subject to } ||\mathbf{A}||_F^2 = E$$

where $||\cdot||_F$ denotes Frobenius norm. It has been proved [20] that the pilot is optimal if $\mathbf{A}\mathbf{A}^H = E\mathbf{I}$, which means the optimal training sequences at different transmit antennas must be equally powered, equally spaced and phase shifts orthogonal. Moreover, due to the full column rank requirement of $\mathbf{A}$, we obtain $gN_p \geq LN_t$. Considering FFT, gN_p should also be the power of 2. Therefore, the optimal pilot sequences can thus be derived as [20]

$$X_{p,k}^{n_t}(m) = \sqrt{\frac{E}{gN_p}} e^{-j2\pi \frac{n_{n_t}(m+kg)}{gN_p}} \tag{3.8}$$

where $m \in \{0, \ldots, g-1\}$, $k \in \{1, \ldots, N_p\}$, $n_t \in \{1, \ldots, N_t\}$, $n_{n_t} = (n_t - 1)L$, and $gN_p = 2^{\lceil \log_2(LN_t) \rceil}$. Note $\sqrt{\frac{E}{gN_p}} e^{-j2\pi n_{n_t}(m+kg)/(gN_p)} \cdot c(k)$ is also optimal as long as $c(k)$ is an arbitrary unit modulus sequence ($|c(k)| = 1$), which can be given by

$$c(k) = e^{j2\pi s_k} \tag{3.9}$$

where s_k is uniformly distributed on $[0, 1]$.

For simplicity, we use one trained OFDM symbol for channel estimation, i.e. $g = 1$, in the following section. The optimal TS can now be designed as

$$X_{p,k}^{n_t} = \sqrt{\frac{E}{N_p}} e^{-j2\pi \frac{n_{n_t} k}{N_p}} \cdot c(k) \tag{3.10}$$

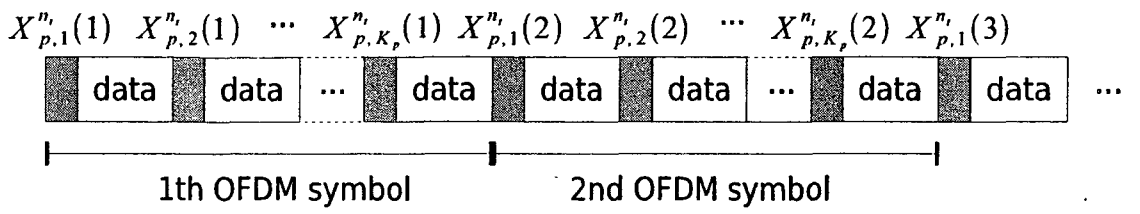

Figure 3.4: Training over a single OFDM symbol

Fig. 3.4 shows the structure of the OFDM symbols at the n_tth transmit antenna. Each OFDM symbol consists of N_p equally spaced optimal pilots created by (3.10) and $N - N_p$ data signals. Note the optimal sequences of different symbols are not necessarily the same.

3.3 LS Channel Estimation Performance of MIMO-OFDM Systems

In this section, different system parameters are used to investigate the performance of the TSLS channel estimation for MIMO-OFDM systems. We consider a MIMO-OFDM system with 2 transmit and 4 receive antennas. A fading channel modeled by an 8-tap MIMO-FIR filter is assumed, where each tap corresponds to a 4 by 2 random matrix whose elements are i.i.d. complex random variables with a maximum DS at 100 Hz. The signals are sampled at 1 MHz and modulated by QPSK, 128 sub-carriers are applied thereafter, which contains 16 optimal pilots. A CP of length $L_g = 8$ is then padded for each OFDM symbol. Note the optimal pilot sequences are designed over one OFDM symbol and also known a prior at the receiver. In the first four experiments, a Rayleigh fading channel model is assumed. While in the last experiment, the TSLS channel estimator is examined under both Rayleigh

and Rician fading channels with different K-factors. Besides, the SNR is defined as

$$\text{SNR} = \frac{LN_t\sigma_h^2 E_b}{\sigma_n^2} \tag{3.11}$$

where σ_n^2 and σ_h^2 denote the averaged power of the AWGN and the path gains, respectively; and also the power of transmitted signals is denoted by E_b.

Another thing should be noted is, in the previous sections, a quasi-static channel model, that is time-invariant over one OFDM symbol, was assumed for simplicity. However, the real wireless channels are time-varying. To be practical, the upcoming simulations are carried out under time-varying fading channels. As a result, due to Doppler effect caused by relative movement between the transmitter and the receiver, ICI at the receiver is expected to cause estimation error.

3.3.1 Experiment 1: Effect of Antenna Configurations

This experiment investigates the channel estimation performance for systems with different antenna configurations varying from $N_t \times N_r = 1 \times 1$ to $N_t \times N_r = 2 \times 4$. Fig. 3.5 shows the MSE of channel estimate versus SNR for each antenna configuration. Here, the MSE is calculated by

$$\text{MSE} = \frac{1}{M}\sum_{n_r=1}^{N_r}\sum_{n_t=1}^{N_t}\sum_{l=0}^{L-1}|\hat{h}_l^{n_r,n_t}(m) - h_l^{n_r,n_t}(m)|^2 \tag{3.12}$$

where $M = N_r \times N_t \times L$, and $\hat{h}_l^{n_r,n_t}(m)$ denotes the estimated CIR.

As expected, with the increase of SNR, a better MSE performance can be achieved. Obviously, the data rate or system capacity can be increased by employing more transmit antennas. However, as defined in (3.11), σ_n^2 is supposed to be raised when more transmit

antennas are in use for a specific SNR. As a result, a 3 dB performance loss is noticed in the 2 transmit antenna schemes compared with the 1 transmit antenna counterparts with the same number of receive antennas. It is also clear that, a 3 dB gain is achieved when the number of receive antennas is doubled, which is independent of the number of transmit antennas. Therefore, in the following experiments we focus on the 2 × 4 MIMO channel which will be further studied in Chapter 4.

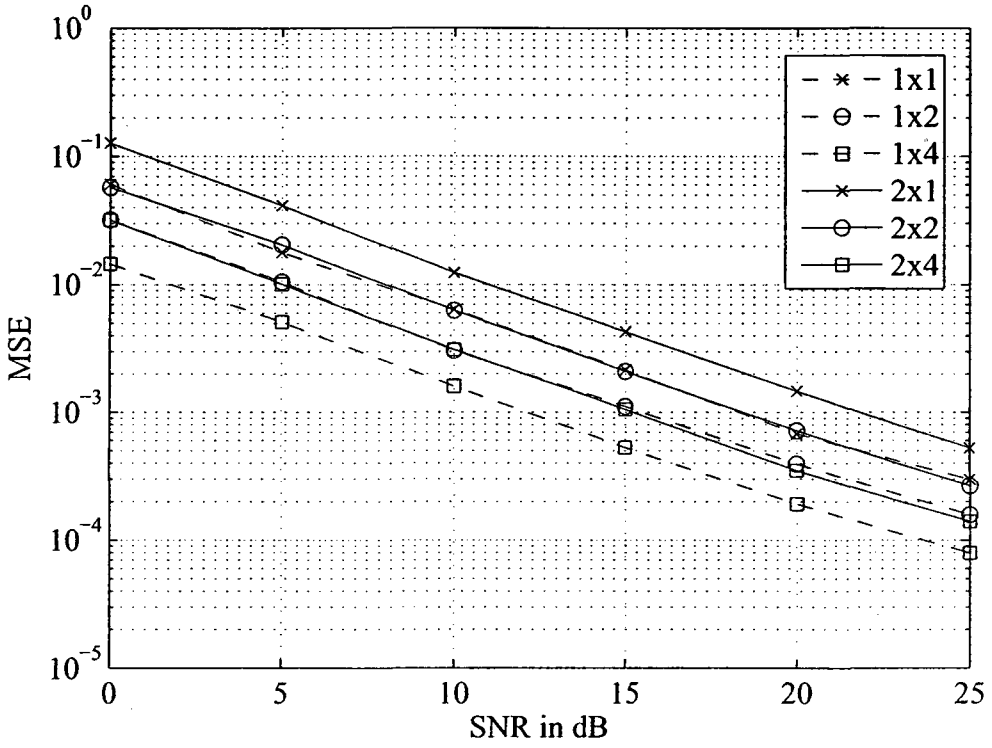

Figure 3.5: MSE versus SNR with different antenna configurations

3.3.2 Experiment 2: Effect of Guard Interval

In this experiment, the channel estimation performance with different guard intervals is investigated. As has been pointed out, to decrease the effect of ISI, a CP with a length of L_g

that is at least equal to the channel length L should be used. Thus, L_g is set between 0 and 10. Fig. 3.6 shows the MSE versus SNR plots for different guard lengths $L_g \in \{0, 4, 6, 8, 10\}$. It is seen that a short CP with length that is less than the channel length $L = 8$ leads to a poor channel estimation results due to the occurrence of ISI. On the other hand, a CP length that is larger than the channel length does not help to improve channel estimation. Therefore, the best trade-off in view of the channel estimation performance and the spectral efficiency is $L_g = L$.

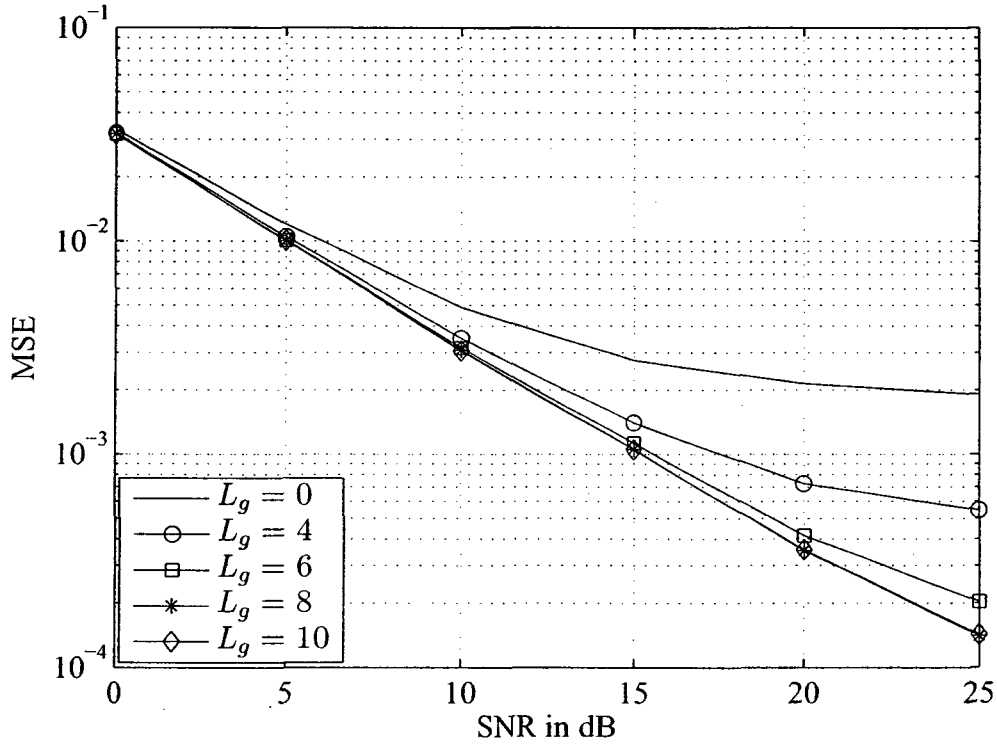

Figure 3.6: MSE versus SNR with different guard lengths

3.3.3 Experiment 3: Effect of Optimal Pilots

In this experiment, we investigate the performance of channel estimator by using different number of optimal pilots, $N_p \in \{8, 15, 16, 32, 64, 128\}$. Fig. 3.7 depicts the MSE versus SNR plots when the number of optimal pilots used varies from 8 to 128.

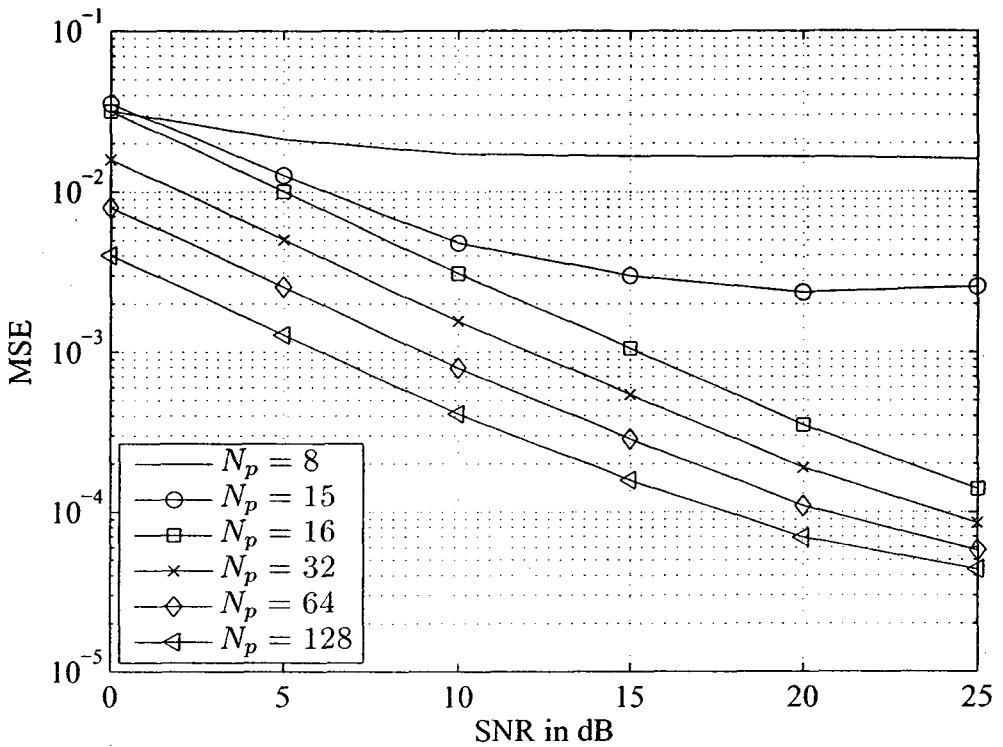

Figure 3.7: MSE versus SNR with different number of optimal pilots

Simulation results show that as we increase the number of pilots, the performance is improved noticeably. In particular, when 128 sub-carriers of each OFDM symbol are replaced by 128 optimal pilots, the best performance is achieved. It should be mentioned that, according to the criterion of optimal pilot design, we have $N_p \geq LN_t$, where N_p is the number of pilots, L and N_t are the channel length and the number of transmit antennas, respectively.

In this experiment, we have set $L = 8$ and $N_t = 2$, which suggest that a minimum of 16 optimal pilots are required for better channel estimation performance. Therefore, in this particular case, the MSE with respect to $N_p = 8$ or $N_p = 15$ is not acceptable. It is also interesting to note that, the MSE is twice better in the range of 0 to 20 dB SNR when N_p is doubled and $N_p \geq LN_t$, which means that, more optimal pilots can significantly improve the estimation results at low to moderate SNRs when $N_p \geq LN_t$. At a higher SNR level, the MSE improvement is less significant with the increase of pilot length.

3.3.4 Experiment 4: Effect of Maximum DS

In this experiment, we examine again the MSE performance of the channel estimator as a function of the SNR but with various DS as well as sample durations. Fig. 3.8 shows the channel estimation results with DS ranging between 0 Hz and 1000 Hz, along with a sample rate of 1 MHz. The estimation performance at small f_ds almost keeps unchanged, which implies that the MIMO channel can be regarded as constant or quasi-static over an OFDM symbol. However, a MIMO channel with a maximum DS of more than 100 Hz can lead to performance degradation, since the channel within one OFDM symbol can no longer be regarded as quasi-static, i.e. the channel relatively fades faster. In addition, due to larger DSs, the ICI becomes a major factor of performance loss at high SNRs. As a result, the static channel assumption made in the previous sections dose not hold in such a case.

For comparison, another simulation with a sample rate of 10 MHz is performed. The simulation results are shown in the Fig. 3.9, which indicates that with a higher sample rate, the channel can be viewed as static over on OFDM symbol even with larger DSs, such as 1000 Hz. Hence, estimation performance loss may occur in systems with longer symbol

durations. We can also deduce that, the channel estimator using training over multiple OFDM symbols performs worse than that of using training over a single OFDM symbol, especially under fast-fading channels.

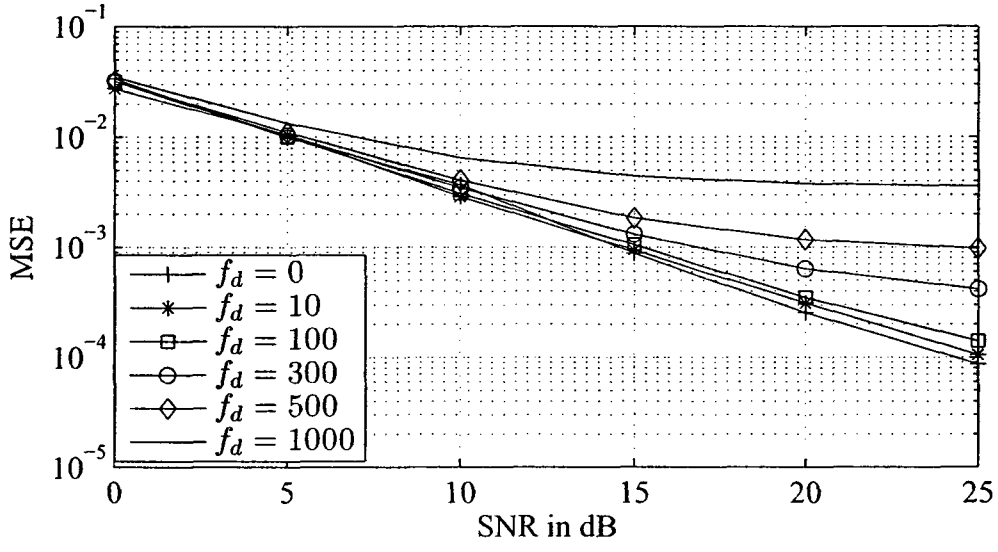

Figure 3.8: MSE versus SNR with different DSs, $T = 1\ \mu s$

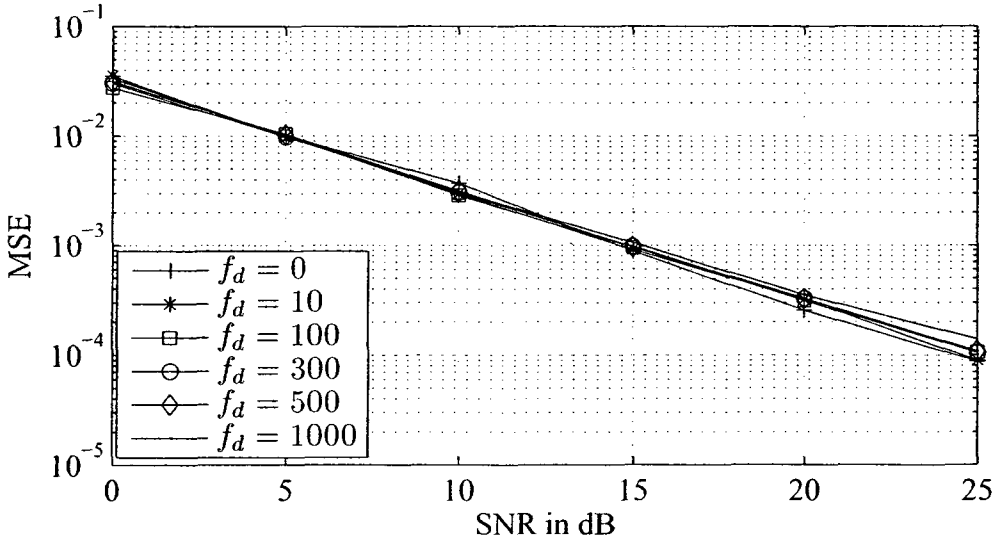

Figure 3.9: MSE versus SNR with different DSs, $T = 0.1\ \mu s$

3.3.5 Experiment 5: Estimation of Rician Channels

This final experiment investigates the performance of the TSLS channel estimator for Rician fading channels with different K-factors. All system parameters are kept the same as previous experiments, except for a non-zero K-factor which denotes a Rician fading channel as opposed to Rayleigh fading where $K = 0$. Note in this experiment, only the first channel tap is Rician process [21], while other 7 taps are Rayleigrician-amplitude.figh distributed. Thus, we only examine the estimation performance of the first tap.

Firstly, we test on a system with an AOA being $\theta_0 = 90°$ and give the MSE results in Fig. 3.10, where K varies from 0 to 10, and $K = 0$ indicates Rayleigh fading. It is seen that when $\theta_0 = 90°$, the channel is nearly quasi-static during the period of on OFDM symbol. To explain this phenomenon, we recall Eq. (2.9) for CIR of fading channels:

$$h(t) = \frac{1}{\sqrt{K+1}} \sum_{i=1}^{I} \alpha_i e^{j[2\pi f_d \cos(\theta_i)t + \phi_i]} + \sqrt{\frac{K}{K+1}} e^{j[2\pi f_d \cos(\theta_0)t + \phi_0]} \tag{3.13}$$

where the initial phase ϕ_0 is normally set to 0. Hence, when $\theta_0 = \pi/2$, Eq. (3.13) becomes

$$h(t) = \frac{1}{\sqrt{K+1}} \sum_{i=1}^{I} \alpha_i e^{j[2\pi f_d \cos(\theta_i)t + \phi_i]} + \sqrt{\frac{K}{K+1}} \tag{3.14}$$

which means that the CIR is a sum of the Rayleigh fading CIR plus a constant term. As shown in the left half of Fig. 3.12, with the increase of K-factor, the amplitude of CIR begins to increase and gets closer to 0 dB; on the other hand, the fading speed keeps almost unchanged in terms of the K-factor, and therefore explains the situation in Fig. 3.10.

The second experiment is carried out with $\theta_0 = 0$, or $f_{d,LOS} = 100$ Hz. Apparently, this channel fades faster than the former one, and a larger K can lead to visible performance loss as shown in Fig. 3.11. This is because the second term on the right side of (3.13) becomes

a complex periodic function with a frequency of 100 Hz.

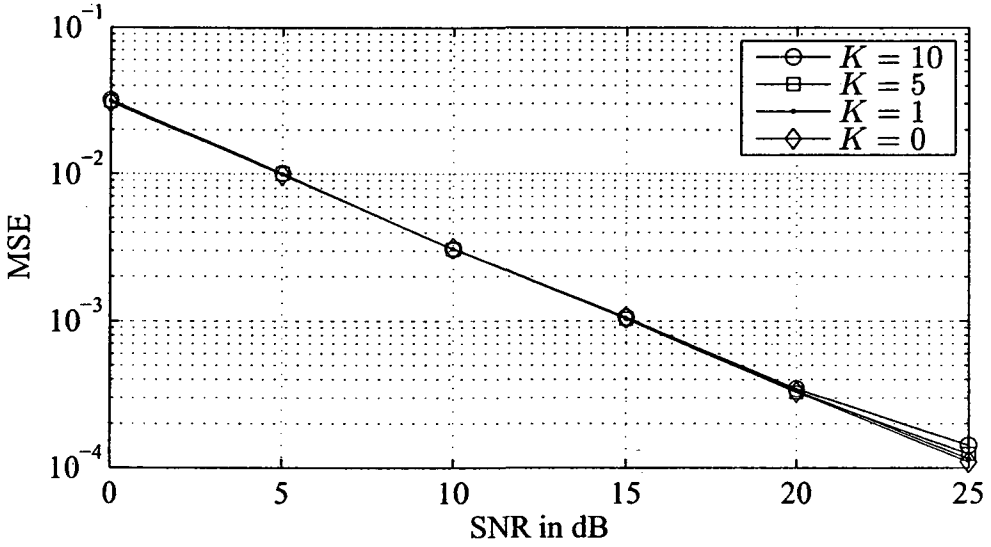

Figure 3.10: MSE versus SNR in Rician fading channels, $\theta_0 = 90°$

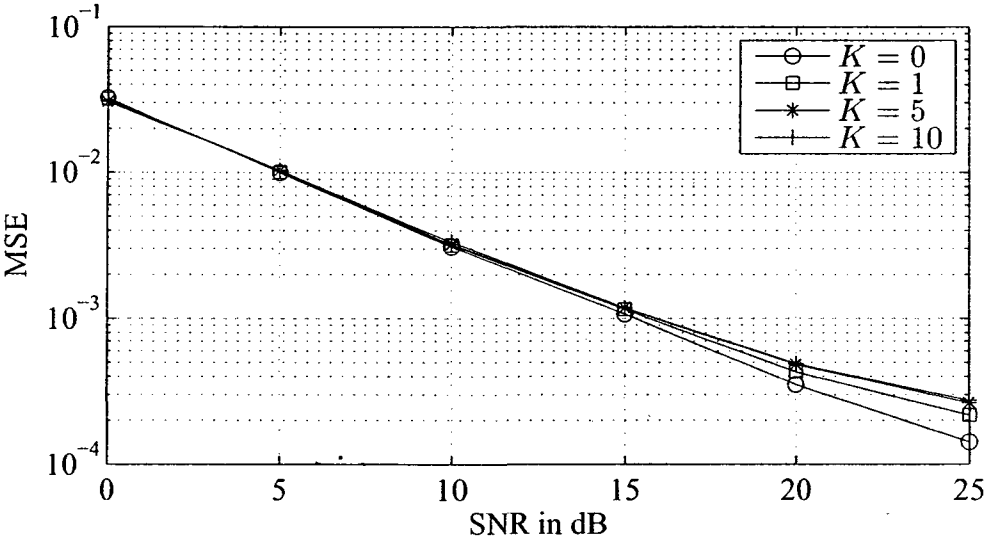

Figure 3.11: MSE versus SNR in Rician fading channels, $\theta_0 = 0$

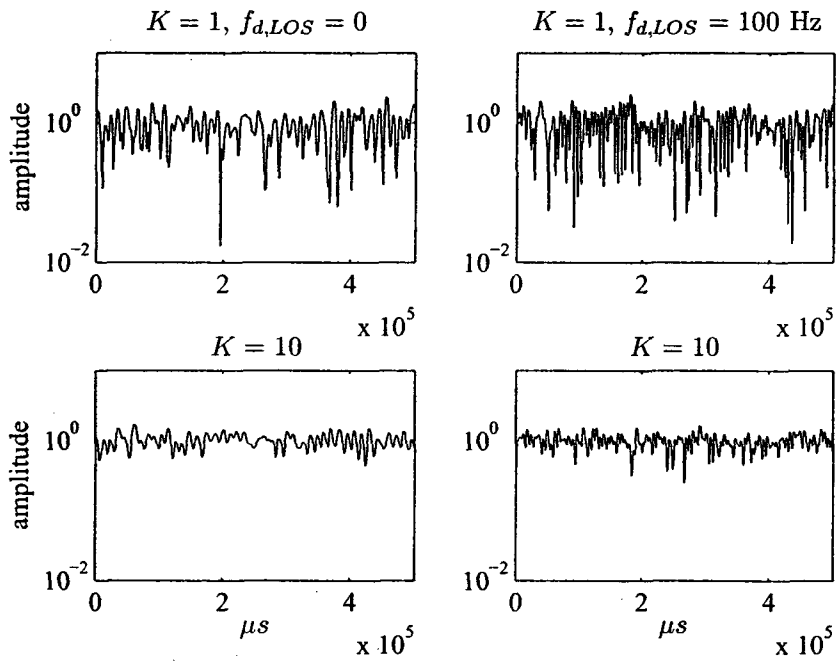

Figure 3.12: Rician fading

3.4 Conclusion

In this chapter, we have conducted a thorough study of the TSLS MIMO-OFDM channel estimation approach in the time domain. Optimal training-sequences were derived according to the minimal MSE criterion, and implemented into consecutive OFDM symbols. Computer simulations were carried out by using one training symbol with different system parameters and channel conditions. The simulation results indicated that, for a MIMO-OFDM system, where the guard interval of each OFDM symbol is no less than the channel length and a minimum of $L \times N_t$ optimal pilots are equispacedly inserted within one OFDM symbol, the TSLS channel estimator provides very satisfactory channel estimates under moderate channel conditions, which are well suitable for DS estimation. We have also pointed out that the TSLS estimation is easy to implement in practical application.

Chapter 4

ACF based DS Estimation for MIMO-OFDM Systems

In this chapter, we present a DS estimation method for MIMO-OFDM systems. It is based on the ACF of the CIR, which is obtained by using the TSLS channel estimation method in Chapter 3. Firstly, we give a brief overview of auto-correlation property of the fading channels as well as two algorithms for the calculation of the DS under Rayleigh fading channels. The two algorithms will be then extended for i.i.d. MIMO channels in the later sections. The first one utilizes the first zero-crossing point of the ACF curve, and the second one calculates the inverse of Bessel function by employing the partial ACF curve, which is divided into polynomial fitting and look-up tables schemes. The ACF based DS estimator is also extended for Rician fading channels with another DS estimator proposed for LOS path. Accuracy analyses for different algorithms are investigated thereafter. Interpolation techniques are then proposed to improve the estimation performance under certain circumstances. Finally, we give a detailed computer simulation study of the DS estimation

for MIMO-OFDM systems with different system parameters and channel conditions, along with comparisons between the proposed algorithms.

4.1 ACF based DS Estimation for SISO Systems

4.1.1 Auto-correlation Feature of Rayleigh Fading Channels

As reviewed in Chapter 2, the CIR can be expressed by

$$h(t) = \Re(t) + j\Im(t) \tag{4.1}$$

For a Rayleigh fading channel, $\Re(t)$ and $\Im(t)$ are independent Gaussian random variables with zero-mean and unit variance. That is, $\mathrm{E}\{\Re(t)\} = \mathrm{E}\{\Im(t)\} = 0$, $\sigma^2_{\Re(t)} = \sigma^2_{\Im(t)} = 1$. In this case, the normalized ACF of random variable $\Re$ or $\Im$ has the following closed form:

$$R_{\Re\Re}(\tau) = R_{\Im\Im}(\tau) = \mathrm{E}\left\{\Re(t)\Re(t+\tau)\right\} = \mathrm{E}\left\{\Im(t)\Im(t+\tau)\right\} = J_0(2\pi f_d \tau) \tag{4.2}$$

where $\mathrm{E}\{\cdot\}$ represents expectation and $J_0(\cdot)$ is the zeroth-order Bessel function of the first kind; f_d is the maximum DS and τ denotes the time delay of the delay path.

We should notice that, τ can only be discrete values in practical processing, i.e. $\tau = kT_s$, where k is the index of OFDM symbols, and T_s represents the time duration of an OFDM symbol. Thus, (4.2) can be rewritten as

$$R_{\Re\Re}(k) = \mathrm{E}\left\{\Re(m)\Re(m+k)\right\} = J_0(2\pi f_d k T_s) \tag{4.3}$$

where m denotes the mth OFDM symbol. The maximum DS f_d can now be calculated by the inverse of Bessel function

$$f_d = \frac{J_0^{-1}\left(\mathrm{E}\left\{\Re(m)\Re(m+k)\right\}\right)}{2\pi k T_s} = \frac{J_0^{-1}(R_{\Re\Re}(k))}{2\pi k T_s} \tag{4.4}$$

Note that the ACF is generated by the CIRs, which are already estimated in Chapter 3 by using optimal training pilots along with the LS algorithm. Let the CIRs be denoted by $\hat{h}(m) = \hat{\Re}(m) + j\hat{\Im}(m)$, the normalized ACF can be calculated as

$$J_0(2\pi f_d k T_s) = \mathrm{E}\left\{\hat{\Re}(m)\hat{\Re}(m+k)\right\} = \hat{R}_{\Re\Re}(k) \tag{4.5}$$

where $\hat{\Re}(m)$ and $\hat{R}_{\Re\Re}(k)$ denote, respectively, the real component of the CIR estimates and the generated ACF with lag k.

Now the question becomes how to get the inverse of generated ACF. In the succeeding sections, several ACF based algorithms are proposed.

4.1.2 DS Estimation Employing Zero-crossing Point of ACF

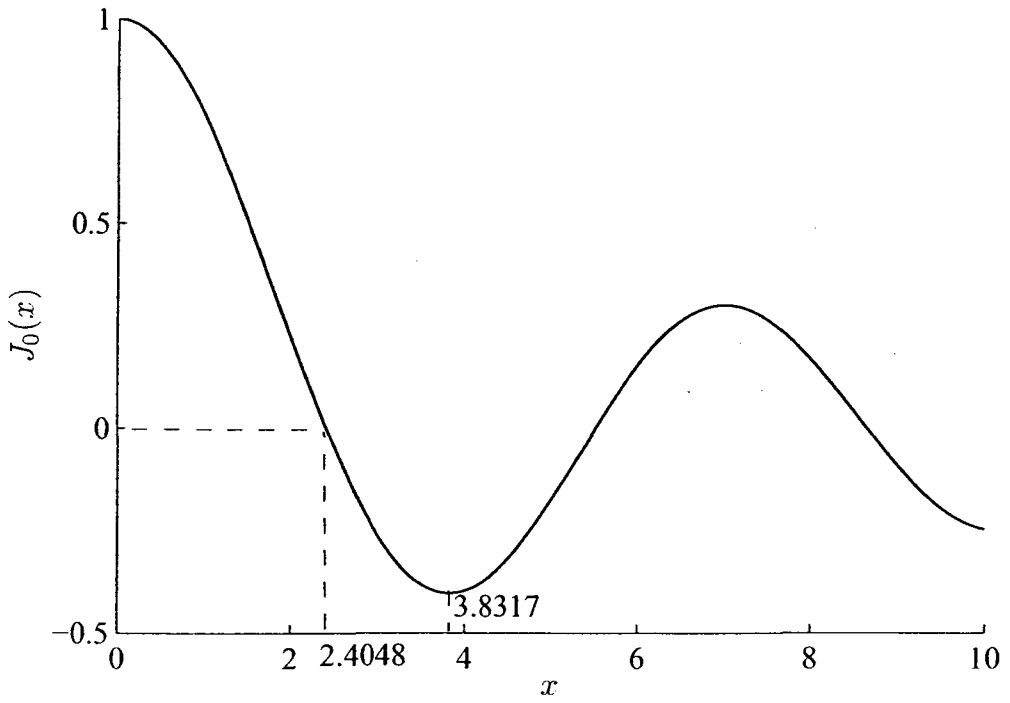

Figure 4.1: Zeroth-order Bessel function of the first kind

Theoretically, the generated ACF which employs channel estimates is equal to a zeroth-order Bessel function of the first kind [22] as shown in Fig. 4.1. We can see that the Bessel function is monotonically decreasing between 0 and the first zero-crossing point $k_0 = 2.4048$. From (4.4) and (4.5), the estimated maximum DS $\hat{f}_d$ can be calculated by [22]

$$\hat{f}_d = \frac{J_0^{-1}(0)}{2\pi \hat{k}_0 T_s} = \frac{2.4048}{2\pi \hat{k}_0 T_s} \tag{4.6}$$

where $\hat{k}_0$ represents the estimated first zero-crossing point of the normalized ACF. Assuming that adequate CIRs are available for ACF computation. Hence it should be accurate enough to estimate the first zero-crossing point $\hat{k}_0$ simply by utilizing linear interpolation for the generated ACF curve.

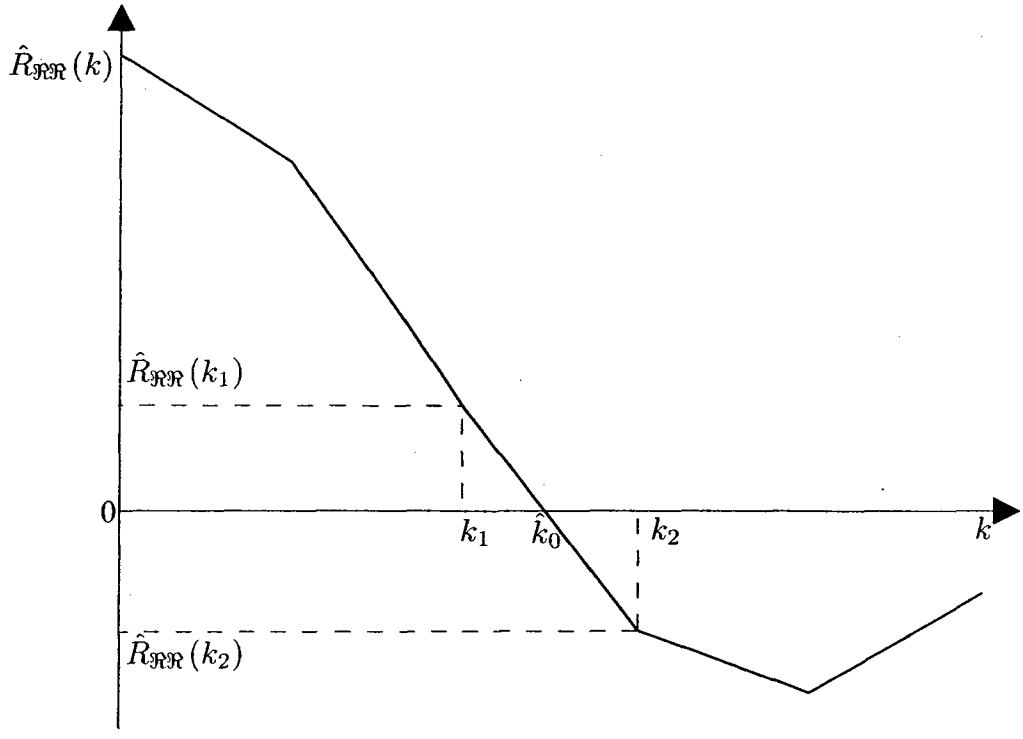

Figure 4.2: Linear interpolation of ACF curve for estimating the first zero-crossing point

Fig. 4.2 shows that an ACF curve has a first zero-crossing point $\hat{k}_0$, which could be determined by using linear interpolation between $\hat{R}_{\Re\Re}(k_1)$ and $\hat{R}_{\Re\Re}(k_2)$, where $k_2 = k_1 + 1$. Therefore, the estimated first zero-crossing point $\hat{k}_0$ can be obtained by solving the equations below:

$$\begin{cases} \frac{\hat{R}_{\Re\Re}(k_1)-\hat{R}_{\Re\Re}(k_2)}{k_1-k_2} = \frac{\hat{R}_{\Re\Re}(k_1)-\hat{R}_{\Re\Re}(\hat{k}_0)}{k_1-\hat{k}_0} \\ \hat{R}_{\Re\Re}(\hat{k}_0) = 0 \\ k_2 = k_1 + 1 \end{cases} \tag{4.7}$$

Namely,

$$\hat{k}_0 = k_1 - \frac{\hat{R}_{\Re\Re}(k_1)}{\hat{R}_{\Re\Re}(k_2) - \hat{R}_{\Re\Re}(k_1)} \tag{4.8}$$

provided that $\hat{R}_{\Re\Re}(k_1) \geq 0$ and $\hat{R}_{\Re\Re}(k_2) \leq 0$.

The zero-crossing algorithm is summarized in Fig. 4.3

4.1.3 DS Estimation Employing ACF Curve

The zero-crossing scheme for DS estimation is efficient and simple. However, since it utilizes linear interpolation, it does not give a high accuracy. Moreover, the first zero-crossing point may not be obtained accurately due to insufficient channel estimates for ACF computation, or poor channel conditions such as low SNR. To overcome such drawbacks, we can exploit the generated ACF curve for a better estimation result. Two schemes making use of the ACF curve are proposed as follows.

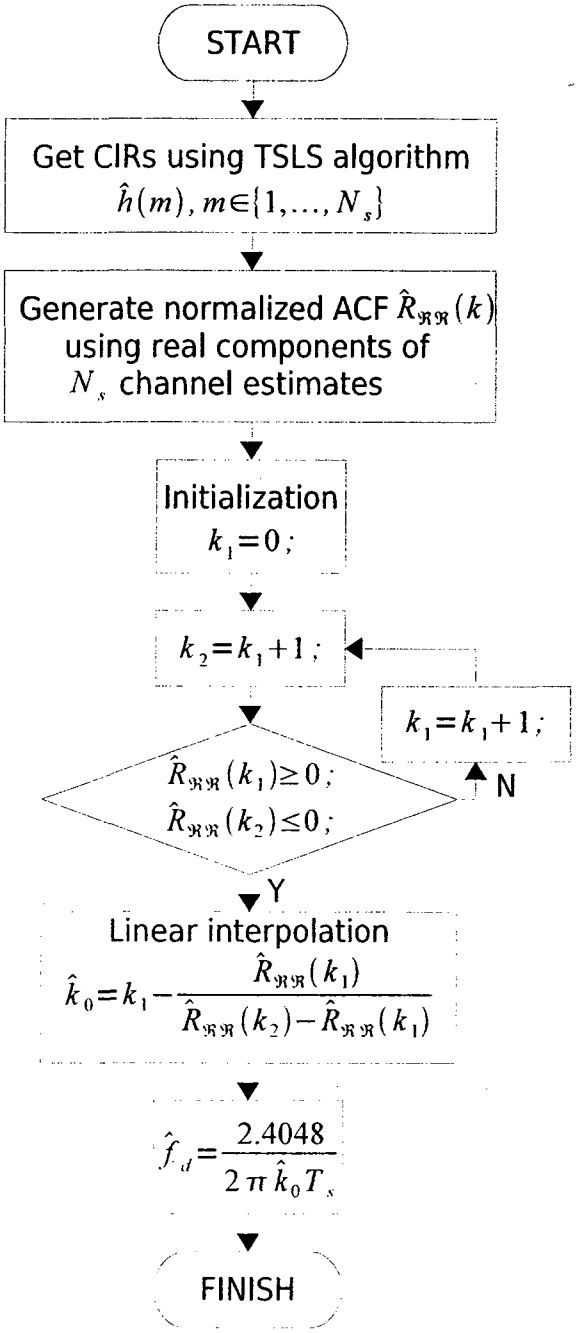

Figure 4.3: Flowchart of zero-crossing algorithm

Polynomial Curve Fitting Scheme

It is known that the zeroth-order Bessel function of the first kind can be expanded using Taylor series as

$$J_0(x) = \sum_{n=0}^{\infty} \frac{(-1)^n x^{2n}}{2^{2n}(n!)^2}$$

As $J_0(x)$ is monotonically decreasing in the span of $[0,\ 3.8317)$ (see Fig. 4.1), we choose $[0, 2]$ as our observation interval, or $J_0(x) \in [1, 0.2239]$, equivalently. Then, $J_0(x)$ can be approximated by a 6-order polynomial [23]:

$$J_0(x) = 1 - \frac{x^2}{4} + \frac{x^4}{64} - \frac{x^6}{2304} + O\Big(\frac{1}{576}\Big),\ x \in [0, 2] \tag{4.9}$$

Due to $J_0(2\pi f_d k T_s) = \hat{R}_{\Re\Re}(k) = \mathrm{E}\left\{\hat{\Re}(m)\hat{\Re}(m+k)\right\}$, (4.9) can be rewritten as

$$1 - \frac{x^2}{4} + \frac{x^4}{64} - \frac{x^6}{2304} = \hat{R}_{\Re\Re}(k) = \hat{R}_{\Re\Re}\Big(\frac{x}{2\pi f_d T_s}\Big)$$

i.e.

$$2304\big[\hat{R}_{\Re\Re}(k) - 1\big] + 576x^2 - 36x^4 + x^6 = 0 \tag{4.10}$$

In addition, the companion matrix of the monic polynomial $p(x) = c_0 + c_1 x + \cdots + c_{n-1}x^{n-1} + x^n$ is a square matrix as given by

$$C(p) = \begin{bmatrix} 0 & 0 & \dots & 0 & -c_0 \\ 1 & 0 & \dots & 0 & -c_1 \\ 0 & 1 & \dots & 0 & -c_2 \\ \vdots & \vdots & \ddots & \vdots & \vdots \\ 0 & 0 & \dots & 1 & -c_{n-1} \end{bmatrix}_n,\ n \geq 2$$

which can be rewritten with the given coefficients of (4.10) as

$$C(p) = \begin{bmatrix} 0 & 0 & 0 & 0 & 0 & 2304[1 - \hat{R}_{\Re\Re}(k)] \\ 1 & 0 & 0 & 0 & 0 & 0 \\ 0 & 1 & 0 & 0 & 0 & -576 \\ 0 & 0 & 1 & 0 & 0 & 0 \\ 0 & 0 & 0 & 1 & 0 & 36 \\ 0 & 0 & 0 & 0 & 1 & 0 \end{bmatrix} \tag{4.11}$$

The eigenvalues of the companion matrix $C(p)$ equal the roots of $p(x) = 0$. Therefore, the roots of (4.10) can be resolved by calculating the eigenvalues of the companion matrix (4.11).

Finally, the maximum DS can be estimated by

$$\hat{f}_d = \frac{x}{2\pi k T_s} \tag{4.12}$$

where x is the only real and positive root of the 6-order polynomial (4.10) in the range of $[0, 2]$. A flowchart summarizing the proposed DS estimator is shown in Fig. 4.4.

Look-up Table Scheme

Despite the fact that the proposed polynomial curve fitting method using high-order polynomials could be more accurate than searching for a single zero-crossing point by linear interpolation, a higher order polynomial results in higher accuracy as well as slower calculation of the eigenvalues of the corresponding companion matrix. In order to reduce computational complexity, a look-up table 4.1 of Bessel function within $[0, 2]$ is required. Therefore, it becomes simply searching in this table for a certain value of $J_0(x)$, which is

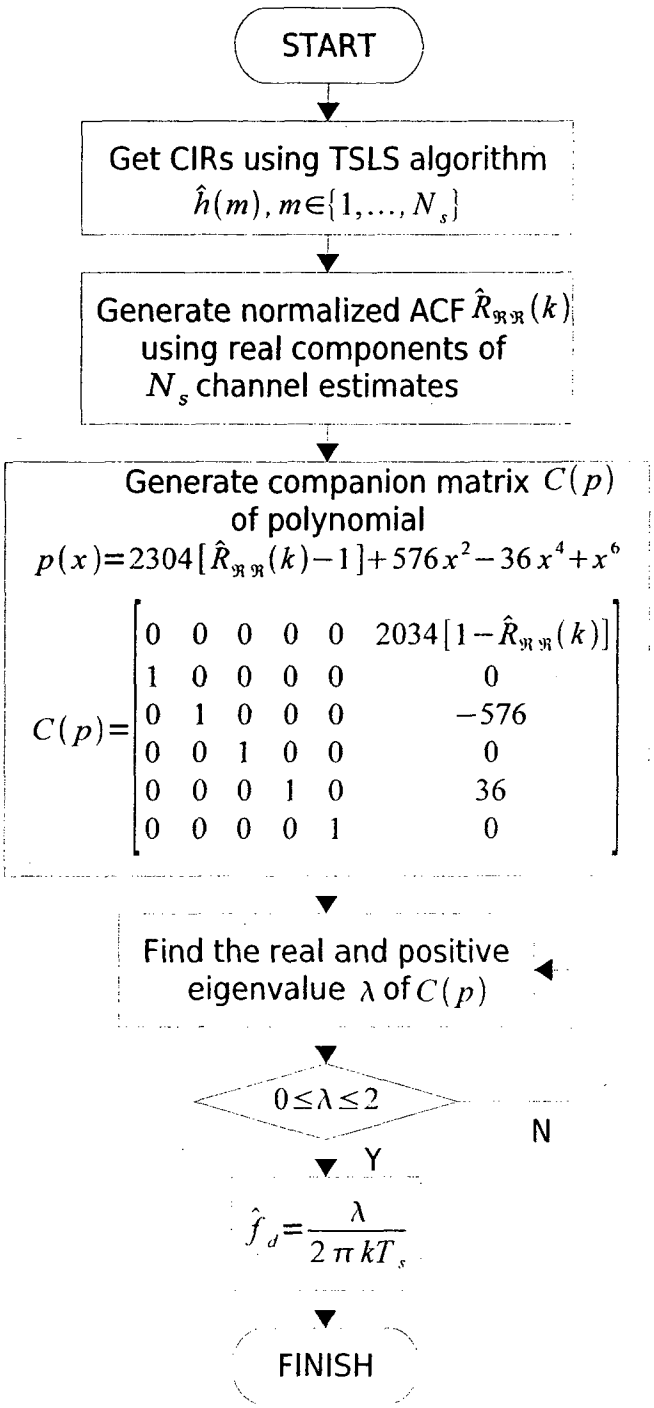

Figure 4.4: Flowchart of polynomial curve fitting algorithm

the closet to the estimated normalized ACF $\hat{R}_{\Re\Re}(k)$:

$$\hat{x} = \arg \min_{x \in [0,2]} |J_0(x) - \hat{R}_{\Re\Re}(k)| \tag{4.13}$$

$\hat{x}$ is then utilized to calculate the maximum DS by the following equation similar to (4.12):

$$\hat{f}_d = \frac{\hat{x}}{2\pi k T_s} \tag{4.14}$$

For example, if the estimated ACF $\hat{R}_{\Re\Re}(k) = 0.765$, the closet value of $J_0(x)$ found in the look-up table is $J_0(1.0) = 0.7652$. Thus, an estimate of f_d is obtained using (4.14) with $\hat{x} = 1.0$. Fig. 4.5 is a flowchart of the proposed algorithm:

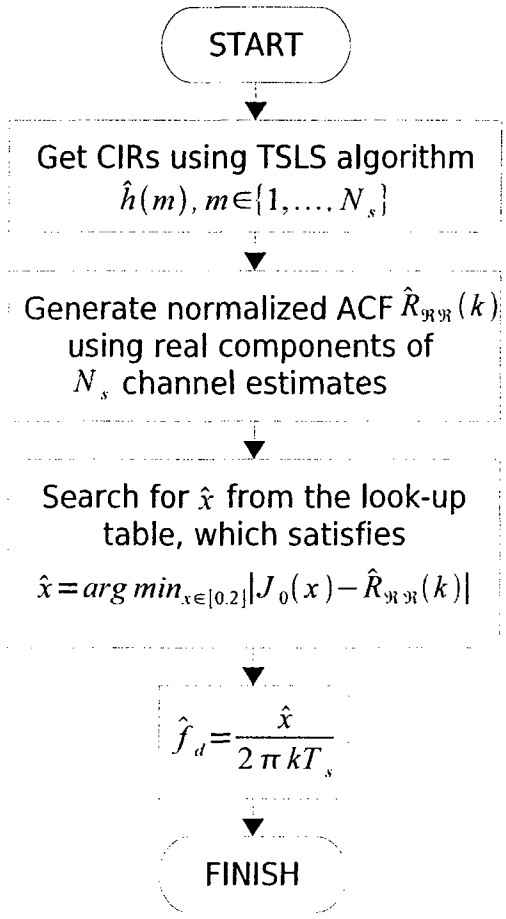

Figure 4.5: Flowchart of look-up table scheme

Table 4.1: Look-up table of $J_0(x)$ with x ranging from 0 to 2.09

x	0.00	0.01	0.02	0.03	0.04	0.05	0.06	0.07	0.08	0.09
0.0	1.0000	1.0000	0.9999	9998	9996	9994	9991	9988	9984	9980
0.1	0.9975	9970	9964	9958	9951	9944	9936	9928	9919	9910
0.2	9900	9890	9879	9868	9857	9844	9832	9819	9805	9791
0.3	9776	9761	9746	9730	9713	9696	9679	9661	9642	9623
0.4	9604	9584	9564	9543	9522	9500	9478	9455	9432	9409
0.5	9385	9360	9335	9310	9284	9258	9231	9204	9177	9149
0.6	9120	9091	9062	9032	9002	8971	8940	8909	8877	8845
0.7	8812	8779	8745	8711	8677	8642	8607	8572	8536	8500
0.8	8463	8426	8388	8350	8312	8274	8235	8195	8156	8116
0.9	8075	8034	7993	7952	7910	7868	7825	7783	7739	7696
1.0	7652	7608	7563	7519	7473	7428	7382	7336	7290	7243
1.1	7196	7149	7101	7054	7006	6957	6909	6860	6810	6761
1.2	6711	6661	6611	6561	6510	6459	6408	6356	6305	6253
1.3	6201	6149	6096	6043	5990	5937	5884	5830	5777	5723
1.4	5669	5614	5560	5505	5450	5395	5340	5285	5230	5174
1.5	5118	5062	5006	4950	4894	4838	4781	4725	4668	4611
1.6	4554	4497	4440	4383	4325	4268	4210	4153	4095	4038
1.7	3980	3922	3864	3806	3748	3690	3632	3574	3516	3458
1.8	3400	3342	3284	3225	3167	3109	3051	2993	2934	2876
1.9	2818	2760	2702	2644	2586	2528	2470	2412	2354	2297
2.0	2239	2181	2124	2066	2009	1951	1894	1837	1780	1723

4.1.4 DS Estimation for Rician Fading Channels

In the preceding sections, a Rayleigh fading channel model is assumed. Nevertheless, the proposed schemes cannot be directly applied to Rician fading channels since the generated ACF is no longer a Bessel function. As shown in Fig. 2.8 where $K = 10$, $f_d = 100$ Hz and $\theta_0 = 0$, 1000 CIR estimates are utilized to generate the normalized ACF curve. For a specific f_d, both channels have different ACF curves. As a result, a large MSE would occur if the previous estimation schemes proposed for Rayleigh fading channels are employed for Rician channels.

Recall that the ACF of Rician fading channel (2.21) with a substitution of $\tau = kT_s$ is given by

$$R_{\Re\Re}(k) = \frac{1}{K+1} J_0(2\pi f_d k T_s) + \frac{K}{K+1} \cos\left(2\pi f_d \cos(\theta_0) k T_s\right) \tag{4.15}$$

where K is the ratio of the power of the LOS component to the scattered component, θ_0 is the AOA of the LOS component. Here, we separate the ACF into two cases with regard to θ_0. While θ_0 is equal to 90° (see Fig. 4.6), (4.15) becomes

$$R_{\Re\Re}(k) = \frac{1}{K+1} J_0(2\pi f_d k T_s) + \frac{K}{K+1} \tag{4.16}$$

Thus the second term of (4.16) can be viewed as a Direct Current (DC) component, which can be further removed by eliminating the mean value of the estimated CIRs [11]. When $\theta_0 \neq 90°$, we have an interesting result,

$$\begin{aligned} \lim_{K\to\infty} R_{\Re\Re}(k) &= \lim_{K\to\infty} \left\{ \frac{1}{K+1} J_0(2\pi f_d k T_s) + \frac{K}{K+1} \cos\left(2\pi f_d k T_s \cos\theta_0\right) \right\} \\ &= \cos\left(2\pi f_d k T_s \cos\theta_0\right) \end{aligned} \tag{4.17}$$

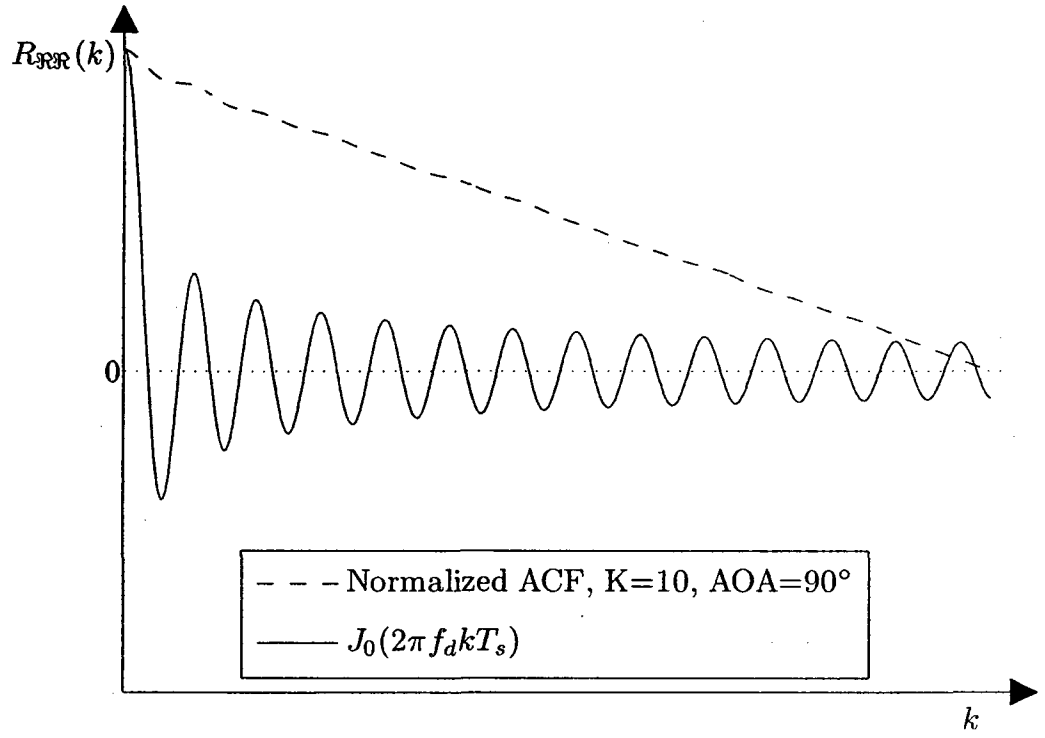

Figure 4.6: Normalized ACF when $\theta_0 = 90°$

which implies that the ACF can be approximated by a cosine function with a relative large value of K.

Fig. 4.7 shows an ACF curve of Rician fading channels with $K = 10$ in reference to a cosine function, that is generated based on 1000 CIRs, where k_v represents the first valley point and also the half-period (π) of the ACF curve. It indicates that with a relative large K-factor, the ACF curve is periodical with the same period as the reference cosine function. On the other hand, the envelope of ACF curve drops gradually. The more the channel estimates used for ACF computation, the slower the envelop of ACF declines. Fortunately, the first half-period of the generated ACF can always be reliably utilized to calculate $f_d \cos\theta_0$, which is actually the DS of the direct path, or LOS path. According to Eq. (4.17), the direct path

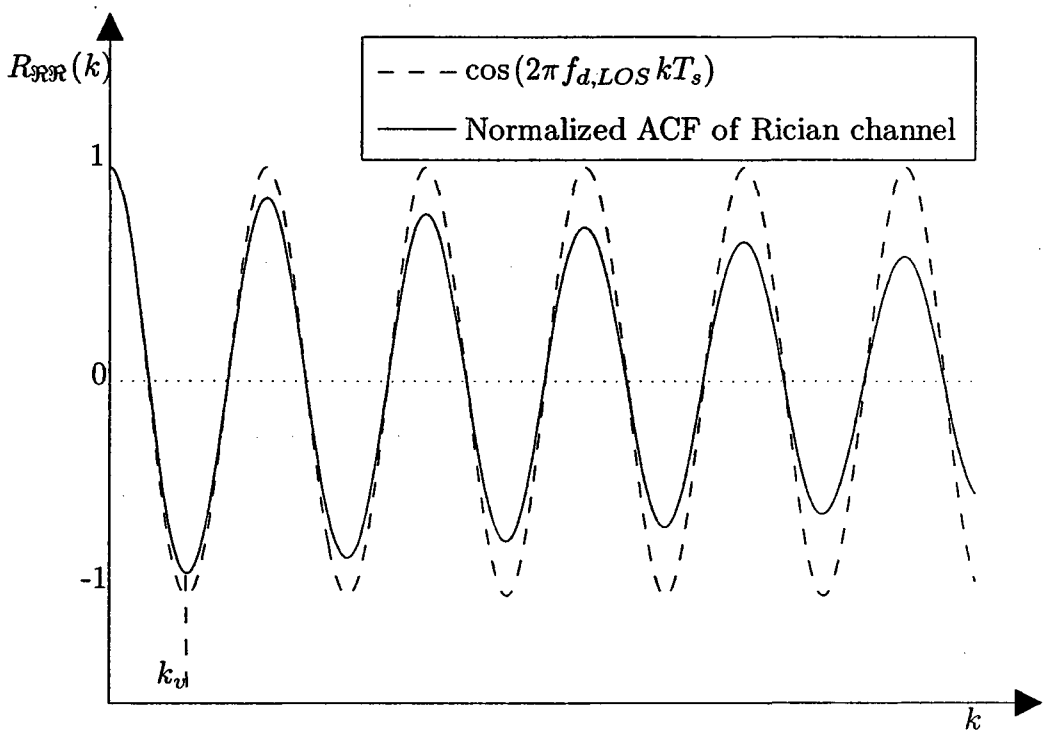

Figure 4.7: Normalized ACF curve of Rician fading channel

DS can be determined by

$$2\pi f_d k_v T_s \cos\theta_0 = \pi$$

or,

$$\hat{f}_{d,LOS} = f_d \cos\theta_0 = \frac{\pi}{2\pi k_v T_s} = \frac{1}{2k_v T_s} \tag{4.18}$$

where k_v denotes the first valley point of the estimated ACF curve.

Moreover, if θ_0 is known a prior to the receiver, the maximum DS can be simply obtained by

$$\hat{f}_d = \frac{1}{2k_v T_s \cos\theta_0} \tag{4.19}$$

A flowchart (Fig. 4.8) is drawn below to summarize the proposed algorithm for Rician fading channels.

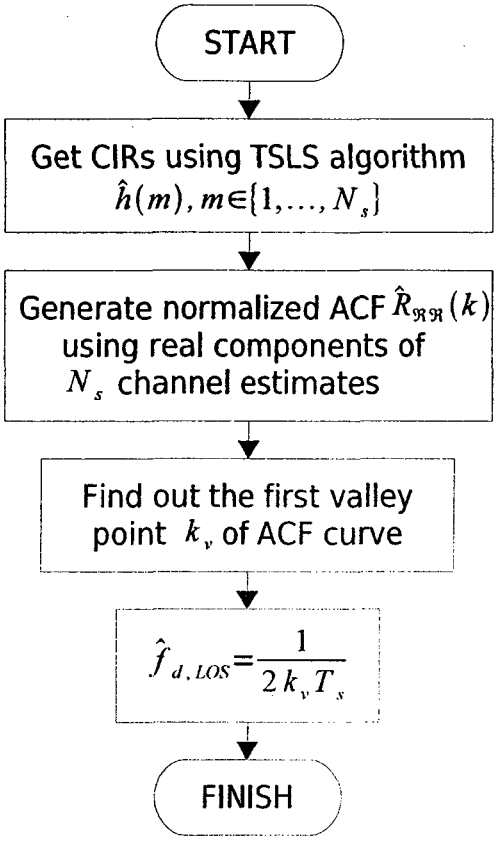

Figure 4.8: Flowchart of LOS DS estimator

4.2 ACF Based DS Estimation for i.i.d. MIMO-OFDM Systems

In this section, we propose several ACF based DS estimation approaches for i.i.d. MIMO-OFDM systems.

4.2.1 Rayleigh Fading Channels

First of all, we recall the MIMO channel model described in Chapter 2

$$\mathbf{y}_n(m) = \sum_{l=0}^{L-1} \mathbf{H}_l(m)\mathbf{x}_{n-l}(m) + \mathbf{v}_n(m) \tag{4.20}$$

where the lth tap channel matrix for the mth OFDM symbol is given by

$$\mathbf{H}_l(m) = \begin{bmatrix} h_l^{1,1}(m) & h_l^{1,2}(m) & \dots & h_l^{1,N_t}(m) \\ h_l^{2,1}(m) & h_l^{2,2}(m) & \dots & h_l^{2,N_t}(m) \\ \vdots & \vdots & \ddots & \vdots \\ h_l^{N_r,1}(m) & h_l^{N_r,2}(m) & \dots & h_l^{N_r,N_t}(m) \end{bmatrix}_{N_r \times N_t} \tag{4.21}$$

Here, the element $h_l^{n_r n_t}(m)$ represents the CIR between the n_rth receive antenna and the n_tth transmit antenna. For the i.i.d. MIMO channel, elements $h_l^{n_r,n_t}(m)$ ($n_r \in \{0,\dots,N_r\}$, $n_t \in \{0,\dots,N_t\}$) are independent complex random variables. If there is no LOS propagation, i.e. the Rayleigh fading case, they are also known as circular symmetric Gaussian random variables. Therefore, for each pair of transmit and receive antennas, we have an ACF of $R_{h_l h_l}^{n_r,n_t}(k) = \mathrm{E}\left\{h_l^{n_r,n_t}(m)(h_l^{n_r,n_t}(m+k))^*\right\} = J_0(2\pi f_d k T_s)$, where T_s denotes OFDM symbol duration and k represents the index of OFDM symbols.

Define

$$\mathbf{h}(m) = \left[\mathbf{h}_0^T(m), \ldots, \mathbf{h}_{L-1}^T(m)\right]^T \tag{4.22}$$

as the mth discrete-time CIR vector, where $\mathbf{h}_l(m) = \text{vec}\left(\mathbf{H}_l(m)\right)$, and the operation $\text{vec}\left(\mathbf{H}_l(m)\right)$ represents the vector associated with the lth channel tap $\mathbf{H}_l$, i.e.

$$\mathbf{h}_l(m) = \left[(\mathbf{h}_l^1(m))^T, \ldots, (\mathbf{h}_l^{N_t}(m))^T\right]^T \tag{4.23}$$

where

$$\mathbf{h}_l^{n_t}(m) = \left[h_l^{1,n_t}(m), \ldots, h_l^{N_r,n_t}(m)\right]^T \tag{4.24}$$

Thus, the correlation matrix of vector $\mathbf{h}$ can be expressed as

$$\begin{aligned}
\mathbf{R}_{hh}(k) &= \mathrm{E}\left\{\mathbf{h}(m)\mathbf{h}^H(m+k)\right\} \\
&= \text{diag}\left\{\mathbf{R}_{h_0h_0}(k), \ldots, \mathbf{R}_{h_{L-1}h_{L-1}}(k)\right\} \\
&= J_0(2\pi f_d k T_s)\mathbf{I}_{LN_tN_r}
\end{aligned} \tag{4.25}$$

where $\mathbf{I}_{LN_tN_r}$ is an identity matrix of size $LN_tN_r \times LN_tN_r$, and

$$\mathbf{R}_{h_lh_l}(k) = \left[\mathbf{R}_{h_lh_l}^1(k), \ldots, \mathbf{R}_{h_lh_l}^{N_t}(k)\right] \tag{4.26}$$

with

$$\mathbf{R}_{h_lh_l}^{n_t}(k) = \left[R_{h_lh_l}^{1,n_t}(k), \ldots, R_{h_lh_l}^{N_r,n_t}(k)\right] \tag{4.27}$$

For the real components of CIRs, we have a similar form as given by

$$\mathbf{R}_{\Re\Re}(k) = J_0(2\pi f_d k T_s)\mathbf{I}_{LN_tN_r} \tag{4.28}$$

Therefore, the estimated DS $\hat{f}_d$ for each $h_l^{n_rn_t}(m)$ can then be obtained by the proposed algorithms as follows:

- **zero-crossing algorithm:**

$$\hat{f}_{d,l}^{n_r,n_t} = \frac{2.4048}{2\pi \hat{k}_0 T_s} \tag{4.29}$$

where $\hat{k}_0$ is the estimated first zero-crossing point of the estimated normalized ACF

$$\hat{R}_{\Re_l\Re_l}^{n_r,n_t}(k) = \mathrm{E}\left\{\Re_l^{n_r,n_t}(m)\Re_l^{n_r,n_t}(m+k)\right\} = J_0(2\pi f_d k T_s) \tag{4.30}$$

which is obtained by linear interpolation

$$\hat{k}_0 = k_1 - \frac{\hat{R}_{\Re\Re}^{n_r,n_t}(k_1)}{\hat{R}_{\Re\Re}^{n_r,n_t}(k_2) - \hat{R}_{\Re\Re}^{n_r,n_t}(k_1)} \tag{4.31}$$

- **polynomial curve fitting algorithm:**

$$\hat{f}_{d,l}^{n_r,n_t} = \frac{x}{2\pi k T_s} \tag{4.32}$$

where x is the real and positive root of the polynomial $2304[\hat{R}_{\Re_l\Re_l}^{n_r n_t}(k) - 1] + 576x^2 - 36x^4 + x^6 = 0$, and $x \in [0, 2]$.

- **look-up table algorithm:**

$$\hat{f}_{d,l}^{n_r,n_t} = \frac{\hat{x}}{2\pi k T_s} \tag{4.33}$$

where $\hat{x}$, determined by (4.13), is the closest value of $\hat{R}_{\Re_l\Re_l}^{n_r,n_t}(k)$ in the look-up table 4.1 of Bessel function $J_0(x)$.

Note that for a MIMO channel with N_r receive antennas, N_t transmit antennas and L FIR taps, the estimated maximum DS can be simply calculated by taking an average of all the DS estimates over all pairs of antennas:

$$\hat{f}_d = \mathrm{E}\left\{\hat{f}_{d,l}^{n_r,n_t}\right\} = \frac{1}{M}\sum_{n_r=1}^{N_r}\sum_{n_t=1}^{N_t}\sum_{l=0}^{L-1}\hat{f}_{d,l}^{n_r,n_t} \tag{4.34}$$

where $M = N_r \times N_t \times L$.

However, due to relatively small number of CIR estimates or severe channel conditions such as low SNR, the maximum DS calculated by (4.34) may lead to performance loss (see Fig. 4.9), such as the absence of zero-crossing point and a shape change of the ACF curve. Therefore, the more efficient way is to reform an averaged ACF over all CIR $h_l^{n_r,n_t}(m)$ in advance, namely,

$$\hat{R}_{\Re\Re}(k) = \mathrm{E}\left\{\hat{R}_{\Re_l\Re_l}^{n_r,n_t}(k)\right\} = \frac{1}{M}\sum_{n_r=1}^{N_r}\sum_{n_t=1}^{N_t}\sum_{l=0}^{L-1}\hat{R}_{\Re_l\Re_l}^{n_r,n_t}(k) \tag{4.35}$$

and then calculate $\hat{f}_d$ by employing the proposed estimators. This way can save processing time greatly and can also have little effect from incorrectly estimated $\hat{f}_{d,l}^{n_r,n_t}$s.

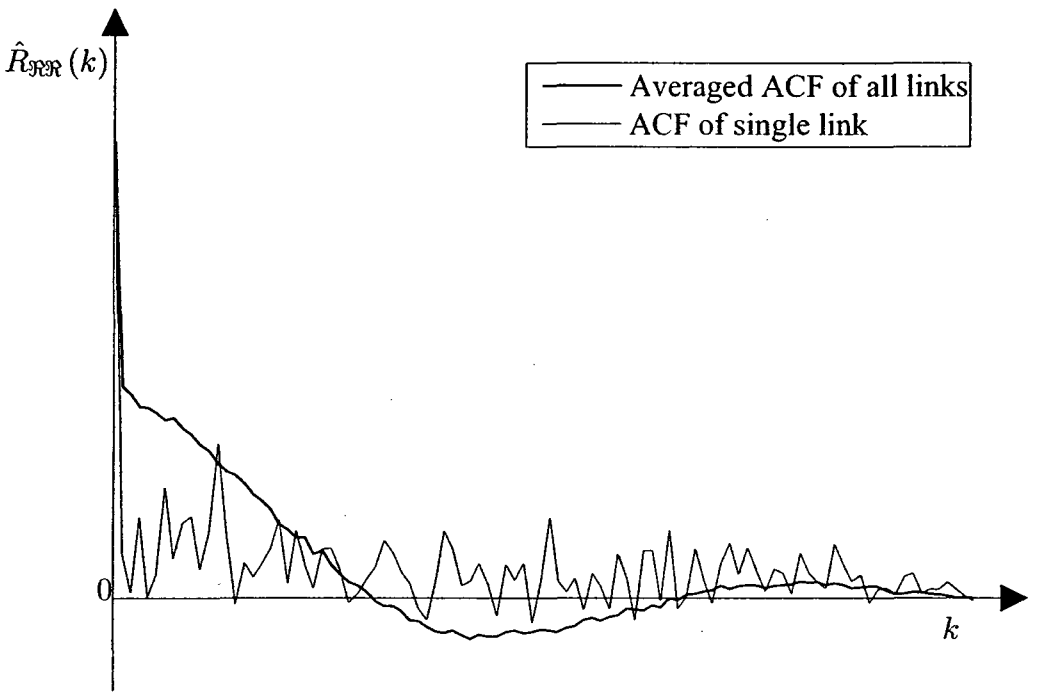

Figure 4.9: Averaged ACF of all links versus the ACF of single link, SNR = 0 dB

4.2.2 Rician Fading Channels

In general, all the multi-path components can be divided into two groups in MIMO channels [21]. Some of the discrete paths present Rician fading processes which contain a LOS component with a non-zero K-factor. The remaining discrete paths are independent Rayleigh fading processes which have no LOS component at all.

In this thesis, we assume that only the first tap of the FIR filter, or non-delay path, is a Rician fading process, and the remaining $N_r \times N_t \times (L-1)$ NLOS paths are Rayleigh fading processes. Under this assumption, we conduct two estimations, one for the maximum DS f_d that can be estimated by normal DS estimators using the $N_r \times N_t \times (L-1)$ NLOS paths; the other for the direct path DS, or $f_{d,LOS}$, that can be done by utilizing Eq. (4.18), along with the first FIR tap, containing $N_r \times N_t$ paths in total. Moreover, the AOA θ_0 can be determined by using Eq. (4.19), i.e.

$$\theta_0 = \arccos\left(\frac{f_{d,LOS}}{f_d}\right) \tag{4.36}$$

4.3 Accuracy Analysis of Proposed Algorithms with Possible Practical Solutions

In this section, we first analyze the accuracy of the proposed four DS estimation algorithms. We will also provide some suggestions for practical implementation of these algorithms.

4.3.1 Zero-crossing Scheme

A decent investigation of the accuracy problem of zero-crossing method has been done in [22]. It was pointed out that the pdf of the zero-crossing point estimated by linear interpolation dose not strictly follow a normal distribution. As a result, a normal arithmetic mean is no longer suitable for such a scheme. At the same time, the pdf of the zero-crossing point varies with the DS, and thus an accurate estimation is relatively difficult to achieve.

Beside the non-normal distribution, the generated ACF curve is hard to stabilize without sufficient channel estimates, and sometimes even no zero-crossing point can be found due to inadequate estimated CIRs. As mentioned in the previous section, to improve the estimation accuracy, all ACFs generated by all pairs of the transmit-receive links shall be averaged to reform an ACF, which on the other hand can largely reduce the entire processing time.

We can make a simple transform from Eq. (4.6)

$$\hat{k}_0 = \frac{2.4048}{2\pi \hat{f}_d T_s} \tag{4.37}$$

which indicates that with a larger f_d, less points are available in the range of $[0, k_0]$. Consequently, the accuracy of estimating the zero-crossing point between two points k_1 and $k_1 + 1$ will degrade. To improve the performance of this estimator, non-linear interpolation techniques can be employed, such as spline method and polynomial fitting. Spline interpolation uses low-degree polynomials in each of the given intervals, and chooses the polynomial parameters such that the ACF is well matched. Fig. 4.10 compares the linear interpolation and spline interpolation in reference to the Bessel function. Apparently, the ACF with spline interpolation almost coincides perfectly with the ideal Bessel function, and

hence can largely improve the estimation accuracy.

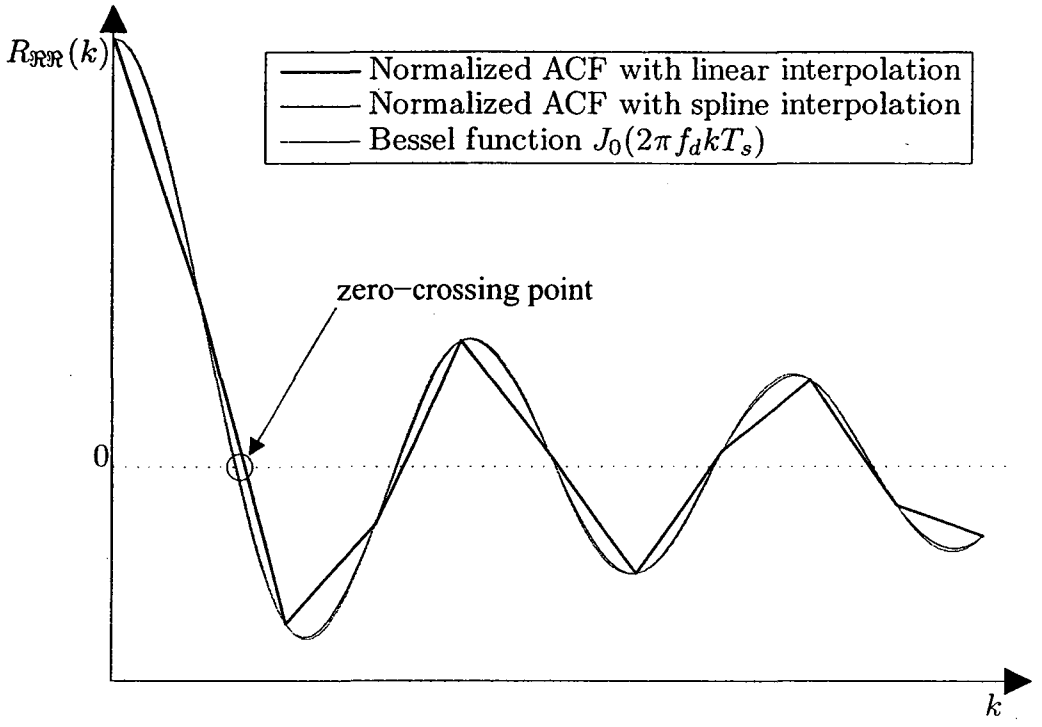

Figure 4.10: Linear interpolation and non-linear interpolation

On the contrary, a small f_d may also lead to a low accuracy. According to (4.37), with a smaller f_d, a larger k_0 occurs, which means in order to obtain the zero-crossing point, a minimum of k_0 CIR estimates are required to generate an ACF curve. Furthermore, it is undetectable when $f_d = 0$, due to $k_0 = \infty$ in this case. Hence, sufficient CIR estimates should be collected prior to DS estimation.

4.3.2 ACF Curve Schemes

Two algorithms have been proposed to make full use of the generated ACF curve. Unlike the zero-crossing scheme, f_d is not estimated by linear interpolation but directly calculating

an inverse of Bessel function. That is to say, the estimation is supposed to be accurate as long as there exists a single point on the observation span of the ACF curve. However, performance degradation is observed in simulations and can be explained in Fig. 4.11.

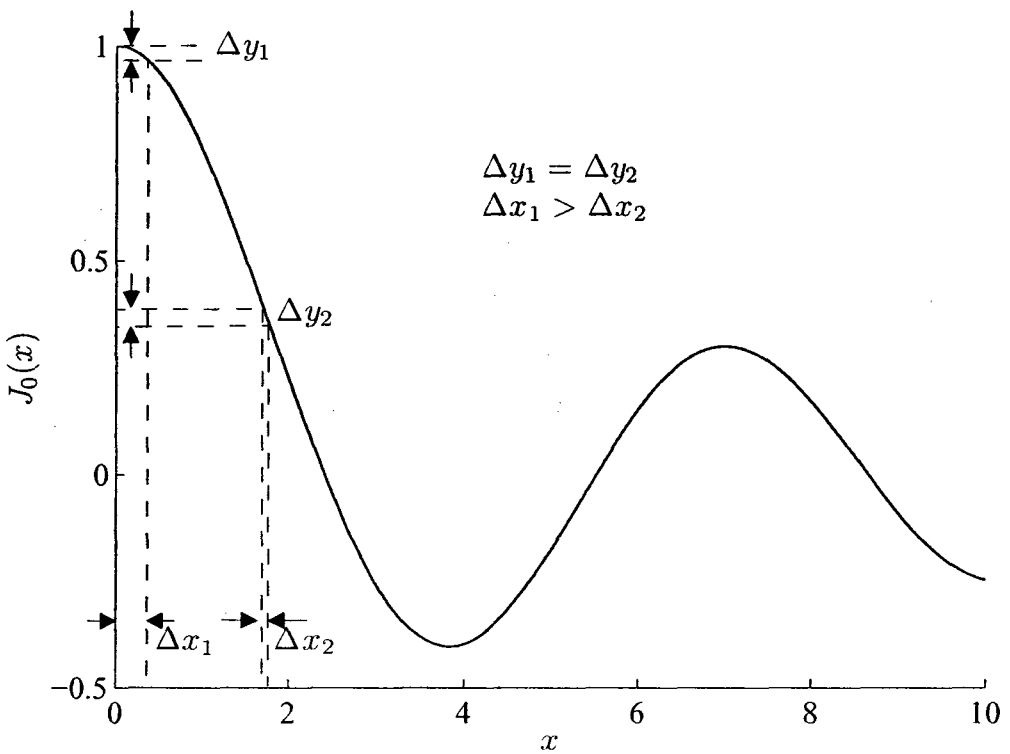

Figure 4.11: Choosing partial ACF curve

From Fig. 4.11, we can see that the closer to 1 the Bessel function moves, the larger offset is observed on the x-axis while with the same offset on the y-axis. Fig. 4.12 shows the slope of the Bessel function $J_0(x)$ in the range of $x = [0, 3]$. Taking Fig. 4.11 and 4.12 into consideration, we can conclude that a large error could be induced by a large slope. Therefore, we need to choose a part of the ACF curve that has the lowest slope, which in particular can be approximately determined by $J_0(1.7) = 0.398$ and $J_0(2) = 0.2239$. Another typical problem for such schemes is point-lacking while the mentioned span is too

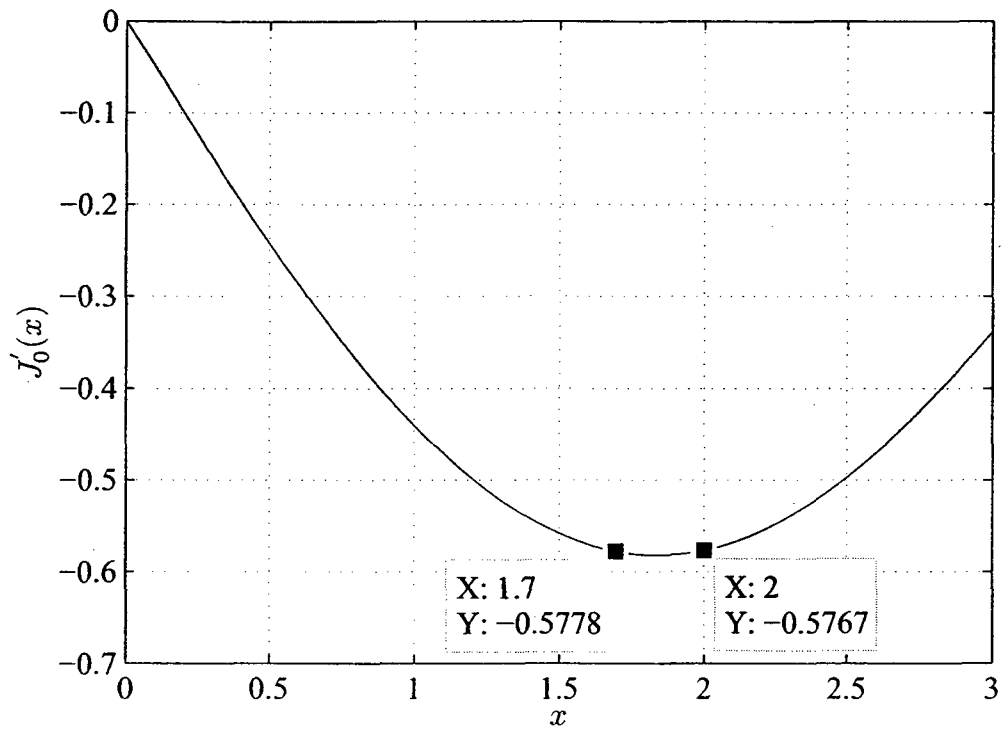

Figure 4.12: Slope of Bessel function $J_0(x)$

small. In other words, f_d is too large such that no point exists within the region, since f_d is proportional to $\frac{1}{k}$ according to Eq. (4.12). In that case, it also can be solved by interpolation, such as spline interpolation method shown in Fig. 4.10. In addition, similar to the zero-crossing scheme, a tiny f_d can also lead to a large estimation error especially when inadequate CIR estimates are used.

Polynomial Curve Fitting Scheme

Since it is essentially a polynomial fitting method, estimation errors can be expected with lower-order polynomials. In the previous section, we discussed about a six-order polynomial (4.10) with an error term of $O(\frac{1}{576})$ when $x \in [0, 2]$. Although higher-order polyno-

mials are more accurate, it on the other hand results in higher computational complexity. Therefore, in the simulation section we only test on a simple yet more precise method, which searches for the $x = J_0^{-1}(y)$ values from a look-up table.

Look-up Table Scheme

This method stores the inverse value of Bessel function into a read-only memory (ROM). Precision is therefore controllable within $[1.7, 2]$. However, despite of such promising features, memory capacity increases with higher accuracy requirement, and meanwhile, the time spent on searching the closest value in the look-up table may also increase. A better searching method such as binary search tree (BST) (see Fig. 4.13) could be utilized to accelerate the searching process [24]. This operation requires a running time of $O(\log n)$ on the average, which is much better than a linear search that requires $O(n)$, especially when searching in a large table that is well-sorted.

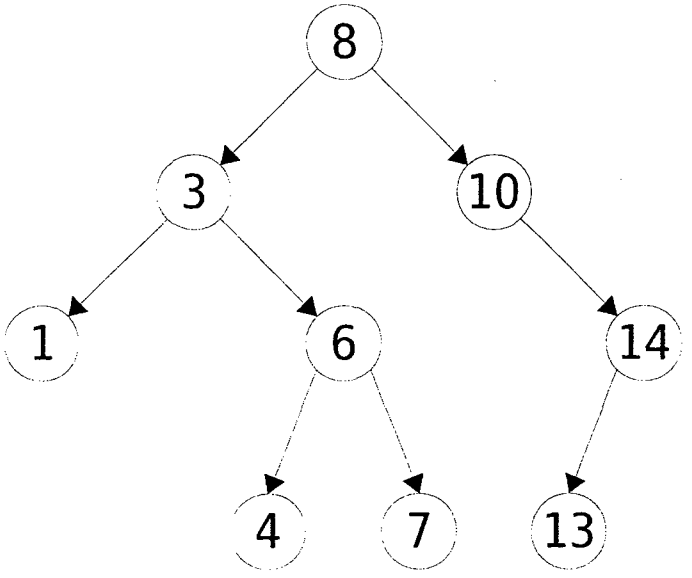

Figure 4.13: A typical binary search tree

4.3.3 Half-period Scheme for LOS DS

Estimation performance also depends on the LOS DS according to $\hat{f}_{d,LOS} = f_d \cos\theta_0 = \frac{\pi}{2\pi k_v T_s} = \frac{1}{2k_v T_s}$. When θ_0 is equal to 90° or $f_d = 0$, the valley point of the ACF curve is thus undetectable, i.e. the first valley point k_v is infinite (Fig. 4.6). And if f_d is tiny or θ_0 is considerably large, more channel estimates are required for an accurate estimation. The extreme case occurs when f_d is small or θ_0 is close to 90 degrees with inadequate channel estimates. In this case, no real valley point exists. The remedy is to consider the minimum value of the ACF min $R_{\Re\Re}(k)$, and the corresponding index k is viewed as the valley point k_v as shown in Fig. 4.14. It shows an offset between the real valley point and the lowest

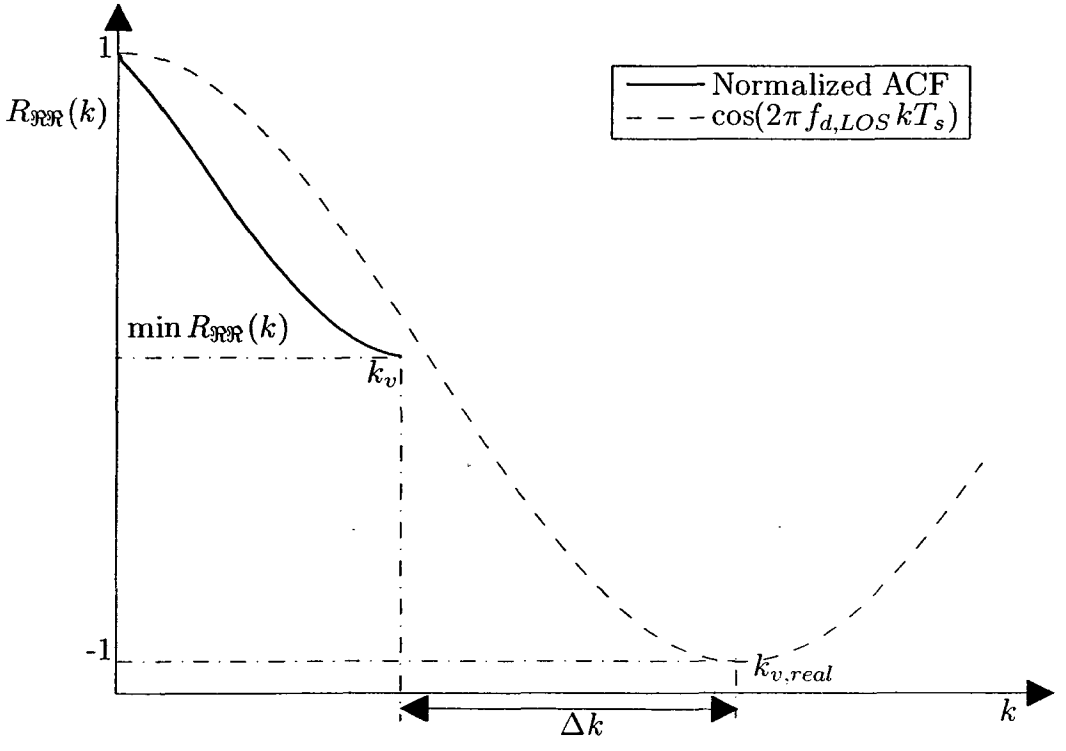

Figure 4.14: ACF when $f_{d,LOS}$ is small

point of the ACF denoted by $\Delta k = k_{v,real} - k_v$, where $k_{v,real}$ is the real valley point. As a very large error could happen in this case, a large number of CIR estimates should be used at the cost of higher computational complexity.

On the other hand, when $f_{d,LOS}$ is quite large, less points are available within one period of ACF. As shown in Fig. 4.15, the smallest valley point has a large shift Δ_1 from the real one and consequently yields an incorrect estimate. Non-linear interpolation can largely improve the performance in such situations as shown in Fig. 4.15, which will be verified in the experiments in the next section.

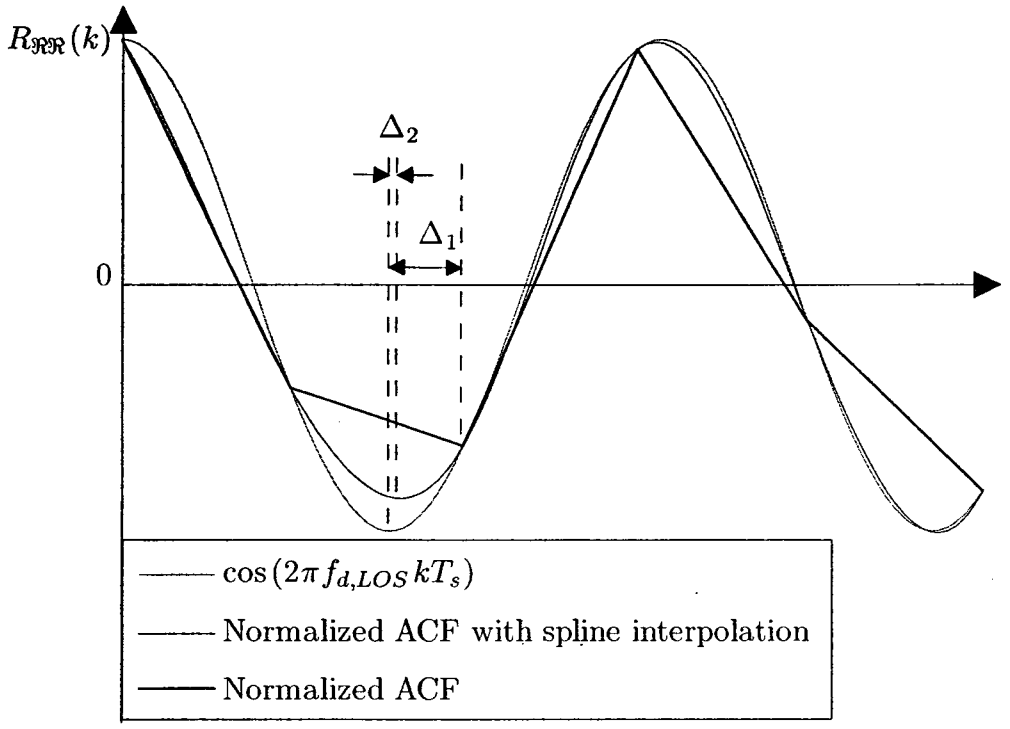

Figure 4.15: Cosine-like ACF curve and interpolation

Besides, since the period of the ACF almost keeps constant as shown in Fig. 4.7, instead of simply picking the first valley point k_v, multiple valley as well as peak points on the ACF

curve can be used together to improve the estimation performance by taking an average of all these valley and peak points against their corresponding periods. The direct path DS is thus determined by

$$\hat{f}_{d,LOS} = \frac{1}{2k_e T_s} \tag{4.38}$$

where k_e denotes the effective first valley point, as given by

$$k_e = \frac{1}{U}\left(\frac{k_1}{1} + \frac{k_2}{2} + \cdots + \frac{k_U}{U}\right) = \frac{1}{U}\sum_{u=1}^{U}\frac{k_u}{u} \tag{4.39}$$

where U is the number of available valley and peak points on the generated ACF curve, and k_u represents those estimated valley and peak points of the uth half-period (π), which are ordered as shown in Fig. 4.16.

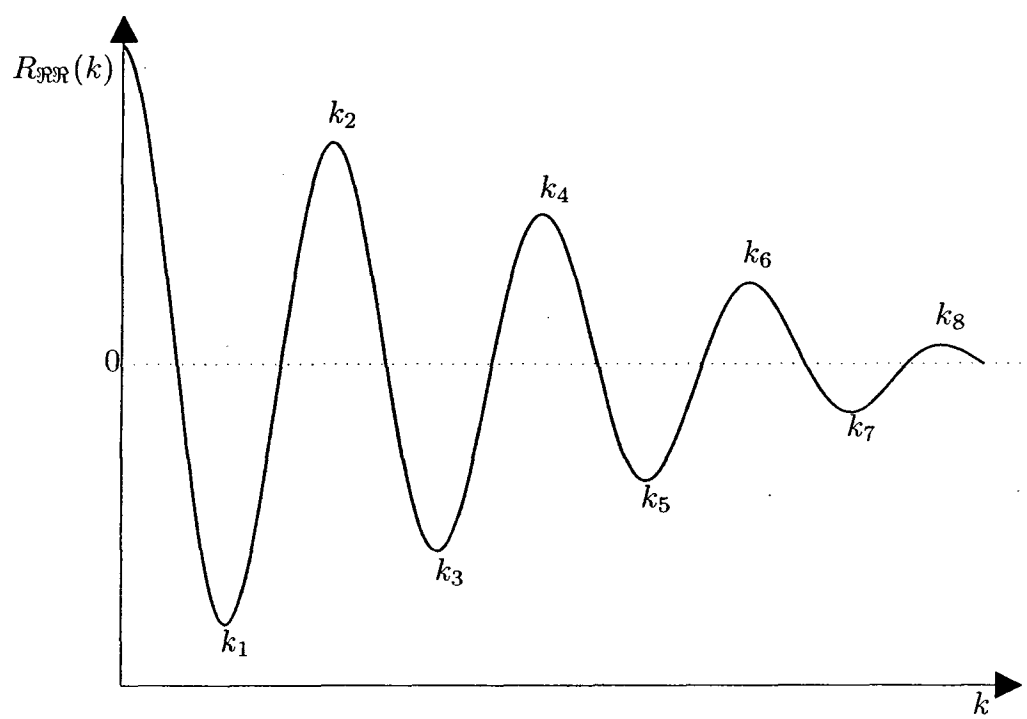

Figure 4.16: Valley and peak points on the ACF curve

4.4 Simulation Results

In this section, the performance of the TSLS channel estimator and the three DS estimators are investigated through computer simulations. Different system parameters and two channel conditions are considered.

4.4.1 Rayleigh Fading Channels

We start with simulation study of the DS estimators in i.i.d. Rayleigh fading channels. By default, a MIMO-OFDM system with 4 receive and 2 transmit antennas is examined. The QPSK modulation is used in the transmitter to create signals with a sample duration of 1 μs. The guard interval is set to be 8, which is equal to the channel length. A total of 16 optimal pilots are inserted equispacedly within one symbol which consists of 128 subcarriers before OFDM modulation. The fading channel is modeled as an 8-tap FIR filter with a maximum DS of 100 Hz. Those channel taps are normalized with averaged path gains of 0 dB, and path delays vary from 0 to $1 \times 8 = 8$ μs by one sample duration of 1 μs. At the receiver side, AWGN is added at each receive antenna with an SNR defined by Eq. (3.11). TSLS channel estimation is performed right after OFDM demodulator, with 100 channel estimates being attained to compute a normalized ACF, which is the average of $N_r \times N_t \times L = 4 \times 2 \times 8 = 64$ ACFs. Thereafter, two DS estimators are simulated and compared. The estimator using a look-up table is tested in the first four experiments, where the precision of the look-up table of $J_0(x)$ is assigned to 10^{-3} with $x \in [1.7, 2]$. In another word, 301 values of Bessel function is stored in advance. In the last three experiments, the DS estimator using look-up table is compared with the one using zero-crossing point.

Experiment 1: Effect of Receive Antenna Configurations

In this experiment, the number of receive antennas varies from 1 to 4, while the transmit antennas are fixed at 2. Here, the normalized mean square error (NMSE) of the estimated DS is defined as

$$\text{NMSE} = \frac{1}{M} \sum_{n_r=1}^{N_r} \sum_{n_t=1}^{N_t} \sum_{l=0}^{L-1} \frac{(\hat{f}_{d,l}^{n_r,n_t} - f_d)^2}{f_d^2} \tag{4.40}$$

where $M = N_r \times N_t \times L$. Note that in Eq. (4.35), ACF is pre-averaged over all channel links of L taps before processing for stability and accuracy. Thus, (4.40) can now be simplified to

$$\text{NMSE} = \frac{(\hat{f}_d - f_d)^2}{f_d^2} \tag{4.41}$$

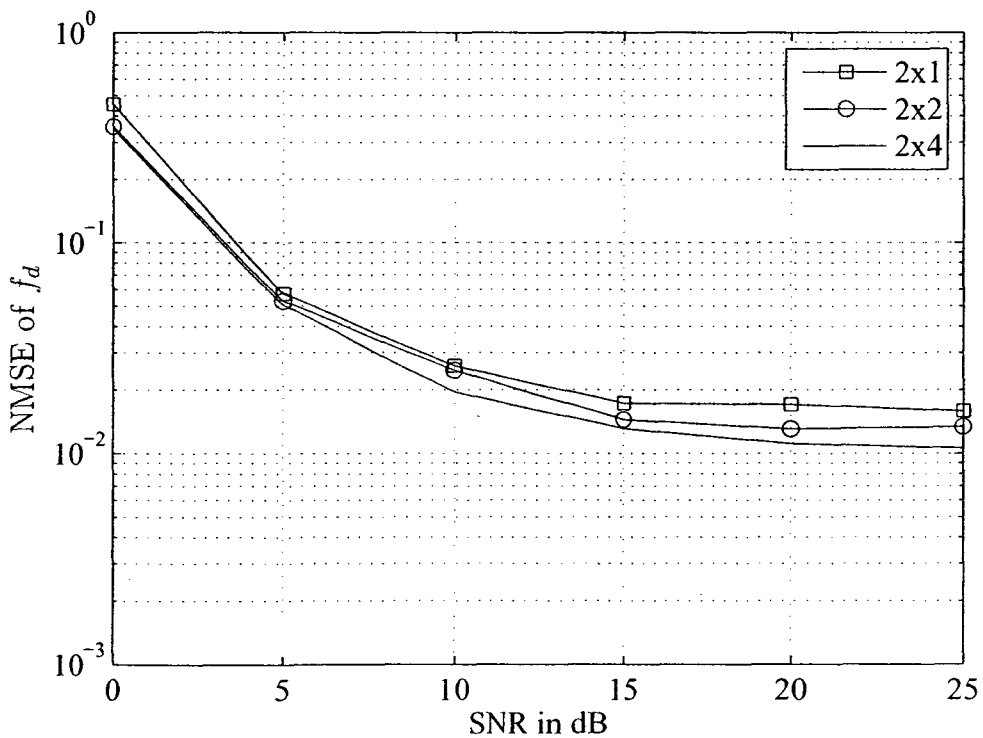

Figure 4.17: NMSE of $\hat{f}_d$ versus SNR for different receive antenna configurations

In a similar test of channel estimator in Chapter 3, it turns out that a 3 dB gain is achieved when receive antennas are doubled. However, as Fig. 4.17 indicates, the performance improvement with increasing the number of receive antennas is almost ignorable, since the average difference between the best ($N_t \times N_r = 2 \times 4$) and the worst ($N_t \times N_r = 2 \times 1$) cases is around 5×10^{-3}. On the other hand, the AWGN has a great effect on the NMSE. As seen from Fig. 4.17, the NMSE gradually decreases as SNR is getting larger, and starts to stabilize at SNR $\approx$ 15 dB. This is due to the disturbance of the TSLS channel estimator, which affects the shape of the generated ACF curve. Therefore, a better channel estimator is required for systems with low SNRs.

Experiment 2: Effect of Guard Intervals

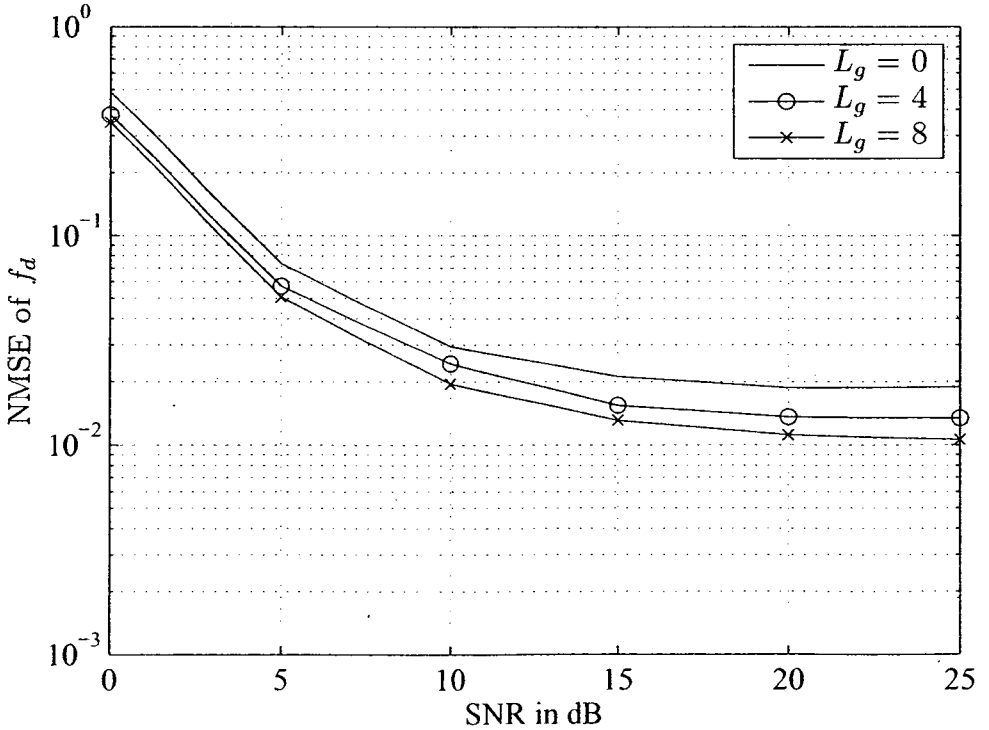

Figure 4.18: NMSE of $\hat{f}_d$ versus SNR with regard to guard interval

This experiment compares the performance of the DS estimator with different guard intervals or CP. From Fig. 4.18, we could confirm that sufficient guard length L_g, which is no less than the maximum channel length L ($L = 8$), results in a promising performance. In addition, the tolerance of unpredictable path delays makes it a satisfactory estimator.

Experiment 3: Effect of Optimal Pilots

In this experiment, the system is performed with different numbers of optimal pilots over one OFDM symbol, which varies from a minimum of 16 pilots to 128 pilots or pilot symbol. A better performance is observed in Fig. 4.19, which is due to a larger amount of pilots. When pilot symbols are utilized in the simulation, the performance of partial-curve

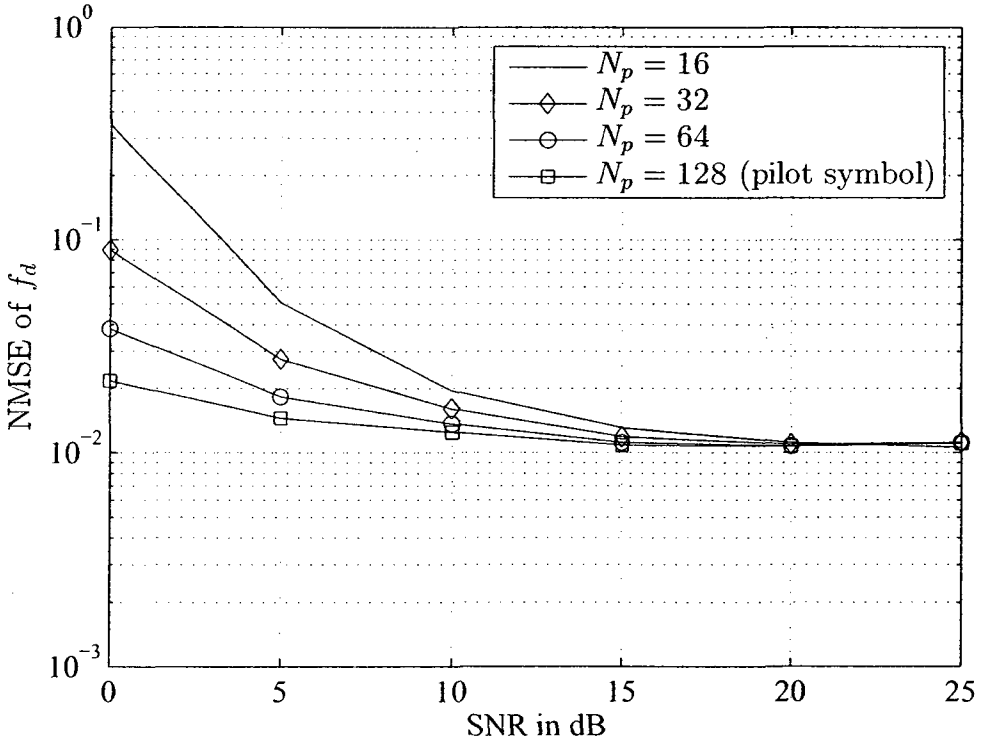

Figure 4.19: NMSE of $\hat{f}_d$ versus SNR with different number of pilots

algorithm which is SNR-sensitive can be largely improved especially at low SNRs. Therefore, a better channel estimation scheme, such as the combination of optimal pilots and data stream, a.k.a. semi-blind channel estimation, is required for ACF based DS estimators using part of the ACF curve.

Experiment 4: Effect of Sample Rates

In this experiment, two MIMO-OFDM systems with different sample rates are investigated as shown in Fig. 4.20. The figure indicates that a system with a longer symbol duration has

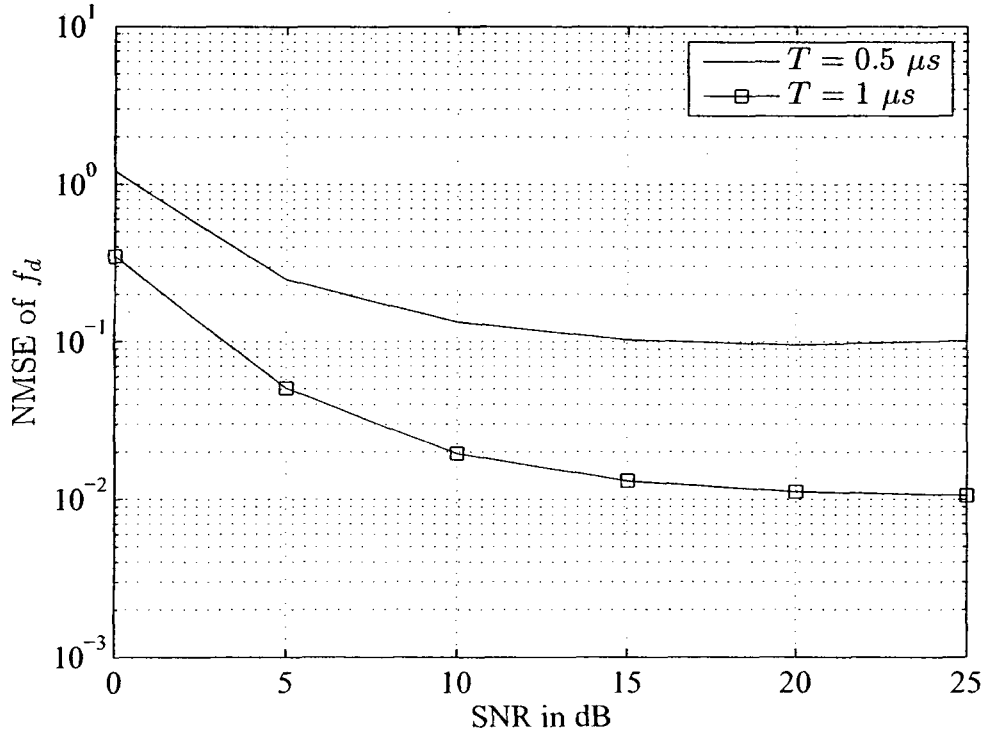

Figure 4.20: Comparison between systems with different sample rates of 1 μs and 0.5 μs

a better performance. According to $k = x/(2\pi f_d T_s)$, the index k is inverse proportional to the symbol duration T_s for a specific f_d and same amount of CIR estimates. As a result, longer symbol duration leads to a smaller k, or in other words, with the same amount of

CIR estimates required to form the ACF curve, a DS estimator with a small k can be much more accurate than that with a large k.

Experiment 5: Comparison of Two Estimators with Different Number of CIR Estimates

In this experiment, the proposed two estimators are compared at 20 dB. Since $f_d = 100$ Hz, the amount of available points within $[0, 2.4048]$ can be calculated by

$$k = \frac{2.4048}{2\pi f_d T_s} = \frac{0.3828}{100 \cdot (128+8) \cdot 10^{-6}} \approx 28$$

which means, at least 28 CIR estimates are required for generating the ACF curve on $[0, 2.4048]$. Hence, a number of CIR estimates varying from 50 to 1000 should be sufficient.

Undoubtedly, Fig. 4.21 indicates that with the increase of CIR estimates for ACF generation, higher accuracy is achieved. The zero-crossing scheme performs better with a small number of CIR estimates, however, with adequate estimates, the estimator using partial ACF curve overtakes the former when the number of CIR estimates reaches 200. Therefore, we could conclude that the zero-crossing scheme is suitable for the situation where a small number of CIR estimates are available at the estimator, while the partial-curve scheme is for higher accuracy purposes. Besides, for the partial-curve estimator, the accuracy will infinitely near 0 as long as we provide with more accurate channel estimates and a look-up table that has a higher precision; on the other hand for the zero-crossing estimator, the precision is limited, it depends on the precision of the two points k_1 and $k_1 + 1$, which are affected by various factors according to Eq. (4.6).

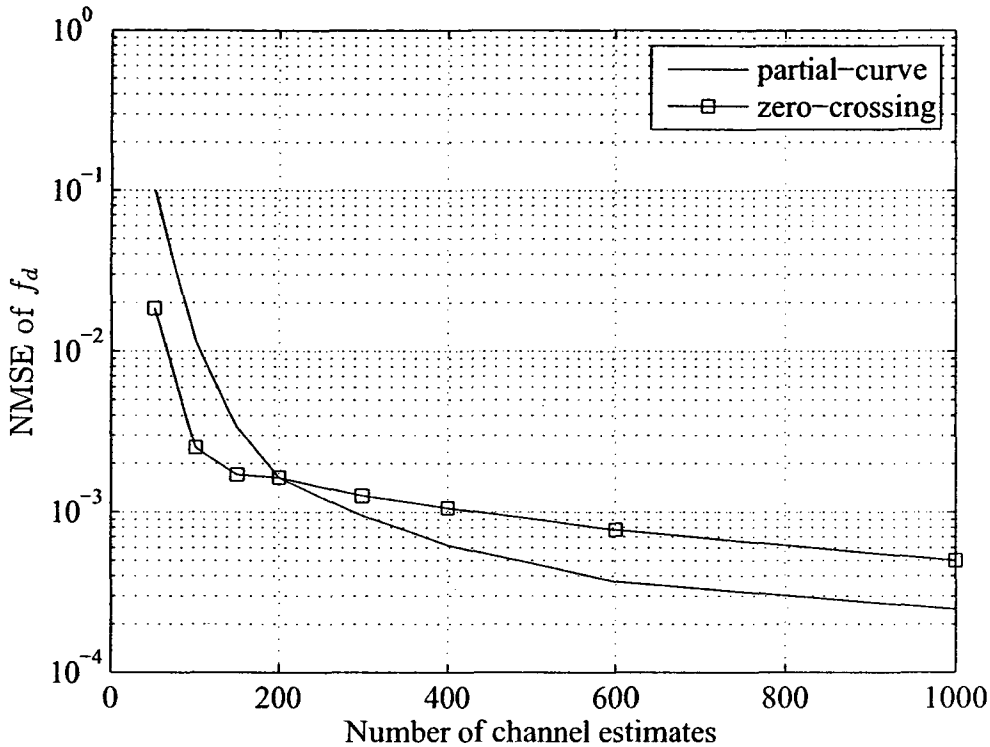

Figure 4.21: Comparison of two estimators with different number of CIR estimates

Experiment 6: Comparison of Two Estimators for Different DSs with A Spline Interpolation Enhanced Method

Two schemes are implemented and examined for different DS varying from 50 Hz to 1 kHz, when SNR equals 20 dB and 100 channel estimates are used. As it is shown in the Fig. 4.22, generally no matter which scheme we choose, a better performance is observed with larger DS. Unsurprisingly, partial-curve scheme does a better job than its counterpart when $f_d > 200$ Hz.

In this experiment, the minimal channel estimates required for obtaining the first zero-crossing point varies from $2.4048/(2\pi 50 \cdot 10^{-6}(128+8)) \approx 56$ down to $2.4048/(2\pi 1000 \cdot 10^{-6}(128+8)) \approx 3$. Hence, larger DS can result in higher accuracy. A performance loss

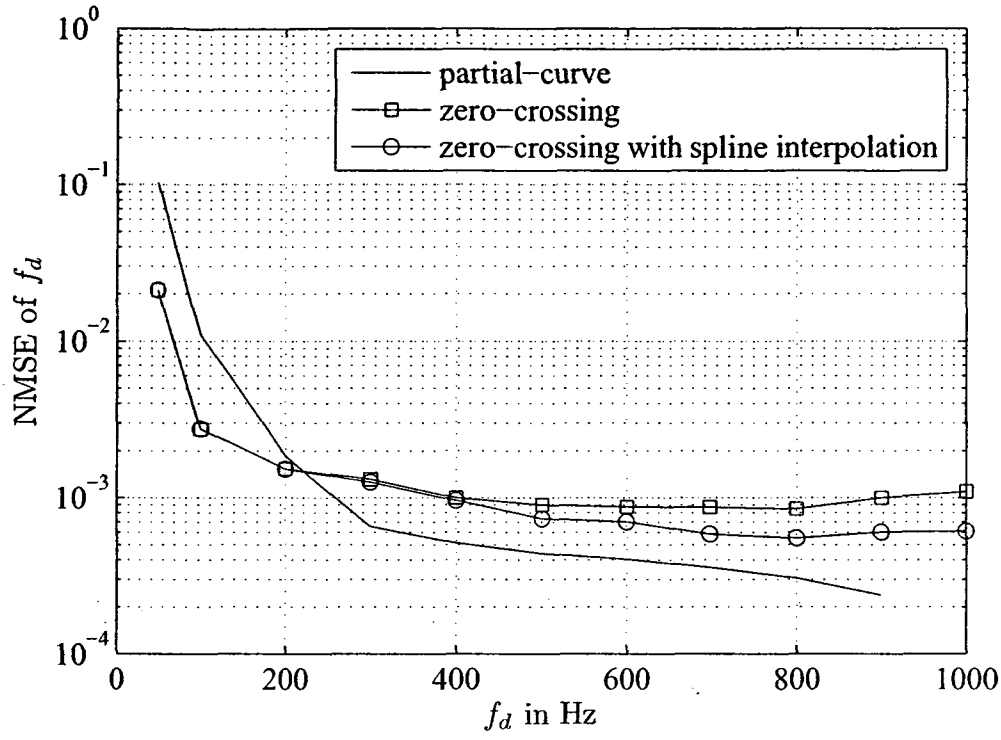

Figure 4.22: Comparison of two estimators for different DSs with a spline interpolation enhanced method at 20 dB

of zero-crossing scheme has happened as expected when DS is extremely large, which is due to the low precision of the two points k_1 and $k_1 + 1$ that determine the zero-crossing point by linear interpolation.

However, we can see that the partial-curve scheme is unable to detect the DS at 1000 Hz, which is due to nonexistence of $R_{\Re\Re}(k)$ within the optimally chosen span of the ACF curve: $[1.7, 2]$. It can be solved by expanding the stated span, which may increase error probability or introducing interpolation methods without any performance gain though.

As has been analysed in the preceding section, this experiment confirms that, the performance of zero-crossing method degrades with the increment of f_d at higher DSs. Thus, we compare the original zero-crossing method with the spline-interpolation powered one,

and the latter shows a performance gain at large DSs.

Experiment 7: Comparison of Two Estimators at Different SNRs

The simulation is carried out at 0 and 20 dB respectively for both estimators at different DSs varying from 50 to 1000 Hz. Simulation results from Fig. 4.23 show that zero-crossing

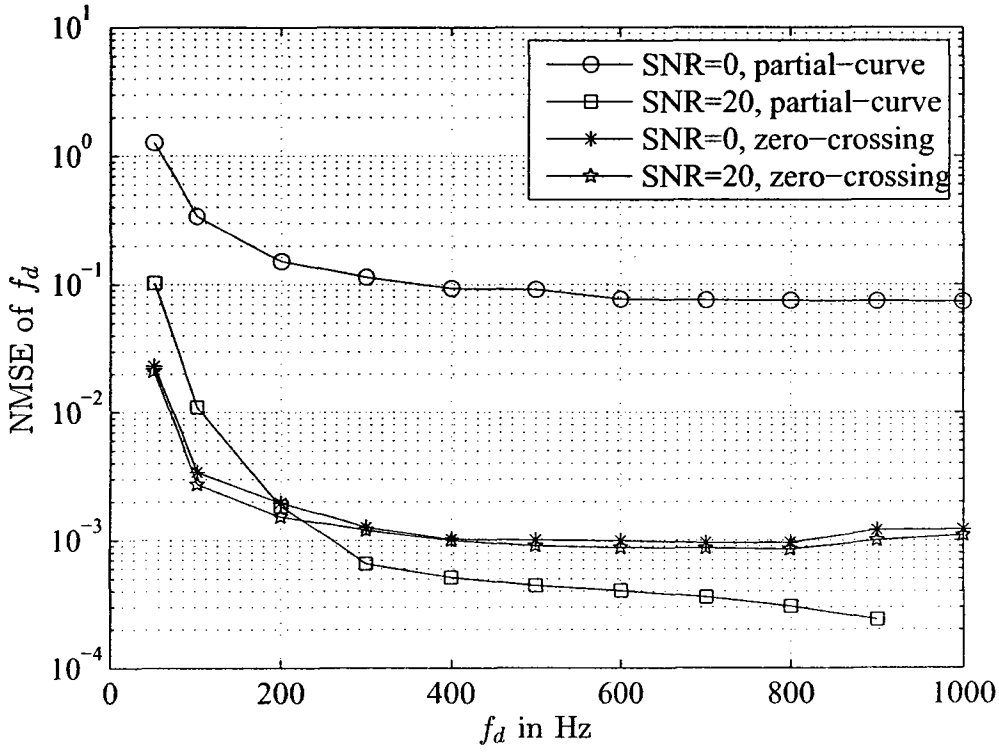

Figure 4.23: Comparison of two estimators at different SNRs

scheme is almost noise-insensitive with a slightly performance loss at 0 dB. On the contrary, partial-curve scheme performs relatively worse than its rival at low SNRs, which can be improved by introducing better channel estimation algorithms according to Experiment 3. We could also conclude that, the zero-crossing scheme is more suitable for severe channel conditions and a low accuracy requirement; and the other scheme is better for high accuracy

purpose at moderate to higher SNRs.

4.4.2 Rician Fading Channels

All of the previous experiments are carried out in Rayleigh fading channels. While in the next five experiments, Rician fading channel is considered with similar system parameters except for an LOS component with specific K-factors and different AOAs. By default, it is modeled as an 8-tap FIR with 2 transmit and 4 receive antennas, only the first tap or non-delay path is assumed to be Rician fading with an AOA of 0 degree and a K-factor of 10, and other paths are normal Rayleigh fading channels with a maximum DS of 100 Hz, in another word, the direct path DS is set to the same as maximum DS $f_{d,LOS} = f_d \cos\theta_0 = 100 \cdot \cos 0 = 100$ Hz. The normalized ACF is generated and averaged by employing all channel links of the first tap, which contains $N_r \times N_t = 4 \times 2 = 8$ links. In the following experiments, we merely examine the performance of the direct path DS estimator, since other NLOS paths are all Rayleigh fading processes which can be utilized to calculate DS by corresponding estimators, and the performance is supposed to be the same as those in Rayleigh fading channels. The direct path DS estimator makes full use of all the valley and peak points on the normalized ACF curve generated by channel estimates, and the DS is calculated by Eq. (4.38).

Experiment 1: Effect of SNR

In this experiment, the estimation is performed for SNRs varying from 0 to 25 dB as shown in Fig. 4.24. Clearly, the proposed estimator for direct path DS is noise-insensitive. The poorly estimated CIRs at low SNRs indeed affect the shape of the generated ACF curve.

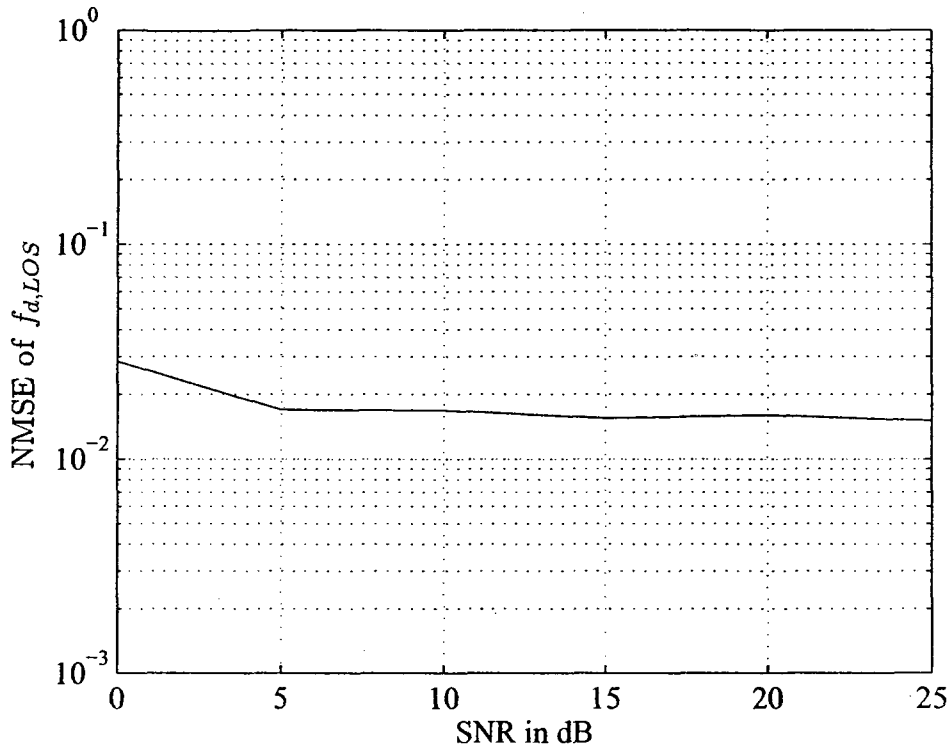

Figure 4.24: NMSE of $\hat{f}_{d,LOS}$ versus SNR

however, those peak or valley points do not make remarkable offsets from their real positions. Moreover, the average of ACFs over all the links of the first channel tap, which in this case is $N_r \times N_t = 4 \times 2 = 8$ in total, can greatly relieve the effect of AWGN (see Fig. 4.9). On the other hand, the average of all peak and valley points by Eq. (4.38) and (4.39) provides a considerably higher accuracy than a single valley point representing the first half period of ACF.

Experiment 2: Effect of CIR Estimates

In this experiment, we investigate the performance of the proposed LOS DS estimator using different number of CIR estimates with a SNR of 20 dB. Here, we assume the direct path DS

is 200 Hz, as doubled peak or valley points are available on the ACF curve with 100 points in total than that of 100 Hz, so as to make estimation results more stable. For example, the available points during one period of the ACF with a $f_{d,LOS} = 100$ Hz is $1/(100 \cdot 10^{-6} \cdot (128 + 8)) \approx 73$, while the one with a $f_{d,LOS} = 200$ Hz is $1/(200 \cdot 10^{-6} \cdot (128 + 8)) \approx 36$. For a specific number of channel estimates, e.g. 100, the former offers $100/73 \approx 1$ period, or a valley point plus a peak point for further averaging. While the latter offers $100/36 \approx 2.5$ periods, or in other words, 4 valley points along with 3 peak points for averaging. Obviously, the latter is much more stable and accurate.

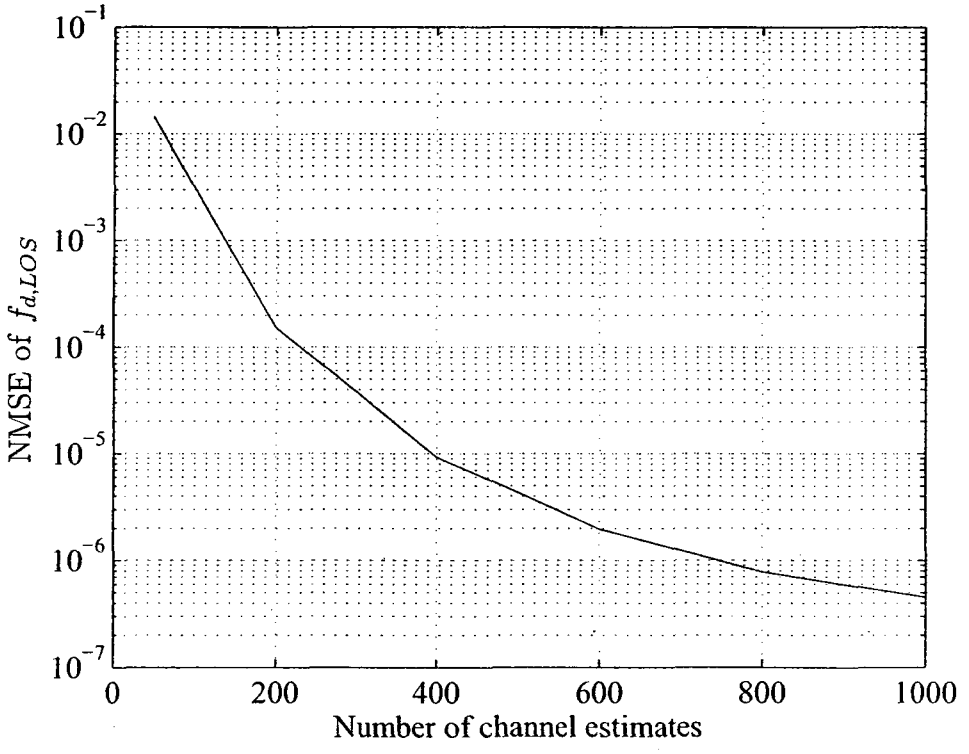

Figure 4.25: NMSE of $\hat{f}_{d,LOS}$ versus number of channel estimates

Simulation results show that the performance improves rapidly as we increase the number of CIR estimates utilized for ACF generation. We can also presume from Fig. 4.25 that

the NMSE will reach a limit around 10^{-7} with more than 1000 CIR estimates. According to Eq. (4.38) and (4.39), with more channel estimates, more periods, or peak and valley points of the ACF curve are available for average, thus giving a more accurate yet stable result.

Experiment 3: Effect of K-factor

This experiment simply investigates the effect of K-factor when SNR equals 20 dB. According to our assumption in the previous section, the ACF curve is cosine-like when K is considerably large. Fig. 4.26 implies that, with the increase of K-factor, the NMSE of the

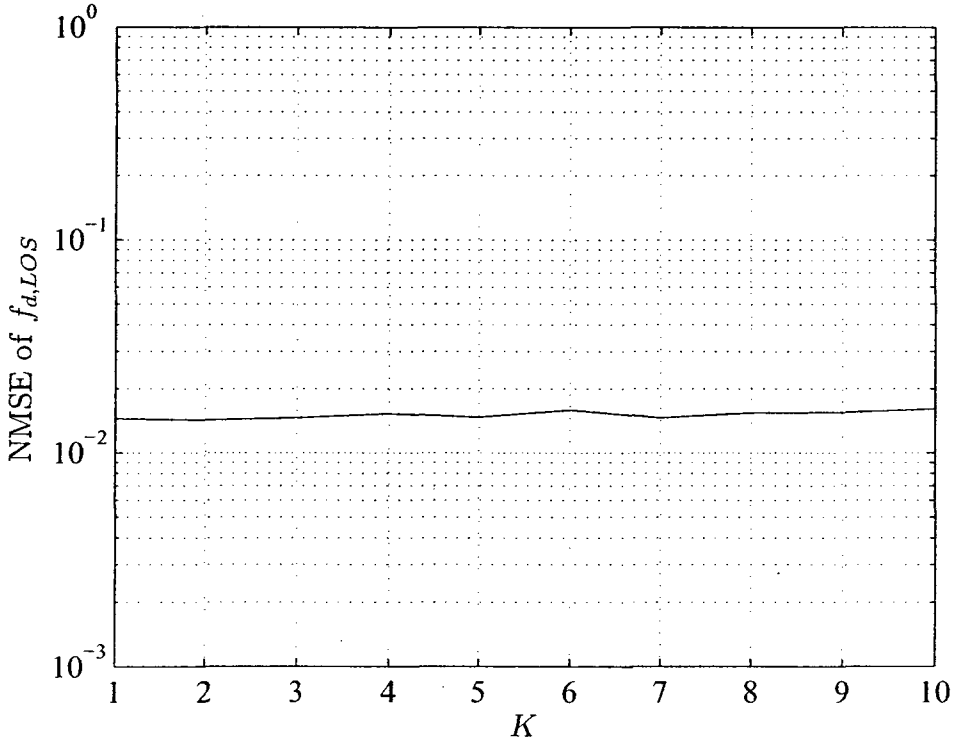

Figure 4.26: Effect of K-factor

estimator keeps almost constant, which means the proposed algorithm for estimating the

direct path DS is very suitable for Rician fading channels. Nevertheless, we should note that these simulation results are based on quantities of Monte Carlo tests, which provides an average performance. Thus, a lower K-factor may lead to unstable estimates in real-time processing as the ACF curve is influenced by the NLOS components from Eq. (4.15).

Experiment 4: Effect of AOA

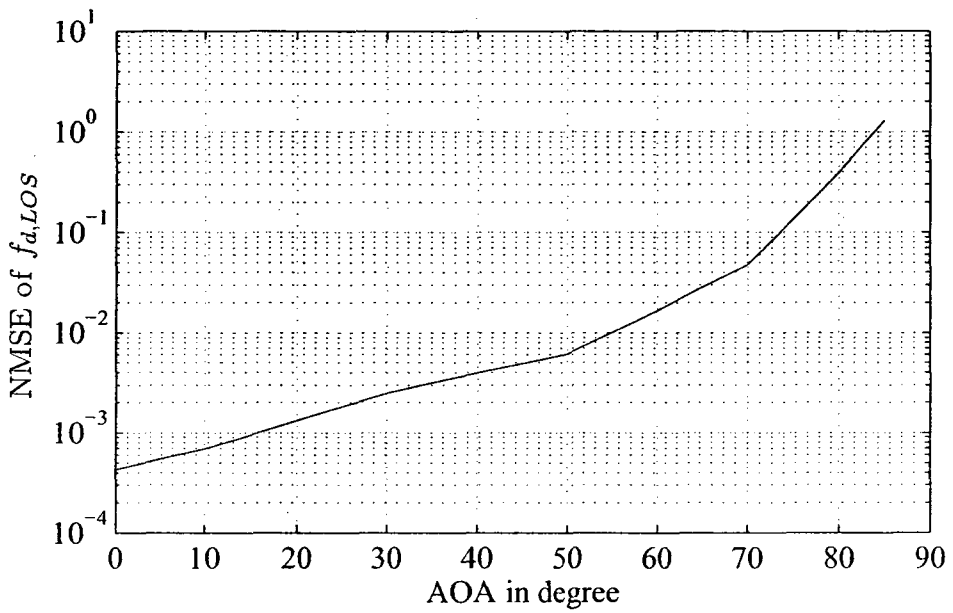

Figure 4.27: Effect of AOA

This experiment investigates a MIMO-OFDM system in the Rician fading channels with a maximum DS of 200 Hz at 20 dB. The AOA is varying from 0 to 85 degrees, and correspondingly the direct path DS ranges between 17 Hz and 200 Hz according to $f_{d,LOS} = f_d \cos\theta_0$. In addition, 100 channel estimates are in use. Hence, no real valley point exists (Fig. 4.14) when AOA is no less than 80 degrees, that is to say more than $1/(2 \cdot (128+8) \cdot 10^{-6} \cdot 200 \cdot \cos 80°) \approx 106 > 100$ points are required for obtaining a valley point on the ACF curve. As discussed in the previous section, we choose the minimum of $\hat{R}_{\Re\Re}(k)$ as

the valley point, which causes the estimation error shown in Fig. 4.27.

Starting from 80 degrees, CIR estimates becomes insufficient for searching for the real smallest valley point of the ACF curve. Those estimated direct path DSs are thus unreliable. The extreme case occurs when $\theta_0 = 90°$, i.e. $f_{d,LOS} = 0$, the index $k \to \infty$, which means $f_{d,LOS}$ is undetectable. We can also conclude from Fig. 4.27 that, when AOA is smaller or equivalently $f_{d,LOS}$ is relatively larger, a better estimation performance is obtained.

Experiment 5: Estimation of $f_{d,LOS}$ with and without Interpolation

This experiment investigates the estimation performance with different LOS DSs. We have analyzed the possible performance degradation due to inadequate points during one period of the ACF curve when $f_{d,LOS}$ gets larger, which is shown in Fig. 4.15. To overcome such drawback, non-linear interpolation is implemented. Through extensive simulations, we have found that spline interpolation is the best method to improve the estimation accuracy. A total of 200 channel estimates are used for ACF generation to make sure at least 1 period of ACF curve is available.

Fig. 4.28 shows two simulation plots obtained under 20 dB with $f_{d,LOS}$ varying from 50 to 1000 Hz. Similar to the proposed estimators for Rayleigh fading channels, the index k is inverse proportional to $f_{d,LOS}$. Thus, for a larger DS, fewer points are required to generate an ACF curve within a period. On the other hand, with fewer points during one period, the valley or peak points, which are estimated by searching for the minimum or maximum value of ACF within their spans, are very likely to have an offset from the real valley or peak points, as shown in Fig. 4.15. Therefore, thanks to the average of all available peak and valley points on the ACF curve, a performance gain is achieved at large $f_{d,LOS}$s. With the

help of spline interpolation, a noticeable improvement emerges when $f_{d,LOS}$ varies between 200 and 1000 Hz.

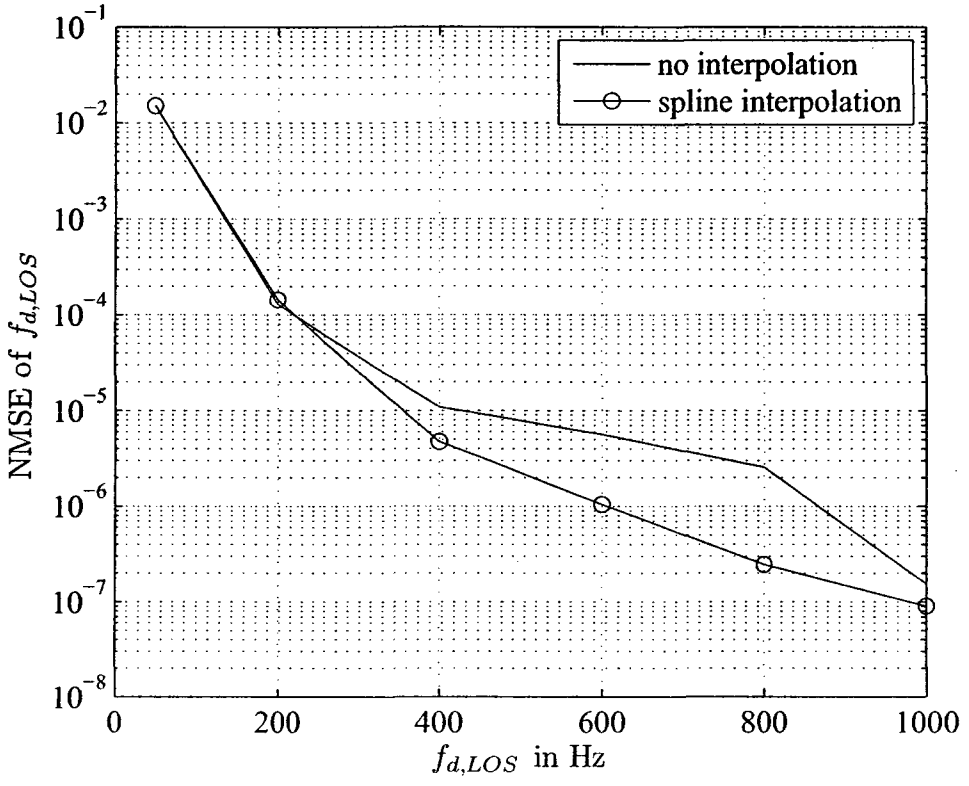

Figure 4.28: NMSE of $f_{d,LOS}$ versus f_d with and without spline interpolation

4.5 Conclusions

In this chapter, four DS estimation algorithms have been proposed for MIMO-OFDM systems by taking Rayleigh and Rician fading channels into consideration, which employ the ACF generated by the TS based channel estimation utilizing LS algorithm. A zero-crossing algorithm is proposed in the first place, followed by two algorithms that make use of part of the ACF curve, one of which calculates the inverse of Bessel function by polynomial

curve fitting, and the other searches for the nearest values of Bessel function by a look-up table. Then, the fourth estimator is proposed for MIMO-OFDM systems in Rician fading channels, which searches for valley and peak points in each period of the ACF. A detailed analysis of estimation accuracy and computational complexity is presented for the proposed DS estimators, along with several suggestions on various situations.

Thereafter, a computer simulation study of the proposed DS estimators is carried out with different system parameters and channel conditions. In Rayleigh fading channel case, seven experiments are performed including different antenna configurations, guard intervals, optimal pilots, signal sample rates, channel estimates and comparisons between the zero-crossing scheme and look-up table scheme with regard to different SNRs and interpolation approach. While in Rician fading channel case, five experiments are performed including different SNRs, amount of channel estimates, K-factors, angle of arrivals, and comparisons of the estimators with and without the enhancement of interpolation.

Finally, we can conclude from all the simulation results that, under moderate noise conditions with adequate MIMO channel estimates, ACF based DS estimators provide promising performance for MIMO-OFDM systems in either Rayleigh or Rician fading channels. All proposed estimators perform well in fast-fading channels, or large DSs; while in slow-fading channels, or in other words, with small DSs, higher computational complexity is required. As for specific estimators, the zero-crossing scheme is very noise-insensitive, which is well suited for severe channel conditions and a moderate accuracy requirement. The partial-curve schemes offer higher accuracy, although at low SNRs they do not perform as well as that at higher SNRs. Besides, non-linear interpolation method such as spline interpolation can be regarded as enhancement of the proposed estimators in particular situations.

Chapter 5

Conclusions and Future Work

5.1 Summary

In this thesis, the TS based channel estimation issue of MIMO-OFDM systems has been first studied. The resulting channel estimates are then utilized to develop the ACF based DS estimators. Thereafter, four ACF based DS estimation methods for MIMO-OFDM systems have been proposed under both Rayleigh and Rician fading channels, with detailed accuracy analysis. Computer simulations and comparisons have been carried out to investigate the performance and computational complexity of different schemes.

The first chapter has highlighted the next generation wireless communication techniques, including the MIMO and OFDM systems, their channel estimation and DS estimation for performance improvement.

In Chapter 2, the latest techniques for wireless communication systems, such as MIMO and OFDM technologies, have been briefly reviewed along with basic concepts of DS and wireless channel models. The combination of MIMO and OFDM techniques have also been

discussed.

Chapter 3 is dedicated to a TS based MIMO channel estimation method. First, the modelling of MIMO-OFDM systems including the transceiver, channel model, signal model and the design of optimal pilots has been studied. Next, we have studied channel estimation in the time domain for MIMO-OFDM systems, followed by a simulation study with several system parameters and channel conditions to prove the reliability of the channel estimation algorithm.

Finally in Chapter 4, four ACF based DS estimation schemes for i.i.d. MIMO-OFDM systems have been proposed under Rayleigh and Rician fading channels. Three of them are used in NLOS paths, in which one calculates the DS by employing the first zero-crossing point of ACF, while others employ partial ACF curve for obtaining the direct inverse of Bessel function by polynomial curve fitting and looking up a table, respectively. The remaining estimator is particularly for the LOS paths, which utilizes the periodicity of ACF curve. After that, we have performed plenty of experiments to study the performance of the proposed four DS estimators. The simulation results have shown that, the zero-crossing scheme achieves rather homogeneous performance for all channel conditions and a relative low computational complexity than partial-curve schemes, which makes it perfect for general use; whereas the partial-curve scheme performs better under relative better channel conditions, making them more suitable for higher accuracy situations. Also a satisfactory performance of the direct path DS estimator for LOS paths has been shown in MIMO-OFDM systems with various K-factors and channel conditions. Moreover, non-linear interpolation techniques have also been implemented for the proposed estimators under certain circumstances as far as the performance and stability issues are concerned.

5.2 Future Research

The possible directions of future research are listed as follows:

- As described in this thesis, ideally uncorrelated channel model has been chosen. Although it is widely accepted as an effective model, in practice, correlated channel is possibly expected, for instance, insufficient antenna spacing. Therefore, correlated channel model should be considered in the future research with proper channel estimation algorithms [25] and corresponding decorrelation techniques.

- The TS based channel estimation algorithm has been used for further Doppler estimation. While it has one drawback, that is, sacrificing frequency efficiency to get a more reliable estimation result. This can be solved by introducing a combination of training sequence and blind estimation schemes, which is well known as the semi-blind algorithm [4][5]. The idea of semi-blind channel estimation is a good compromise both in performance and frequency usage, which is very helpful in modern wireless communication systems.

- We have assumed perfect timing and ideal signal shaping in this thesis. However, in practice, we have to take those issues into consideration. Therefore, timing synchronization and pulse shaping methods could play important roles in my future work.

- As a frequency synchronization scheme, DS estimation is very important in signal recovery and many other tasks in receivers, especially in mobile communications. Thus, more work on such implementations is needed.

- A simplified model for MIMO-OFDM systems has been used in the thesis. More MIMO-OFDM related techniques such as space-time coding [3][26] and solutions to PAPR problem shall be integrated into the system model.

Bibliography

[1] Y. K. Kim and P. Ramjee, *4G Roadmap and Emerging Communication Technologies*. Artech House 2006, 2006.

[2] S. Hussain, Z. Hamid, and N. S. Khattak, ``Mobility management challenges and issues in 4G heterogeneous networks," in *InterSense '06: Proceedings of the first international conference on Integrated internet ad hoc and sensor networks*, (New York, NY, USA), p. 14, ACM, 2006.

[3] B. Vucetic and J. Yuan, *Space-Time Coding*. Wiley, 2003.

[4] V. Barroso and J. Xavier, ``Blind identification of MIMO channels: a closed form solution based on second order statistics," in *Conference Record of the Thirty-Third Asilomar Conference on Signals, Systems, and Computers*, vol. 1, pp. 70--74, Oct. 24--27, 1999.

[5] A. Medles, D. T. M. Slock, and E. De Carvalho, ``Linear prediction based semi-blind estimation of MIMO FIR channels," in *Proc. IEEE Third Workshop on Signal Processing Advances in Wireless Communications (SPAWC '01)*, pp. 58--61, Mar. 20--23, 2001.

[6] M. Biguesh and A. B. Gershman, ``MIMO channel estimation: optimal training and tradeoffs between estimation techniques," in *Proc. IEEE International Conference on Communications*, vol. 5, pp. 2658--2662, June 20--24, 2004.

[7] C. Tepedelenlioglu, A. Abdi, G. B. Giannakis, and M. Kaveh, ``Estimation of Doppler spread and signal strength in mobile communications with applications to handoff and adaptive transmission," *Wireless Communications and Mobile Computing*, vol. 1, no. 2, pp. 221--242, 2001.

[8] B. Sheng and X. You, ``Joint estimation of Doppler spread and carrier frequency offset of OFDM systems," *IEICE Transactions on Fundamentals*, vol. E88-A(11), pp. 3134--3136, 2005.

[9] T. Yucek, R. M. A. Tannious, and H. Arslan, ``Doppler spread estimation for wireless OFDM systems," in *Proc. IEEE/Sarnoff Symposium on Advances in Wired and Wireless Communication*, pp. 233--236, Apr. 18--19, 2005.

[10] J. Cai, W. Song, and Z. Li, ``Doppler spread estimation for mobile OFDM systems in Rayleigh fading channels," *IEEE Transactions on Consumer Electronics*, vol. 49, pp. 973--977, Nov. 2003.

[11] Y.-C. Ko and G. Jeong, ``Doppler spread estimation in mobile communication systems," in *Proc. IEEE 55th Vehicular Technology Conference VTC Spring 2002*, vol. 4, pp. 1941--1945, May 6--9, 2002.

[12] L. Krasny, H. Arslan, D. Koilpillai, and S. Chennakeshu, ``Doppler spread estimation

in mobile radio systems," *IEEE Communications Letters*, vol. 5, pp. 197--199, May 2001.

[13] D. Tse and P. Viswanath, *Fundamentals of Wireless Communication*. Cambridge University Press, 2005.

[14] J. W. Mark and W. Zhuang, *Wireless Communications and Networking*. Prentice Hal, 2002.

[15] M. Pätzold, *Mobile Fading Channels*. Wiley, 2002.

[16] W. Jakes, *Microwave Mobile Communications*. Piscataway, NJ: IEEE Press, 1st ed., 1993.

[17] R. van Nee and R. Prasad, *OFDM for Wireless Multimedia Communications*. Artech House, 2000.

[18] Y. Li, N. Seshadri, and S. Ariyavisitakul, ``Channel estimation for OFDM systems with transmitter diversity in mobile wireless channels," *IEEE Journal on Selected Areas in Communications*, vol. 17, pp. 461--471, Mar. 1999.

[19] S. Ohno and G. B. Giannakis, ``Optimal training and redundant precoding for block transmissions with application to wireless OFDM," *IEEE Transactions on Communications*, vol. 50, pp. 2113--2123, Dec. 2002.

[20] I. Barhumi, G. Leus, and M. Moonen, ``Optimal training design for MIMO OFDM systems in mobile wireless channels," *IEEE Transactions on Signal Processing*, vol. 51, pp. 1615--1624, June 2003.

[21] M. C. Jeruchim, P. Balaban, and K. S. Shanmugan, *Simulation of Communication Systems*. Plenum Press, 1992.

[22] H. Schober and F. Jondral, ``Velocity estimation for OFDM based communication systems,'' in *Proc. VTC 2002-Fall Vehicular Technology Conference 2002 IEEE 56th*, vol. 2, pp. 715--718, Sept. 24--28, 2002.

[23] D. E. Amos, ``Algorithm 644: A portable package for Bessel functions of a complex argument and nonnegative order,'' *ACM Trans. Math. Softw.*, vol. 12, no. 3, pp. 265--273, 1986.

[24] D. A. Heger, ``A disquisition on the performance behaviour of binary search tree data structures,'' *European Journal for the Informatics Professional*, vol. V, pp. 67--75, October 2004.

[25] H. Zhang, Y. Li, A. Reid, and J. Terry, ``Optimum training symbol design for MIMO OFDM in correlated fading channels,'' *IEEE Transactions on Wireless Communications*, vol. 5, pp. 2343--2347, Sept. 2006.

[26] V. Tarokh, H. Jafarkhani, and A. R. Calderbank, ``Space-time block codes from orthogonal designs,'' *IEEE Transactions on Information Theory*, vol. 45, pp. 1456--1467, July 1999.

[27] S. M. Alamouti, ``A simple transmit diversity technique for wireless communications,'' *IEEE Journal on Selected Areas in Communications*, vol. 16, pp. 1451--1458, Oct. 1998.

[28] R. Chang and R. Gibby, ``A theoretical study of performance of an orthogonal multiplexing data transmission scheme," *IEEE Transactions on Communication Technology*, vol. 16, pp. 529--540, Aug. 1968.

[29] D. Chizhik, J. Ling, P. W. Wolniansky, R. A. Valenzuela, N. Costa, and K. Huber, ``Multiple-input-multiple-output measurements and modeling in Manhattan," *IEEE Journal on Selected Areas in Communications*, vol. 21, pp. 321--331, Apr. 2003.

[30] J. P. Kermoal, L. Schumacher, K. I. Pedersen, P. E. Mogensen, and F. Frederiksen, ``A stochastic MIMO radio channel model with experimental validation," *IEEE Journal on Selected Areas in Communications*, vol. 20, pp. 1211--1226, Aug. 2002.

[31] G. Mkrtchyan, K. Naito, K. Mori, and H. Kobayashi, ``Doppler spread estimation method for OFDM signal using mean squareof channel impulse response's time derivative," *IEICE Transactions on Communications*, vol. E89-B, pp. 2961--2966, 2006.

[32] D.-S. Shiu, G. J. Foschini, M. J. Gans, and J. M. Kahn, ``Fading correlation and its effect on the capacity of multielement antenna systems," *IEEE Transactions on Communications*, vol. 48, pp. 502--513, Mar. 2000.

[33] A. Leon-Garcia, *Probability and Random Processes for Electrical Engineering*. Prentice Hall, 2nd ed., 1993.

[34] H. Liu and G. Li, *OFDM-Based Broadband Wireless Networks*. WILEY-INTERSCIENCE, 2005.

[35] A. V. Oppenheim and R. W. Schafer, *Discrete-time signal processing*. Prentice Hall, 2nd ed., 1999.

[36] J. G. Proakis, *Digital Communications*. McGraw-Hill Science/Engineering/Math; 4 edition, 2000.

[37] C.-N. Chuah, J. M. Kahn, and D. Tse, ``Capacity of multi-antenna array systems in indoor wireless environment," in *Proc. Bridge to Global Integration. IEEE Global Telecommunications Conference GLOBECOM 98*, vol. 4, pp. 1894--1899, Nov. 8--12, 1998.

[38] A. Gorokhov, ``Transmit diversity versus SDMA: analytic and numerical comparisons," in *Proc. IEEE International Conference on Communications ICC 2000*, vol. 2, pp. 1020--1024, June 18--22, 2000.

[39] Y.-T. Hsieh and P.-A. Ting, ``An efficient multi-mode channel tracking scheme under different velocities in OFDM systems," in *Proc. 16th International Conference on Computer Communications and Networks ICCCN 2007*, pp. 888--893, Aug. 13--16, 2007.

[40] J. P. Kermoal, L. Schumacher, P. E. Mogensen, and K. I. Pedersen, ``Experimental investigation of correlation properties of MIMO radio channels for indoor picocell scenarios," in *Proc. 52nd Vehicular Technology Conference IEEE VTS-Fall VTC 2000*, vol. 1, pp. 14--21, Sept. 24--28, 2000.